TAMPEREEN TEKNILLINEN YLIOPISTO
TAMPERE UNIVERSITY OF TECHNOLOGY

Aapo Aapro

Factors in Active Damping Design to Mitigate Grid Interactions in Three-Phase Grid-Connected Photovoltaic Inverters

Julkaisu 1502 • Publication 1502

Tampere 2017

Tampereen teknillinen yliopisto. Julkaisu 1502
Tampere University of Technology. Publication 1502

Aapo Aapro

Factors in Active Damping Design to Mitigate Grid Interactions in Three-Phase Grid-Connected Photovoltaic Inverters

Thesis for the degree of Doctor of Science in Technology to be presented with due permission for public examination and criticism in Rakennustalo Building, Auditorium RG202, at Tampere University of Technology, on the 13th of October 2017, at 12 noon.

Tampereen teknillinen yliopisto - Tampere University of Technology
Tampere 2017

Doctoral candidate: Aapo Aapro
Laboratory of Electrical Energy Engineering
Faculty of Computing and Electrical Engineering
Tampere University of Technology
Finland

Supervisor: Teuvo Suntio, Professor
Laboratory of Electrical Energy Engineering
Faculty of Computing and Electrical Engineering
Tampere University of Technology
Finland

Instructor: Tuomas Messo, Assistant professor
Laboratory of Electrical Energy Engineering
Faculty of Computing and Electrical Engineering
Tampere University of Technology
Finland

Pre-examiners: Xiongfei Wang, Associate professor
Department of Energy Technology, Power Electronic Systems
Faculty of Engineering and Science
Aalborg University
Denmark

Pedro Luis Roncero Sánchez-Elipe, Associate professor
School of Industrial Engineering
University of Castilla-La Mancha
Spain

Opponents: Xiongfei Wang, Associate professor
Department of Energy Technology, Power Electronic Systems
Faculty of Engineering and Science
Aalborg University
Denmark

Marko Hinkkanen, Associate professor
Department of Electrical Engineering and Automation
School of Electrical Engineering
Aalto University
Finland

ISBN 978-952-15-4013-4 (printed)
ISBN 978-952-15-4036-3 (PDF)
ISSN 1459-2045

ABSTRACT

An LCL filter provides excellent mitigation capability of the switching frequency harmonics, and is, therefore, widely used in grid-connected inverter applications. The resonant behavior induced by the filter must be attenuated with passive or active damping methods in order to preserve the stability of the grid-connected converter. Active damping can be implemented with different control algorithms, and it is frequently used due to its relatively simple and low-cost implementation. However, active damping may easily impose stability problems if it is poorly designed.

This thesis presents a comprehensive small-signal model of a three-phase grid-connected photovoltaic inverter with LCL filter. The analysis is focused on a capacitor-current-feedback (i.e., a multi-current feedback) active damping and its effects on the system dynamics. Furthermore, a single-current-feedback active damping technique, which is based on reduced number of measurements, is also studied. The main objective of this thesis is to present an accurate multi-variable small-signal model for assessing the control performance as well as the grid interaction sensitivity of grid-connected converters in the frequency domain.

The state-of-the-art literature studies regarding the active damping are mainly concentrated on stability evaluation of the output-current loop, and the effect on external characteristics such as susceptibility to background harmonics and impedance-based instability has been overlooked. As the active damping affects significantly the sensitivity to grid interactions, accurate predictions of the system transfer functions, e.g. the output impedance, must be utilized in order to assess the active-damping-induced properties. Moreover, the single-current-feedback active damping method lacks the aforementioned analysis in the literature and, therefore, the need for accurate full-order small-signal models is evident.

This thesis presents design criteria for the active damping in a wide range of operating conditions. Accordingly, peculiarities regarding the active damping are discussed for both multi and single-current-feedback active damping schemes. In addition, the parametric influence of the active damping on the output-impedance characteristics is explicitly analyzed. It is shown that the active damping design has a significant effect on the output impedance and, therefore, the impedance characteristics should be considered in the converter design for improved robustness against background harmonics and impedance-based interactions.

PREFACE

This research was carried out at the Laboratory of Electrical Energy Engineering (LEEE) at Tampere University of Technology (TUT) during the years 2014 - 2017. The research was funded by the university and ABB Oy. In addition, the financial support received from the Finnish Academy of Science and Letters as well as from the Otto A. Malm foundation is greatly appreciated.

First of all, I want to express my gratitude to Professor Teuvo Suntio for supervising my thesis. All the constructive feedback as well as the insightful discussions have helped and motivated me towards the degree. Moreover, my work would not be finished without the contribution of other amazing members of our team. I want to thank especially Assistant Professor Tuomas Messo for helping me throughout my academic career at the university. All the discussions and your help with practical matters have contributed a lot to my thesis work, and I appreciate it very much. Also, the current and former members of our research team, Assistant Professor Petros Karamanakos, Ph.D. Jenni Rekola, Ph.D. Juha Jokipii, M.Sc. Jukka Viinamäki, M.Sc. Jyri Kivimäki, M.Sc. Kari Lappalainen, M.Sc. Julius Schnabel, M.Sc. Matti Marjanen, M.Sc. Markku Järvelä, M.Sc. Matias Berg, B.Sc. Antti Hildén and B.Sc. Roosa-Maria Sallinen, you deserve a special thanks for creating a delightful and relaxed atmosphere. Furthermore, all the staff at LEEE deserve my thanks for making these years at the university extremely pleasant.

I am grateful to Associate Professors Xiongfei Wang and Pedro Roncero for examining my thesis and providing supportive comments, which have helped me to improve the quality of my thesis.

Last but not least, I want express my gratitude to my family, friends and Susanna. You have supported and encouraged me throughout my academic career which has motivated me more than I dare to admit. I thank you all for that.

Tampere, September 13, 2017

Aapo Aapro

CONTENTS

SYMBOLS AND ABBREVIATIONS

ABBREVIATIONS

AC	Alternating current
AD	Active damping
ADC	Analog-to-digital converter
BPF	Band-pass filter
CC	Constant current, current controller
CV	Constant voltage
CSI	Current-source inverter
DAC	Digital-to-analog converter
DC	Direct current
DC-DC	DC to DC converter
DC-AC	DC to AC converter
Dr. Tech.	Doctor of Technology
DSP	Digital signal processor
FRA	Frequency-response analyzer
GW	Gigawatt
HPF	High-pass filter
LHP	Left-half of the complex plane
LPF	Low-pass filter
MPP	Maximum power point
MPPT	Maximum power point tracker
p.u.	Percent unit
PC	Personal computer
PI	Proportional-integral controller
PLL	Phase-locked loop
PRBS	Pseudo-random binary sequence
PV	Photovoltaic
PVG	Photovoltaic generator
RHP	Right-half of the complex plane
SAS	Solar array simulator
TW	Terawatt
VC	Voltage controller
VSI	Voltage-source inverter

GREEK CHARACTERS

$\langle i_{\mathrm{L}\alpha} \rangle$	Alpha-component of the inductor current
$\langle i_{\mathrm{L}\beta} \rangle$	Beta-component of the inductor current
x_α	Alpha-component of a space-vector
x_β	Beta-component of a space-vector
ω_{s}	Angular frequency of the grid
θ_{c}	Phase angle

LATIN CHARACTERS

A	Diode ideality factor
A	Coefficient matrix A of the state-space representation, Connection point for phase A inductor
B	Coefficient matrix B of the state-space representation, Connection point for phase B inductor
C	Coefficient matrix C of the state-space representation, Connection point for phase C inductor
C_{in}	Capacitance of the DC-link capacitor
C	Capacitance of the three-phase output filter
d	Differential operator, d-component in the synchronous frame
$\hat{d}$	Small-signal duty ratio of the DC-DC converter
$\boldsymbol{d}$	Duty ratio space-vector
$\boldsymbol{d}^{\mathbf{s}}$	Duty ratio space-vector in synchronous frame
d_{a}	Duty ratio of the upper switch in phase A
d_{b}	Duty ratio of the upper switch in phas B
d_{c}	Duty ratio of the upper switch in phase C
d_{d}	Direct component of the duty ratio space-vector
$\hat{d}_{\mathrm{d}}$	Small-signal d-component of the duty ratio space-vector
d_{q}	Quadrature component of the duty ratio space-vector
$\hat{d}_{\mathrm{q}}$	Small-signal q-component of the duty ratio space-vector
D	Coefficient matrix D of the state space representation
D_{d}	Steady-state d-component of the duty ratio
D_{q}	Steady-state q-component of the duty ratio
$\mathbf{G}$	Transfer function matrix
G_{AD}, $\mathbf{G}_{\mathrm{AD}}$	Active damping gain, active damping gain matrix
$G_{\text{cc-d}}$,$G_{\text{cc-q}}$	Current controller transfer functions
G_{ci}	Control-to-input transfer function
G_{co}	Control-to-output transfer function
G_{del}, $\mathbf{G}_{\mathrm{del}}$	Delay transfer function, delay transfer matrix

G_{io}	Input-to-output transfer function
G_{se}	Voltage sensing gains
G_{vc}	Voltage controller
$i_{\mathrm{i=a,b,c}}$	Current of phase a, b or c
I_0	Dark saturation current
i_{C}	Capacitor C_1 current
i_{Cin}	DC-link capacitor current
i_{d}	Current of the diode in the one-diode model
i_{in}	Inverter input current
$\hat{i}_{\mathrm{in}}$	Small-signal DC-DC converter output/inverter input current
I_{in}	Steady-state inverter input current
$\langle \boldsymbol{i}^{\mathrm{s}}_{\mathrm{L1}} \rangle$	Inverter-side inductor current space-vector in synchronous frame
$\langle \boldsymbol{i}_{\mathrm{L1}} \rangle$	Inverter-side inductor current space-vector in stationary frame
$\hat{i}_{\mathrm{L1}}$	Small-signal inverter-side inductor L_1 current
$i_{\mathrm{L1(a,b,c)}}$	Inductor $L_{1(\mathrm{a,b,c})}$ current
$\langle i_{\mathrm{L1(a,b,c)}} \rangle$	Average inductor $L_{1(\mathrm{a,b,c})}$ current
$\langle \boldsymbol{i}^{\mathrm{s}}_{\mathrm{L2}} \rangle$	Grid-side inductor current space-vector in synchronous frame
$\langle \boldsymbol{i}_{\mathrm{L2}} \rangle$	Grid-side inductor current space-vector in stationary frame
$\hat{i}_{\mathrm{L2}}$	Small-signal grid-side inductor L_2 current
$i_{\mathrm{L2(a,b,c)}}$	Grid-side inductor $L_{2(\mathrm{a,b,c})}$ current
$\langle i_{\mathrm{L2(a,b,c)}} \rangle$	Average inductor $L_{2(\mathrm{a,b,c})}$ current
$\langle i_{\mathrm{L(1,2)d}} \rangle$	Average d-component of the inductor current space-vector
$\hat{i}_{\mathrm{L(1,2)d}}$	Small-signal d-component of the inductor current space-vector
$I_{\mathrm{L(1,2)d}}$	Steady-state d-component of the inductor current
$i^{\mathrm{ref}}_{\mathrm{L1d}}$	Reference of the output current d-component
$\langle i_{\mathrm{L(1,2)q}} \rangle$	Average q-component of the inductor current space-vector
$\hat{i}_{\mathrm{L(1,2)q}}$	Small-signal q-component of the inductor current space-vector
$I_{\mathrm{L(1,2)q}}$	Steady-state q-component of the inductor current
$i^{\mathrm{ref}}_{\mathrm{L1q}}$	Reference of the output current q-component
$i_{\mathrm{o(a,b,c)}}$	Output phase current, refer to $i_{\mathrm{L2(a,b,c)}}$
$\langle i_{\mathrm{o\text{-}d}} \rangle$	Average d-component of the output current space-vector
$\hat{i}_{\mathrm{od}}$	Small-signal d-component of the output current space-vector
$\langle i_{\mathrm{o\text{-}q}} \rangle$	Average q-component of the output current space-vector
$\hat{i}_{\mathrm{oq}}$	Small-signal q-component of the output current space-vector
i_{P}	Current flowing from the DC-link toward the inverter switches
$\langle i_{\mathrm{P}} \rangle$	Average current flowing toward the inverter switches
i_{ph}	Photocurrent
$\hat{i}_{\mathrm{pv}}$	Small-signal output current of the photovoltaic generator
i_{pv}	Output current of the photovoltaic generator
I_{pv}	Steady-state output current of the photovoltaic generator

I_{sc}	Short-circuit current of the photovoltaic generator
j	Imaginary part
k_{i}	Scaling constant of the integral term in PI-controller
k_{p}	Scaling constant of the proportional term in PI-controller
L	Inductance of the inverter when all phases are symmetrical
$L_{1(\mathrm{a,b,c})}$	Inverter-side inductance of phase A/B/C
$L_{2(\mathrm{a,b,c})}$	Grid-side inductance of phase A/B/C
L_{in}	DC-link voltage control loop gain
$L_{\text{out-d}}$	Current control loop gain of the d-component
$L_{\text{out-q}}$	Current control loop gain of the q-component
L_{PLL}	Control loop gain of the phase-locked-loop
n	Neutral point
N	Negative rail of the DC-link
P	Positive rail of the DC-link
P_{MPP}	Power at the maximum-power point
p_{pv}	Instantaneous output power of the photovoltaic generator
q	Q-component in the synchronous frame
r_{C}	Parasitic resistance of capacitor C
r_{Cin}	Parasitic resistance of the DC-link capacitor
r_{D}	Parasitic resistance of a diode
R_{d}	Damping resistance, virtual resistor value
R_{eq}	Equivalent resistance related to the inverter
$r_{\mathrm{L1(a,b,c)}}$	Parasitic resistance of inverter-side inductor L_1
$r_{\mathrm{L2(a,b,c)}}$	Parasitic resistance of grid-side inductor L_2
r_{pv}	Dynamic resistance of the photovoltaic generator
r_{s}	Series resistance in the one-diode model
r_{sh}	Shunt resistance in the one-diode model
r_{sw}	Parasitic resistance of the converter switches
s	Laplace variable
$\underline{\hat{u}}$	Column-vector containing input variables
$\mathbf{U}$	Input-variable vector in Laplace-domain
u_{a}	Voltage of phase A
$\langle u_{\mathrm{a}} \rangle$	Average voltage of phase A
$\langle u_{\mathrm{AN}} \rangle$	Average voltage between points A and N
u_{b}	Voltage of phase B
$\langle u_{\mathrm{b}} \rangle$	Average voltage of phase B
$\langle u_{\mathrm{BN}} \rangle$	Average voltage between points B and N
u_{c}	Voltage of phase C
$\langle u_{\mathrm{c}} \rangle$	Average voltage of phase C
$\langle u_{\mathrm{CN}} \rangle$	Average voltage between points C and N

$\langle \boldsymbol{u}_{\mathrm{C}}^{\mathrm{s}} \rangle$	Filter capacitor voltage space-vector in synchronous frame
$\langle \boldsymbol{u}_{\mathrm{C}} \rangle$	Filter capacitor voltage space-vector in stationary frame
$\hat{u}_{\mathrm{C}}$	Small-signal voltage over the capacitor C
u_{C}	Voltage over the capacitor C
U_{C}	Steady-state voltage over the capacitor C
u_{Cin}	DC-link capacitor voltage
$\hat{u}_{\mathrm{Cin}}$	Small-signal DC-link capacitor voltage
U_{Cin}	Steady-state DC-link capacitor voltage
$u_{\mathrm{i=a,b,c}}$	Three-phase grid voltages
u_{d}	Voltage over a diode in the one-diode model
$\langle \boldsymbol{u}_{\mathrm{g}} \rangle$	Grid voltage space-vector
$\langle \boldsymbol{u}_{\mathrm{g}}^{\mathrm{s}} \rangle$	Grid voltage space-vector in synchronous frame
$\hat{u}_{\mathrm{in}}$	Small-signal input voltage
$\langle u_{\mathrm{in}} \rangle$	Average input voltage
u_{in}	Instantaneous input voltage
U_{in}	Steady-state input voltage
$\langle \boldsymbol{u}_{\mathrm{L}} \rangle$	Inductor voltage space-vector
$u_{\mathrm{L(a,b,c)}}$	Voltage over the inductor $L_{\mathrm{a,b,c}}$
$\langle u_{\mathrm{L(a,b,c)}} \rangle$	Average voltage over the inductor $L_{\mathrm{a,b,c}}$
U_{MPP}	Voltage at the maximum power point
$\langle u_{\mathrm{nN}} \rangle$	Average common-mode voltage
u_{o}	Output voltage
U_{oc}	Open-circuit voltage of the photovoltaic generator
U_{od}	Steady-state d-component of the grid voltage
$\hat{u}_{\mathrm{od}}$	Small-signal d-component of the grid voltage
U_{oq}	Steady-state q-component of the grid voltage
$\hat{u}_{\mathrm{oq}}$	Small-signal q-component of the grid voltage
u_{pv}	Voltage across the photovoltaic generator terminals
U_{pv}	Steady-state voltage of the photovoltaic generator
t	Time
T_{oi}	Open-loop output-to-input transfer function
$\underline{\hat{x}}$	Vector containing state variables
$\boldsymbol{x}$	Space-vector
$\boldsymbol{x}^{\mathrm{s}}$	Space-vector in a synchronous reference frame
x_0	Zero component of a space-vector
x_{a}	Variable related to phase A
x_{b}	Variable related to phase B
x_{c}	Variable related to phase C
x_{d}	Direct component of a space-vector
x_{q}	Quadrature component of a space-vector

$\underline{\hat{y}}$	Vector containing output variables
$\underline{\mathbf{Y}}$	Output-variable vector in Laplace-domain
Y_{o}	Output admittance
Z_{in}	Input impedance
Z_{o}	Output impedance

SUBSCRIPTS

d	Transfer function related to d-components
dq	Transfer function from d to q-component
f	Variable related to the three-phase filter
mod	Active-damping-related modifier transfer function
q	Transfer function related to q-components
qd	Transfer function from q to d-component
sw	Power electronic switch

SUPERSCRIPTS

$*$	Complex conjugate of a space-vector
-1	Inverse of a matrix or a transfer function
AD	Transfer function which includes the effect of active damping
c	Variable in the control system reference frame
DC-DC	Transfer function related to the DC-DC converter
DC-AC	Transfer function related to the inverter
g	Variable in the grid reference frame
L	Transfer function which includes the effect of the load
multi	Transfer function related to multi-current-feedback active damping
out	Transfer function which includes the effect of the current control
ref	Reference value
single	Transfer function related to single-current-feedback active damping
S	Transfer function which includes the effect of the source
tot	Transfer function which includes the effect of the voltage control

1 INTRODUCTION

This chapter discusses the background of the thesis and introduces the reader to the topic. Accordingly, an introduction for photovoltaic energy systems is given first and the details regarding the behavior of photovoltaic generators as energy sources are elaborated. Small-signal modeling is applied extensively in this thesis and, therefore, the background for the modeling method as well as its usefulness are highlighted. Theory behind the active damping and output impedance analysis are also discussed as they form the framework for the thesis.

1.1 Renewable energy and introduction to photovoltaic systems

Evidence for global warming and the greenhouse effect is undeniable. Globally, approximately 87% of the total energy produced is generated by fossil fuels from which the majority (38%) comes from oil [1]. Excessive use of fossil fuels increases the emissions of carbon dioxide (CO2) which, in turn, further accelerates the greenhouse effect. In order to slow down the climate change, public attention has been drawn on the issue and, correspondingly, European Union has launched the Roadmap 2050-project with an objective to reduce greenhouse gas emissions at least 80% below the 1990 levels by 2050 [2]. Fossil fuel-dependency must be decreased in order to stop accumulating CO2 into the atmosphere and, thus, these actions are highly necessary.

The aforementioned factors have led to growing interest in the field of grid-connected renewable energy systems, and the utilization of these has been increasing continuously for several years [1]. Solar energy is one of the most promising renewable energy resources due to its environmentally friendly features and relatively low cost of harvesting. Furthermore, it is practically inexhaustible within a realistic time frame. Energy from the Sun is mainly harvested either by using it for heating or by converting to electrical energy. Usually, the electrical energy is harvested using silicon-based solar panels and their price has been rapidly decreasing throughout the world, which makes the use of them in energy production feasible in terms of invested money and payback time. Regarding the usability of solar energy, it is expected to be the second most utilized energy source by 2020 excluding hydroelectric energy [3].

Considering the electrical characteristics, the photovoltaic generators produce direct current (DC), which has to be transformed into alternating current (AC) in order to

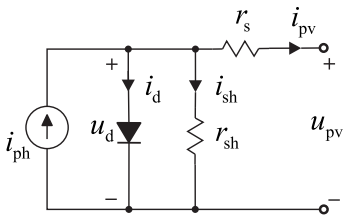

Fig. 1.1: Simplified electrical equivalent single-diode model of a photovoltaic generator.

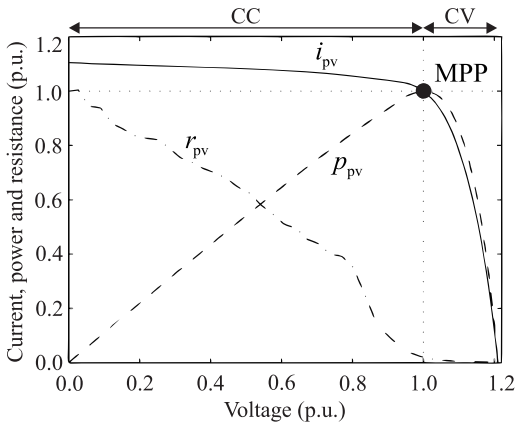

Fig. 1.2: Voltage-current (solid line) and voltage-power (dashed line) curves of a photovoltaic generator as well as the behavior of the dynamic resistance r_{pv}.

be transferred into the AC grid. The conversion from DC to AC is performed with switched-mode power supplies. However, PV generators exhibit peculiar characteristics, which have fundamental effect on the interfacing power electronic converters and their design. Accordingly, the photovoltaic generator can be characterized as a power-limited non-ideal current source with both constant-current and constant-voltage-like properties, which are discussed explicitly in multiple publications [4–6]. This behavior imposes persistent design constraints, which can easily cause stability problems if not considered properly when designing the power-electronic-based devices for photovoltaic applications. A simplified electrical equivalent model characterizing the inherent properties of a PV cell is shown in Fig. 1.1, where r_{s} and r_{sh} represents the losses inside the cell, u_{pv} is the terminal voltage of the cell, i_{pv} is the output current of the cell, i_{d} is the current through the diode and i_{ph} is the photocurrent.

Irradiation from the Sun, upon interacting with the semi-conductor surface of the solar cell, creates the photovoltaic current i_{ph}, which is directly proportional to the irradiance level. The actual output current of the generator is affected by the series and shunt resistances (representing non-ideal properties) as well as the *pn*-junction of the cell

which can be presented as

$$i_{\mathrm{pv}} = i_{\mathrm{ph}} - \underbrace{i_0 \left(e^{\frac{u_{\mathrm{pv}} + r_{\mathrm{s}} i_{\mathrm{pv}}}{NakT/q}} - 1 \right)}_{i_{\mathrm{d}}} - \frac{u_{\mathrm{pv}} + r_{\mathrm{s}} i_{\mathrm{pv}}}{r_{\mathrm{sh}}}, \tag{1.1}$$

where i_0 is the diode reverse saturation current, T (Kelvin) is the cell temperature, k is the Bolzmann constant, a the diode ideality factor, q the electron charge and N is the number of series-connected photovoltaic cells.

As can be deduced from the exponential term in (1.1), the voltage-current characteristics of the PV cell are highly non-linear and can be conveniently solved only by numerical methods. Accordingly, the illustration of the voltage-current and voltage-power dependency of a traditional PV cell can be given as shown in Fig. 1.2. Maximum power can be extracted only at one point, which is called the maximum power point (MPP), although, recent literature indicates that it is in practice a wider constant power region (CPR) [7]. The control system of the interfacing converter tries to keep the operating point near the MPP for maximal power extraction.

Considering Eq. (1.1) as well as Figs. 1.3a and 1.3b, the electrical characteristics of the PV cell will change in proportion to the irradiance level and the cell temperature. Evidently, the short-circuit current produced by the PV cell is directly proportional to the irradiance and, conversely, only minor changes in the open-circuit voltage of the PV cell can be observed when the irradiation level changes. The temperature of the PV cell, on the other hand, affects mainly the open-circuit voltage and has negligible effect on the short-circuit current. Accordingly, higher open-circuit voltages are obtained when the cell temperature is lower, thus an increase of the cell temperature decreases the maximum power extractable from the cell. Consequently, based on the aforementioned factors, the PV current has relatively fast dynamics, affected mainly by the irradiance level, compared to the voltage, which has only slow temperature-dependent dynamics.

In addition to the MPP, two distinct operating regions can be observed in the PV-cell current-voltage (IV) behavior according to Fig. 1.2. When the voltage of the PV cell is below the MPP voltage, a constant current region (CCR) is found, where the current remains relatively constant despite the changes in the PV cell voltage and the PV cell exhibits higher dynamic resistance, thus resembling the characteristics of an ideal current source. Conversely, when the cell voltage is above the MPP voltage, the behavior of the PV cell resembles a constant voltage source as the dynamic resistance of the converter is small and the voltage stays relatively constant regardless of the changes in the current. Correspondingly, this is called the constant voltage region (CVR). Due to the aforementioned constant-voltage and constant-current-like properties, the design and control of the inverter have inherent constraints and, therefore, the effect of the source

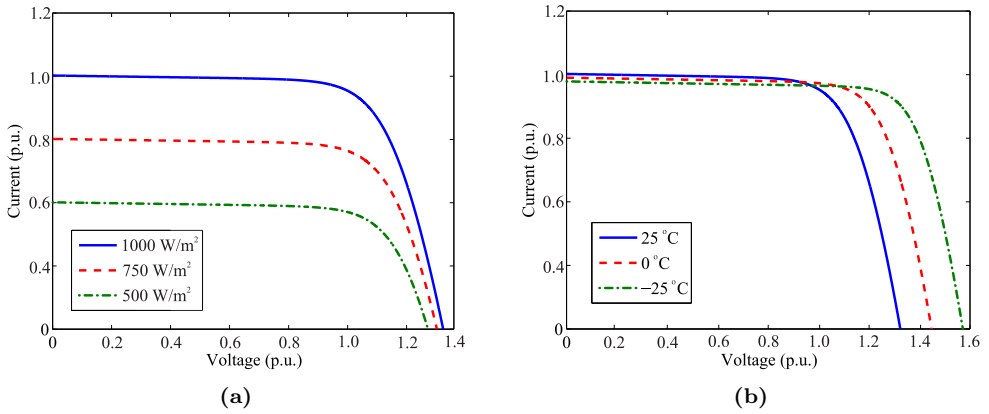

Fig. 1.3: Effect of (a) irradiance and (b) temperature on the electrical characteristics of a PV cell.

has to be properly included in the dynamical modeling in order to analyze the system behavior correctly. Analyzing the converter only as voltage or current-sourced may yield sufficient results for one operating point but the transition between operating points in a real system is inevitable, which may lead to a loss of stability because of faulty analysis.

1.2 Small-signal modeling principles

Small-signal modeling technique, first introduced by Middlebrook in the 70's, is commonly used in the analysis of power-electronic-based systems due to their non-linear nature [8]. That is, in a linear system, an input signal $u = U + \hat{u}$ would yield a proportional output signal as $y = Y + \hat{y}$, where the small-signal AC perturbation (denoted by accent '$\hat{x}$') is of the same frequency between the input and output variables. However, due to the varying switching states of power-electronic-based system, this requirement for linearity does not hold as the system switches between two or more linear networks (depending on the conduction mode). The system has to be, therefore, averaged and linearized at a predefined operating point, where the system behaves as a linear circuit. Accordingly, small-signal transfer functions can be developed for different input-to-output combinations as $G = \hat{y}/\hat{u}$, which are used to examine different dynamical properties such as control-to-output and input-to-output responses as well as input or output impedances.

In order to obtain a small-signal model for an arbitrary system, first the correct state, input and output variables are chosen, and then the average-valued model is formed according to the Kirchhoff's laws. Generally, inductor currents and capacitor voltages are chosen as the state variables since their derivatives, used in the state-space modeling, have a clear meaning. Note that any linearly independent set of variables can be chosen as the state variables but their usefulness may be questionable. The averaging is done by separately determining equations for different switching states, which are then weighted

(averaged) over one switching cycle to remove the effect of the switching ripple. Accordingly, the average-valued or the large-signal model is obtained and the corresponding state-space equations can be given by

$$\begin{aligned} \tfrac{\mathrm{d}\underline{x}}{\mathrm{d}t} &= \mathbf{A}\underline{x} + \mathbf{B}\underline{u} \\ \underline{y} &= \mathbf{C}\underline{x} + \mathbf{D}\underline{u} \end{aligned} \tag{1.2}$$

where vectors $\underline{x}$, $\underline{u}$ and $\underline{y}$ denote the state, input and output variable vectors, respectively. This may not be sufficient for the formulation of the system transfer functions because such model may be nonlinear after recognizing the duty ratio (or the control signal) d as a modulated variable and, therefore, an input signal [8]. Correspondingly, a situation may arise where the state or output variables are multiplied by the duty ratio, which yields a nonlinear dependency between the variables. Therefore, in that case, the system has to be linearized by taking partial derivatives of each variable, which removes the corresponding nonlinearity. After linearizing the equations, the system model can be represented by a linearized state-space in the Laplace-domain as shown in (1.3), from which the system transfer functions can be derived as in (1.4). This small-signal modeling technique is further elaborated in Chapter 2 for a specific application, i.e. for a three-phase grid-connected PV inverter.

$$\begin{aligned} \tfrac{\mathrm{d}\hat{\underline{x}}}{\mathrm{d}t} &= \mathbf{A}\hat{\underline{x}} + \mathbf{B}\hat{\underline{u}} \\ \hat{\underline{y}} &= \mathbf{C}\hat{\underline{x}} + \mathbf{D}\hat{\underline{u}} \end{aligned} \quad \rightarrow \quad \begin{aligned} s\hat{\underline{x}} &= \mathbf{A}\hat{\underline{x}} + \mathbf{B}\hat{\underline{u}} \\ \hat{\underline{y}} &= \mathbf{C}\hat{\underline{x}} + \mathbf{D}\hat{\underline{u}} \end{aligned} \tag{1.3}$$

$$\hat{\underline{y}}(s) = \left[\mathbf{C}(s\mathbf{I} - \mathbf{A})^{-1}\mathbf{B} + \mathbf{D}\right]\hat{\underline{u}} = \mathbf{G}\hat{\underline{u}}(s) \tag{1.4}$$

Depending on the terminal constraints, i.e., the inherent behavior of the source and load as well as the selection of the feedback variables, an appropriate conversion scheme must be chosen for the analysis. Accordingly, four different conversion schemes are shown in Figs. 1.4a-1.4d.

As discussed earlier, the photovoltaic generator exhibits characteristics of a non-linear current source, thus, a current source is a convenient selection as an input source, i.e., the cases shown in Figs. 1.4b or 1.4d. Furthermore, due to rather slow dynamics of the PV voltage (affected mainly by the temperature), the input voltage can be conveniently controlled for maximum power extraction, which complies with the selection of the input source. Considering the output terminal, in grid-connected applications, the output voltage is determined by the external system (i.e. the grid). A stiff grid is, therefore,

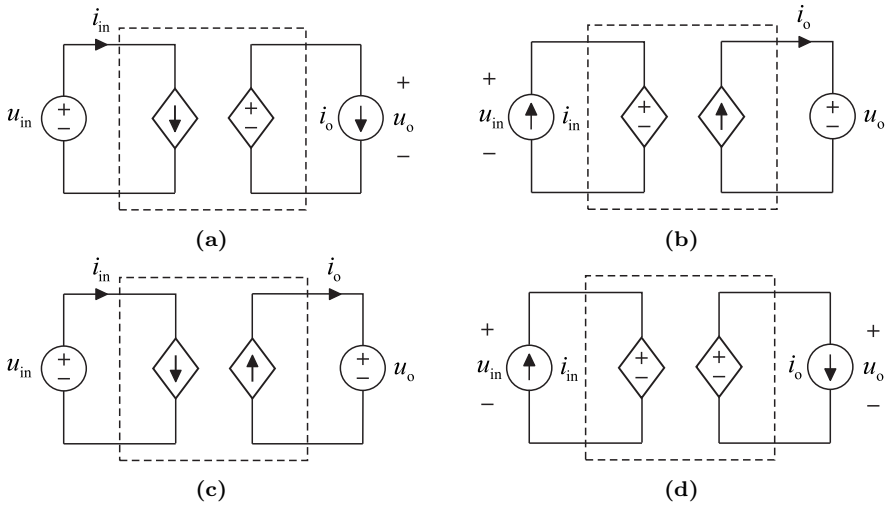

Fig. 1.4: Depiction of a) voltage-to-voltage, b) current-to-current, c) voltage-to-current and d) current-to-voltage conversion schemes.

assumed in this case, which leads to a conclusion that only the H-parameter (current-to-current conversion scheme) model is applicable in the analysis. Accordingly, the input source of the converter is a current source and the input voltage is the input-side feedback variable in order to guarantee maximum power output by means of the MPP tracking (MPPT). Furthermore, the converter output is loaded by a stiff voltage source and the system controls its output current (current injection-mode), which is known as a grid-parallel or grid-feeding mode.

Modeling of three-phase converters differs from the modeling of DC-DC converters, since the space-vector theory has to be used to analyze the three-phase variables. This means that the inverter is not analyzed per phase, but instead the three-phase variables of the small-signal model are transformed into synchronous (dq-domain) or stationary reference ($\alpha\beta$-domain) frames. Many publications analyze the inverter in a stationary reference frame in order to decrease the complexity of the analysis and the computational burden as discussed, for example, in [9–13]. However, some inconsistencies arise, since in a stationary reference frame the steady-state operating point cannot be solved in a consistent manner, which imposes restrictions for the small-signal modeling requiring a steady-state operating point. In the rotating or synchronous reference frame, the AC-quantities appear constant (i.e., DC) in the steady state, which allows the linearizing of the system.

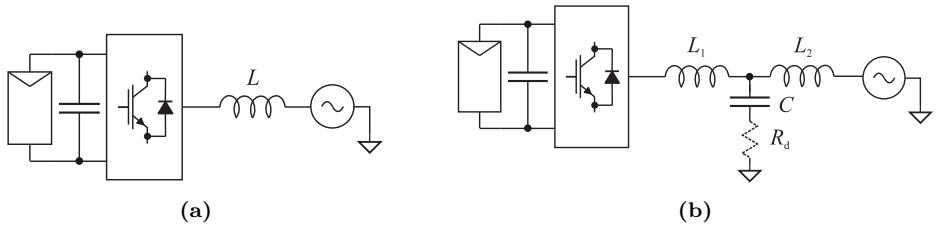

Fig. 1.5: Depictions of (a) L-filtered and (b) LCL-filtered grid-connected converters.

1.3 Passive and active damping of LCL-filter resonance

1.3.1 LCL-filter

In grid-connected applications, an inductive (L-type) filter may not sufficiently attenuate the switching-ripple currents. High power applications produce larger currents, which require high value for inductance in order to obtain sufficient attenuation of the switching harmonics. This naturally increases the system costs and size. Therefore, inductive-capacitive-inductive (LCL) filters have gained popularity as filtering elements due to their excellent harmonic attenuation capability also at lower switching frequencies [14]. An LCL-filter enables wide range of power levels with relatively small values for inductances and capacitance to achieve the same filtering performance as with only an L-type filter [10, 14–20]. For demonstrative purposes, the two filtering topologies are shown in Figs. 1.5a and 1.5b. Inherently, the LCL-filter creates several resonances in the *dq*-domain control dynamics of the converter, which must be damped in order to ensure robust performance and stability of the converter. The resonant frequencies are dependent on the passive component values of the filter and can be generally given as

$$\omega_{\text{res}} = \sqrt{\frac{L_1 + L_2}{L_1 L_2 C}}, \tag{1.5}$$

$$\omega_0 = \sqrt{\frac{1}{L_2 C}}. \tag{1.6}$$

The resonance given in (1.5) is caused by the series-parallel interaction of inverter-side inductance as well as the grid-side inductance and capacitance. Respectively, the other resonance in (1.6) is caused by the series interaction between the grid-side inductance L_2 and the filter capacitance C.

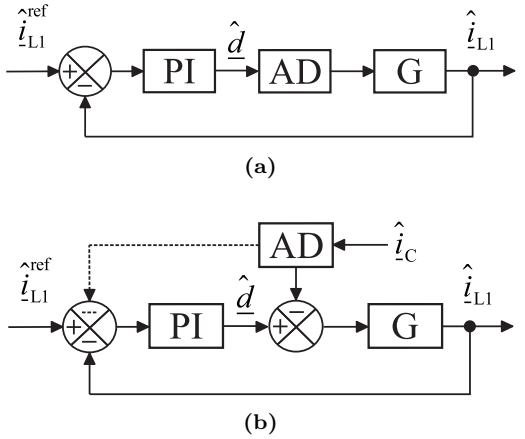

Fig. 1.6: Simplified block diagram of a control system with (a) filter-based and (b) multi-loop active damping methods.

1.3.2 Resonance damping

The resonant behavior induced by the LCL-filter can be attenuated with passive or active damping methods [14, 15, 20]. The most elementary method to damp the resonance is to add a resistor in series with the LCL-filter capacitor, which is commonly known as passive damping. Note that the resistor can be placed in parallel or series with all the passive filtering components in order to damp the resonances. The series damping resistor with the filter capacitor can be still considered as the most popular technique in the literature. Although, the resistor provides desired resonance damping, it also causes reduction in the attenuation capability and ohmic losses reducing the converter efficiency by up to 1 %. [15]. Moreover, the system costs are increased due to additional components and possible cooling elements (especially in high-power applications).

Active damping, on the other hand, is performed with different control algorithms, which are used to attenuate the resonant behavior and, due to the absence of resistive elements (excluding the ESRs of the components), power losses are negligible in the filter [21, 22]. Moreover, the attenuation capability of the filter is unaffected. Generally, active damping can be implemented either as a filter-based or multi-loop-based method, which are depicted in Figs. 1.6a and 1.6b, respectively.

Considering the filter-based method illustrated in Fig. 1.6a, no additional feedback loop is added due to the active damping. Basically, the active damping is performed by modifying the inverter control signal (or duty ratio) by means of digital filters such as low-pass, lead-lag or notch filters. Accordingly, the purpose of this method is to induce counter-resonance at the corresponding LCL-filter resonant frequencies in order to guarantee stable operation [23, 24]. This makes the filter-based active damping extremely

cost-efficient since no additional sensors are needed. As the filter-based methods usually utilize parameters from the physical filter and their implementation may be fixed inside the control system (excluding adaptive filters in special cases [25]), corresponding active damping methods are prone to inaccuracy and may even exhibit inferior stability characteristics due to parameter variation caused, e.g., by grid inductance and component aging.

Multi-loop active damping methods include additional feedbacks from a system state variable, which is used to modify the inverter control signal [20, 26, 27] or the inverter output current reference [22] (cf. Fig. 1.6b). However, in the latter case, the bandwidth of the current control limits the performance of the active damping. Considering convenient feedback variables for active damping, the filter capacitor current is usually adopted as a state feedback [27–33]. The filter capacitor voltage is also a common feedback variable [21, 31], although, problems may occur due to the discrete realization of derivative-operator (i.e., $i_C = C du_C/dt$) inside the control system [31]. If a current-feedback is utilized, the aforementioned feedback signal is used to create a so-called *virtual resistor*, which provides the resonance damping by emulating the effect of a passive resistor in series with the filter capacitor inside the control system dynamics [22, 27, 28]. Regarding the naming of the aforementioned concept, the virtual resistor is a convenient term for industrial designers due to its correspondence to the physical entity. However, it is inherently a control loop and should not be considered other than a multi-loop active damping method during the control design. Due to the factors discussed above and the popularity of the capacitor-current-feedback active damping technique, it is analyzed in this thesis.

1.3.3 Effect of delay on active damping

Digital processing delay, present in modern digital control systems, deteriorates the performance of active damping. That is, the active damping feedback signal may be modified significantly by the delay causing insufficient damping or stability problems due to the appearance of right-half-plane (RHP) poles in the output-current-control dynamics [28–30, 34–38]. The delay nearly exclusively determines the performance and stability of active damping as well as it imposes major design constraints. Accordingly, the condition where the resonant frequency (cf. Eq. (1.5)) of the LCL-filter equals one-sixth of the sampling frequency (f_s) has been observed to be critical for stability of a grid-connected converter [28, 29, 31, 34, 35, 37, 39, 40]. Accordingly, the active damping feedback has to be modified depending on the resonant frequency of the LCL-filter and the sampling frequency of the control system in order to avoid delay-induced RHP-poles in the control loop.

The system delay can either induce improved or inferior stability characteristics de-

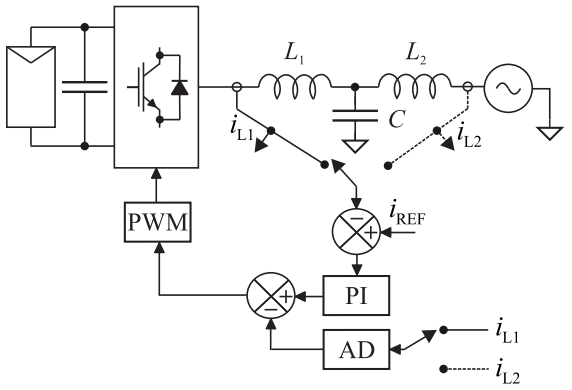

Fig. 1.7: Overview of single-current-feedback active damping schemes. Both inverter and grid-side current controls are depicted.

pending on whether the control system uses inverter current feedback (ICF) or grid current feedback (GCF) for control purposes. In fact, the delay is required for GCF converters for stability to exist but, conversely, the system delay should be minimized for ICF converters. Therefore, the ICF and GCF converters have nearly opposite stability characteristics regarding the system delay [34, 39]. Consequently, active damping is not necessary for ICF converter when $f_{\mathrm{res}} < f_{\mathrm{s}}/6$ but required for stability when $f_{\mathrm{res}} > f_{\mathrm{s}}/6$. For the GCF converter, these conditions are reversed.

Considering the factors stated above, the relevancy of system delay on the overall stability and, especially, on the active damping properties, should not be overlooked. Accordingly, the delay imposes persistent design constraints as well as a risk for unstable dynamics with both ICF and GCF converters. Aforementioned restrictions must be taken into account when selecting the feedback method (ICF/GCF) as the delay affects the active damping design profoundly.

1.3.4 Single-current-feedback active damping

Additional current sensing for active damping will most likely increase the overall system costs. Therefore, in order to decrease the costs, single-loop control strategies have been studied for LCL-filtered converters in the recent literature, which rely only on inverter-current (ICF) or grid-current feedbacks (GCF) [26, 32, 34, 39–42]. Single-loop control method denotes a system, where the current control is used to prevent the LCL-filter resonance from destabilizing the system without additional active damping loops [34, 39, 40]. This can be done by utilizing delay compensation methods such as linear predictors for ICF converters and delay-addition for GCF converters, i.e. the delay is minimized in ICF applications and increased in GCF applications.

On the other hand, active damping can be implemented based on existing current

measurements in the single-loop control scheme, i.e., an additional loop is formed from the measured inverter or grid currents. For convenience, the single-current-feedback term denotes here that the existing current measurements in the single-loop scheme are also used for active damping. Corresponding methods have been successfully demonstrated e.g. in [32, 36, 43, 44]. The additional loop distinguishes the conventional pure single-loop methods from the modified single-current-feedback active damping methods. In order to illustrate the topic further, Fig. 1.7 presents the simplified block diagram of the modified single-loop control schemes.

Considering the stability and robustness, different conclusions have been made regarding, which of the single-current-feedback methods - ICF or GCF system - is the best. Reference [32] concludes that the ICF method would be superior due to inherent damping effect of the aforementioned control solution. However, the effect of system delay is neglected in the analysis, which hides essential inherent properties of active damping [34]. Single-current-feedback active damping was also proposed to be successful for ICF converters in [43]. Conversely, the GCF system might be more convenient as the system delay, persistent in digitally controlled systems, is beneficial for its stability contrary to the ICF systems [34, 39]. Successful control system and active damping implementations have been proposed for both ICF and GCF converters and no clear consensus can be found whether one of the aforementioned method is superior over the other [32, 36, 43, 44]. Therefore, the system dynamics of an ICF converter are further elaborated in this thesis in order to widen the knowledge for corresponding converters.

The single-current-feedback scheme is inherently different from its capacitor-current-feedback counterpart and, therefore, different dynamic properties are naturally imposed in the converter dynamics. The differences between the aforementioned two schemes need to be highlighted in order to further improve the knowledge on single-current-feedback active damping methods.

1.4 Impedance-based analysis

Considering the output terminal properties of a power electronic converter, a small-signal response between the voltage and current at the same terminal represents an admittance or impedance depending on the system configuration. In a grid-feeding converter (i.e., the output terminal current is controlled), the relation between the voltage and current is considered as admittance, which represents the frequency-domain response of the output current against output voltage perturbations. Conversely, for a grid-forming converter (i.e., the output terminal voltage is controlled), the output impedance represents the response of output voltage against the grid-current perturbations. Accordingly, the responses can be expressed as $Y_\mathrm{o} = i_\mathrm{o}/u_\mathrm{o}$ and $Z_\mathrm{o} = u_\mathrm{o}/i_\mathrm{o}$ for the grid-feeding and grid-forming converters, respectively. However, regarding the topic of the thesis, only the

former is considered.

Active damping affects the system dynamics (i.e., transfer functions) by modifying the duty ratio of the converter and, thus, introducing an additional loop-structure inside the output-current-control loop. As the output-current loop affects the deviations between the measured and reference currents only within its bandwidth, the effect of active damping is visible at frequencies beyond the output-current loop. Thus, different output impedance properties are obtained at the resonant frequency, which dictate the external behavior of the converter, i.e., the susceptibility to the grid background harmonics and harmonic instability.

The utility grid usually contains numerous power electronic devices as well as other non-linear loads, which draw non-sinusoidal currents. Consequently, the current consists of multiple harmonics, which interact with the grid impedance causing distortions in the supply voltage waveform. The grid impedance is determined by the configuration of the power delivery system including transmission cables, transformers and other power electronic devices. These affect the grid impedance seen by grid-connected electrical systems as illustrated in Fig. 1.8. Accordingly, the grid impedance at the point-of-common-coupling (PCC) may contain several resonances along with the inductive characteristics at higher frequencies, which makes the grid impedance estimation a challenging task [45, 46].

If the grid voltage contains harmonics at a certain frequency, the operation of grid-connected power-electronic converters can be disturbed. Accordingly, the injected current (in grid-feeding converters) at the output terminal is affected according to the Ohm's law as $\hat{i}_\mathrm{o} = \hat{u}_\mathrm{o}/Z_\mathrm{o}$ and, therefore, high output impedance prevents the grid-voltage harmonics from affecting the grid current. Considering active damping and the high-frequency impedance behavior, high output impedance is required especially in multi-parallel inverter systems, where inverters can interact with each other and cause the point-of-common coupling (PCC) voltage to oscillate [47, 48]. Low output impedance allows such oscillations to be transferred into the grid current, which can further enhance the PCC voltage distortions via the grid impedance.

Grid current oscillations may occur also without significant grid background harmonics. This is caused by the finite grid impedance, which interacts with the output impedance of the converter, i.e., impedance-based interactions occur. Harmonic instabilities and resonances in solar power plants have revealed that such interactions may cause severe damage to the system hardware and impair the power quality in the grid [49]. These power quality problems, however, are not purely dependent on the internal stability of interconnected converters, and their stable control systems do not necessarily guarantee absence of harmonic resonances. Therefore, accurate output impedance models are essential when predicting the possibility for impedance-based interactions in

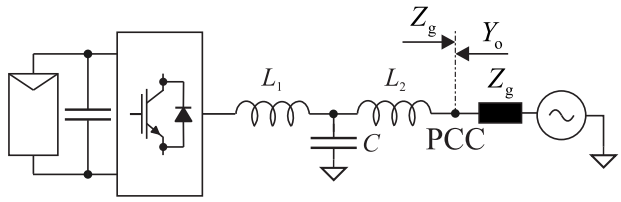

Fig. 1.8: Grid-interface of a three-phase grid-connected converter.

grid-connected applications. The frequency-domain behavior of output impedance can be obtained either by frequency-domain measurements, which can be difficult and time-consuming for high-power applications, or by analytical models. Analytical models (i.e., small-signal models), naturally, offer a very cost-efficient way to evaluate the stability of the grid-interface and, thus, the possibility for impedance-based interactions is decreased as the control system design can be carried out accordingly.

Considering aforementioned issues, impedance-based stability analysis has gained increasing attention in recent publications regarding the stability of three-phase grid-connected converters [50–62]. Output impedance has been observed to affect significantly the instability sensitivity of the converter, and the risks for impedance-based instability arise especially, for a grid-feeding converter, when the converter is connected to a weak grid (i.e., high impedance grid) [50, 52, 56, 63, 64]. Both dq-domain [52, 59, 64–67] and sequence-domain impedance models [51, 56–58] have been widely utilized in the analysis of impedance-based stability.

The impedance-based stability is assessed by using the Nyquist stability criterion, which analyses the ratio of grid impedance and converter output impedance as Z_g/Z_o (for grid-feeding converter) [50]. Aforementioned impedance ratio is also known as the inverse minor-loop gain in DC-DC systems. Risk for instability is present if the grid impedance magnitude exceeds the converter output impedance as $|Z_g|/|Z_o| \geq 1$ and the phase difference of the two impedances exceeds or equals 180 degrees. In passive circuits, this phase difference is not achievable as the phase of individual impedances is restricted to $-90°...+90°$. However, the output impedance is affected by control structures, e.g., the phase-locked loop (PLL), which forces the converter output impedance to be $-180°$ within its bandwidth inducing negative resistor-like behavior [52, 55, 58, 64, 66, 68]. Moreover, the output impedance can become also non-passive (active-type) under certain conditions due to the delay in the control system [51, 61, 69]. Accordingly, the delay seems to impose a major risk for the impedance-based instability by inducing active-type (i.e., negative real-part) impedance characteristics. Similar results are also presented in this thesis regarding the active damping, thus complying with the observations of active-type output impedance.

Even though active damping affects the output impedance significantly, there is no explicit analysis in the literature considering the issue, and some publications have only briefly discussed the topic. For example, passivity-based stability and impedance analysis for power electronic converters with active damping were discussed in [18, 63, 65, 70–73], but the comprehensive parametric influence of the active damping on the output impedance was not analyzed nor the actual impedances are experimentally verified in [18, 65, 70, 71, 73]. Output impedance analysis with active damping was presented briefly for GCF converters in [74], but the effect of the delay was neglected, which hides important information regarding the ratio of LCL-filter resonant and sampling frequencies. Furthermore, the impedances were not verified experimentally in the aforementioned paper. Active damping of DC-DC converters and its impedance properties were analyzed in [75], but the results are not directly applicable for DC-AC grid-connected converters with LCL-filters.

Clearly, the effect of the traditional capacitor-current-feedback active damping on the output impedance needs to be further clarified considering the lack of explicit analysis on the topic. Furthermore, as the single-current-feedback active damping scheme provides an attractive alternative due to its simple and inexpensive implementation, the single-current-feedback scheme and its output impedance properties are analyzed and compared to the multi-current counterpart. Due to the absence of proper research on the topic, this thesis provides incremental knowledge on the multi and single-current-feedback schemes. Severe impedance-based stability problems and harmonic resonances can be avoided if proper impedance modification via active damping is performed as will be discussed in this thesis.

1.5 Objectives and scientific contributions

This thesis presents a comprehensive small-signal model of a grid-connected PV inverter with active damping using multi-variable small-signal modeling technique. Accurate predictions of inverter transfer functions are obtained, which are utilized to elaborate the active-damping-induced properties on the output impedance and overall system dynamics. Furthermore, the stability criteria for the active damping are studied for LCL-filter resonant frequencies both lower and higher than the critical frequency of $f_s/6$ with multi-current as well as single-current-feedback schemes. Accordingly, active damping design criteria are presented and clarified for ICF converters by using both root trajectory and frequency-domain analysis. In addition, the parametric influence of the active damping on the output impedance characteristics is explicitly analyzed. It is shown that the active damping design has a significant effect on the output impedance and, therefore, the impedance analysis should be utilized in the converter design for improved robustness against background harmonics and impedance-based interactions.

The scientific contribution of this thesis can be summarized as follows:

- An accurate small-signal model characterizing the open and closed-loop dynamics of a three-phase grid-connected PV inverter with LCL-filter is formulated in this thesis. So far, explicit small-signal models for the corresponding inverter topology do not exist in the literature.
- Active damping and its effect on the system dynamics are analyzed by utilizing multi-variable modeling method, which is a novel way to study active damping. This allows explicit and accurate analysis of active damping on the system dynamics and it significantly simplifies the model derivation, which can be done with comparable effort to simple DC-DC converters.
- Output impedance characteristics for the capacitor-current-feedback active damping are presented for the first time in literature. This introduces a useful method to further improve the active damping design, which usually concentrates on the stability evaluation of the output-current control. Accordingly, the external characteristics of the inverter can be conveniently analyzed and, thus, the robustness against harmonic instability can be improved.
- Single-current-feedback active damping and its impedance properties are presented and, therefore, important information regarding the differences between the multi-current and single-current-feedback schemes are obtained.

1.6 Related publications and author's contribution

The following publications form the basis of this thesis.

[P1] Aapro, A., Messo, T., Roinila, T. and Suntio, T. (2017). "Effect of active damping on output impedance of three-phase grid-connected converter", in *IEEE Transactions on Industrial Electronics*, (accepted for publication).

[P2] Aapro, A., Messo, T. and Suntio, T. (2016). "Output impedance of grid-connected converter with active damping and feed-forward schemes", in *IEEE Annual Conference of the IEEE Industrial Electronics Society, IECON'16*, pp. 2361 – 2366.

[P3] Aapro, A., Messo, T. and Suntio, T. (2016). "Effect of single-current-feedback active damping on the output impedance of grid-connected inverter", in *IEEE European Conference on Power Electronics and Applications, EPE'16 ECCE Europe*, pp. 1 – 10.

[P4] Aapro, A., Messo, T. and Suntio, T. (2015). "Effect of active damping on the output impedance of PV inverter", in *IEEE Workshop on Control and Modeling for Power Electronics, COMPEL'15*, pp. 1 – 8.

[P5] Aapro, A., Messo, T. and Suntio, T. (2015). "An accurate small-signal model of a three-phase VSI-based photovoltaic inverter with LCL-filter", in *IEEE International Conference on Power Electronics and ECCE Asia, ICPE'15 ECCE Asia*, pp. 2267 – 2274.

[P6] Messo, T., Aapro, A. and Suntio, T. (2016). "Design of grid-voltage feedforward to increase impedance of grid-connected three-phase inverters with LCL-filter", in *IEEE International Power Electronics and Motion Control Conference, IPEMC'16 ECCE Asia*, pp. 1–6.

[P7] Messo, T., Aapro, A. and Suntio, T. (2015). "Generalized multi-variable small-signal model of three-phase grid-connected inverter in DQ-domain", in *IEEE Workshop on Control and Modeling for Power Electronics, COMPEL'15*, pp. 1 – 8.

Publications [P1]-[P5] are written and the analysis is performed by the author. However, Assistant Professor Tuomas Messo helped with the writing process by providing insightful comments regarding both the mathematical aspects and the writing itself. Furthermore, he helped with the laboratory setup used in the experimental measurements. Professor Teuvo Suntio, the supervisor of this thesis, gave valuable comments regarding these publications.

In [P6] and [P7], the author of this thesis contributed to the publications by providing comments on the theory of corresponding articles and helping to formulate the small-signal models.

1.7 Structure of the thesis

The rest of the thesis is organized as follows. Chapter 2 discusses the small-signal modeling for a three-phase grid-connected converter at open loop. Chapter 3 presents the closed-loop formulation of the corresponding system with active damping, where both the multi-current and single-current-feedback schemes are analyzed. Moreover, the stability analysis regarding the active damping design is presented. Chapter 4 concentrates on the output impedance analysis, and the active-damping-induced properties are explained. Experimental evidence as well as the validation of the models and analyses are presented in Chapter 5. The final conclusions are drawn and the future research topics discussed in Chapter 6.

2 SMALL-SIGNAL MODELING OF A THREE-PHASE GRID-CONNECTED INVERTER

This chapter presents the small-signal model for a current-fed grid-connected three-phase inverter with LCL-type grid-filter in s-domain. Modeling is performed according to the well-known state-space averaging methods, and the open-loop system transfer functions are derived, which are later used to formulate the closed-loop system.

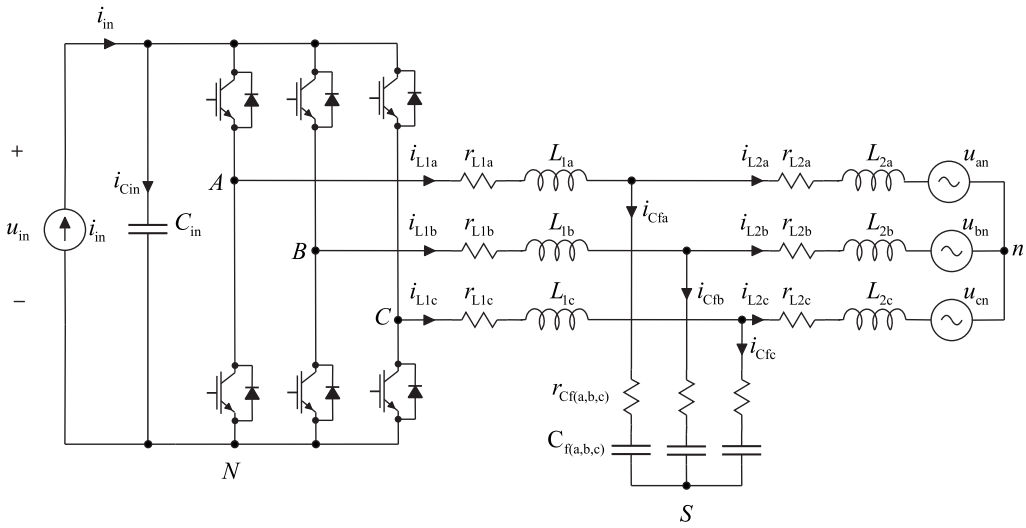

Fig. 2.1: Three-phase grid-connected current-fed VSI-type inverter with LCL-type grid filter.

The converter topology, analyzed in this thesis, is depicted in Fig. 2.1. Considering the terminal constraints discussed in Chapter 1, the system inputs are selected accordingly, i.e., the input is supplied by a current source i_{in} and the output is loaded by a fixed grid voltage $u_{(\mathrm{a,b,c})\mathrm{n}}$. According to the control engineering principles, the inputs of a system cannot be controlled, thus, they act as disturbance elements regarding the system dynamics. The output variables are, therefore, the input voltage u_{in} and the grid phase currents $i_{\mathrm{L2(a,b,c)}}$. Note that in the modeling, the inverter-side inductor currents $i_{\mathrm{L1(a,b,c)}}$ are considered as intermediate output variables, because they are the actual controlled

variables in the corresponding inverter system.

2.1 Average model

Small-signal modeling begins by deriving the average-valued equations over one switching cycle, which can be obtained from Fig. 2.1. By assuming continuous-conduction mode (CCM), the currents of the inductors are either increasing or decreasing and do not remain zero, thus, the system switches between two linear networks. The average model is derived per-phase, first by closing the upper switch in each phase and deriving expression for the inductor voltages and capacitor currents as well as for the output variables. Correspondingly, similar procedure is performed, when the lower switch of each phase is closed. The result is averaged over one switching cycle yielding the average-valued equations shown in (2.1)-(2.6). In the corresponding equations, r_{eq} denotes the combination of the switch on-time resistance r_{sw} and the inductor ESR value r_{L} and $r_{\mathrm{C(a,b,c)}}$ corresponds to the ESR of the filter capacitor. Average-valued variables are denoted with brackets, which is customary in the field of power electronics.

$$\langle u_{\mathrm{L1k}}\rangle = d_{\mathrm{k}}\langle u_{\mathrm{in}}\rangle - (r_{\mathrm{eq}} + r_{\mathrm{Cn}})\langle i_{\mathrm{L1k}}\rangle - \langle u_{\mathrm{Ck}}\rangle - r_{\mathrm{Ck}}\langle i_{\mathrm{Ck}}\rangle - \langle u_{\mathrm{SN}}\rangle,\ k = a, b, c \quad (2.1)$$

$$\langle u_{\mathrm{L2k}}\rangle = -(r_{\mathrm{L2k}} + r_{\mathrm{Ck}})\langle i_{\mathrm{L2k}}\rangle + r_{\mathrm{Ck}}\langle i_{\mathrm{L1k}}\rangle - \langle u_{\mathrm{kn}}\rangle + \langle u_{\mathrm{Sn}}\rangle + \langle u_{\mathrm{Ck}}\rangle,\ k = a, b, c \quad (2.2)$$

$$\langle i_{\mathrm{Ck}}\rangle = \langle i_{\mathrm{L1k}}\rangle - \langle i_{\mathrm{L2k}}\rangle,\ k = a, b, c \quad (2.3)$$

$$\langle u_{\mathrm{in}}\rangle = \langle u_{\mathrm{Cin}}\rangle, \quad (2.4)$$

$$\langle i_{\mathrm{Cin}}\rangle = \langle i_{\mathrm{in}}\rangle - d_{\mathrm{A}}\langle i_{\mathrm{L1a}}\rangle - d_{\mathrm{B}}\langle i_{\mathrm{L1b}}\rangle - d_{\mathrm{C}}\langle i_{\mathrm{L1c}}\rangle, \quad (2.5)$$

$$\langle i_{\mathrm{ok}}\rangle = \langle i_{\mathrm{L2k}}\rangle,\ k = a, b, c. \quad (2.6)$$

As a steady-state is required for the linearized model and the average model is derived for a three-phase system, Eqs. (2.1)-(2.6) have to be transformed into rotating vector according to the space-vector theory. Correspondingly, a three-phase variable can be expressed as a complex valued vector $\underline{x}(t)$ and real valued zero sequence component $x_z(t)$. However, a symmetrical and ideal grid condition is assumed, thus the zero sequence component is zero. Fig. 2.2 depicts a space vector $\underline{u}$ in both synchronous and stationary reference frames.

The phase representation can be easily transformed into the stationary reference frame

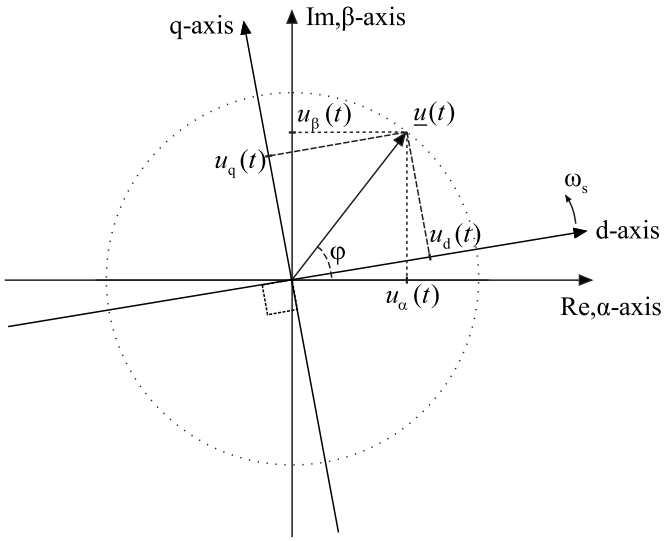

Fig. 2.2: Space vector in both stationary and synchronous reference frames.

requiring only a constant multiplication. Accordingly, the real and imaginary parts of the space vector, i.e. the alpha and beta components can be expressed by

$$x_{\alpha\beta z}(t) = \frac{2}{3}(x_{\mathrm{a}}(t)e^{j0} + x_{\mathrm{b}}(t)e^{j2\pi/3} + x_{\mathrm{c}}(t)e^{-j2\pi/3}) = x_\alpha(t) + jx_\beta(t), \tag{2.7}$$

$$x_{\alpha\beta z}(t) = \frac{2}{3}\begin{bmatrix} 1 & -\frac{1}{2} & -\frac{1}{2} \\ 0 & \frac{\sqrt{3}}{2} & -\frac{\sqrt{3}}{2} \\ \frac{1}{2} & \frac{1}{2} & \frac{1}{2} \end{bmatrix}\begin{bmatrix} x_{\mathrm{a}}(t) \\ x_{\mathrm{b}}(t) \\ x_{\mathrm{c}}(t) \end{bmatrix} \tag{2.8}$$

$$x_z(t) = \frac{1}{3}(x_{\mathrm{a}}(t) + x_{\mathrm{b}}(t) + x_{\mathrm{c}}(t)) \tag{2.9}$$

The coefficient 2/3 in aforementioned equations is a scalar, which scales the magnitude of the space vector equal to the peak value of the phase variables for symmetrical phases. Generally, the coefficient is chosen as 2/3 or $\sqrt{2/3}$ depending on if the amplitude or power invariant form is used, respectively.

According to (2.7), the average-valued equations in (2.1)-(2.6) can be expressed first in the stationary reference frame by transforming the three-phase representation into the corresponding space-vector form. The voltage across the inverter-side inductor can be

given as (denoting vectors as underlined letters)

$$\langle \underline{u}_{\mathrm{L1}} \rangle = -(r_{\mathrm{eq}} + r_{\mathrm{Ca}})\langle \underline{i}_{\mathrm{L1}} \rangle + \underline{d}\langle u_{\mathrm{in}} \rangle - \langle \underline{u}_{\mathrm{Ca}} \rangle + r_{\mathrm{Ca}}\langle \boldsymbol{i}_{\mathrm{L2}} \rangle - \frac{2}{3}(e^{j0} + e^{j2\pi/3} + e^{j4\pi/3})\langle \underline{u}_{\mathrm{SN}} \rangle. \tag{2.10}$$

The common-mode voltage $\underline{u}_{\mathrm{SN}}$ becomes zero as $e^{j0} + e^{j2\pi/3} + e^{j4\pi/3} = 0$, hence, Eq. (2.10) can be presented by

$$\langle \underline{u}_{\mathrm{L1}} \rangle = -(r_{\mathrm{eq}} + r_{\mathrm{C}})\langle \underline{i}_{\mathrm{L1}} \rangle + \underline{d}\langle u_{\mathrm{in}} \rangle - \langle \underline{u}_{\mathrm{C}} \rangle + r_{\mathrm{C}}\langle \underline{i}_{\mathrm{L2}} \rangle. \tag{2.11}$$

Furthermore, the grid-side inductor voltage can be given by

$$\langle \underline{u}_{\mathrm{L2}} \rangle = -(r_{\mathrm{L2}} + r_{\mathrm{C}})\langle \underline{i}_{\mathrm{L2}} \rangle + r_{\mathrm{C}}\langle \underline{i}_{\mathrm{L1}} \rangle + \langle \underline{u}_{\mathrm{C}} \rangle - \langle \underline{u}_{\mathrm{o}} \rangle, \tag{2.12}$$

and the filter capacitor current by

$$\langle \underline{i}_{\mathrm{C}} \rangle = \langle \underline{i}_{\mathrm{L1}} \rangle - \langle \underline{i}_{\mathrm{L2}} \rangle. \tag{2.13}$$

As the stationary-reference-frame model cannot be linearized due to constantly varying operating point, the space-vector theory is applied to transform the aforementioned equations into a synchronous reference frame by substituting $\underline{x}^s(t) = \underline{x}(t)e^{-j\omega_s t}$, where the superscript 's' denotes the synchronous reference frame and ω_s is the synchronous frequency. According to the definition for the transformation, a grid angle is subtracted from the rotating stationary reference frame counterpart and, thus, the vector in the *dq*-domain appears to be constant. The synchronous reference frame representations for (2.11)-(2.13) can be given according to transformation shown in (2.14).

$$\langle \underline{i}_{\mathrm{L1}} \rangle = \langle \underline{i}^{\mathrm{s}}_{\mathrm{L1}} \rangle e^{j\omega_s t} \rightarrow \frac{\mathrm{d}\langle \underline{i}_{\mathrm{L1}} \rangle}{\mathrm{d}t} = \frac{\mathrm{d}\langle \underline{i}^{\mathrm{s}}_{\mathrm{L1}} \rangle}{\mathrm{d}t} e^{j\omega_s t} + j\omega_s \langle \underline{i}^{\mathrm{s}}_{\mathrm{L1}} \rangle e^{j\omega_s t} \tag{2.14}$$

By substituting (2.14) into (2.11) and rearranging yields

$$\frac{\mathrm{d}\langle \underline{i}^{\mathrm{s}}_{\mathrm{L1}} \rangle}{\mathrm{d}t} = \frac{1}{L_1}\Big[\underline{d}^{\mathrm{s}}\langle u_{\mathrm{in}} \rangle - (r_{\mathrm{eq}} + r_{\mathrm{C}} + j\omega_s L_1)\langle \underline{i}^{\mathrm{s}}_{\mathrm{L1}} \rangle + r_{\mathrm{C}}\langle \underline{i}^{\mathrm{s}}_{\mathrm{L2}} \rangle - \langle \underline{u}^{\mathrm{s}}_{\mathrm{C}} \rangle\Big]. \tag{2.15}$$

Similar procedures are performed for all stationary-reference-frame variables and, accord-

ingly, the synchronous form for the grid-side inductor can be expressed by

$$\frac{\mathrm{d}\langle \underline{i}^{\mathrm{s}}_{\mathrm{L2}}\rangle}{\mathrm{d}t} = \frac{1}{L_2}\Big[-(r_{\mathrm{L2}} + r_{\mathrm{C}} + j\omega_{\mathrm{s}}L_2)\langle \underline{i}^{\mathrm{s}}_{\mathrm{L2}}\rangle + r_{\mathrm{C}}\langle \underline{i}^{\mathrm{s}}_{\mathrm{L1}}\rangle + \langle \underline{u}^{\mathrm{s}}_{\mathrm{C}}\rangle - \langle \underline{u}^{\mathrm{s}}_{\mathrm{o}}\rangle\Big], \tag{2.16}$$

and for capacitor voltage by

$$\frac{\mathrm{d}\langle \underline{u}^{\mathrm{s}}_{\mathrm{C}}\rangle}{\mathrm{d}t} = \frac{1}{C}\Big[\langle \underline{i}^{\mathrm{s}}_{\mathrm{L1}}\rangle - \langle \underline{i}^{\mathrm{s}}_{\mathrm{L2}}\rangle - j\omega_{\mathrm{s}}C\underline{u}^{\mathrm{s}}_{\mathrm{C}}\rangle\Big]. \tag{2.17}$$

The total current flowing into the inverter bridge, i.e., $i_{\mathrm{tot}} = i_{\mathrm{in}} - i_{\mathrm{Cin}}$, can be given with the inverse Park's transformation as $i_{\mathrm{tot}} = d_{\mathrm{A}}\langle i_{\mathrm{L1a}}\rangle + d_{\mathrm{B}}\langle i_{\mathrm{L1b}}\rangle + d_{\mathrm{C}}\langle i_{\mathrm{L1c}}\rangle = \frac{3}{2}\mathrm{Re}\{\underline{d}^{\mathrm{s}}\langle \underline{i}^{\mathrm{s}}_{\mathrm{L1}}\rangle^*\} = \frac{3}{2}[d_{\mathrm{d}}\langle i_{\mathrm{L1d}}\rangle + d_{\mathrm{q}}\langle i_{\mathrm{L1q}}\rangle]$ and, therefore, the input-capacitor current can be expressed as

$$\langle i_{\mathrm{Cin}}\rangle = \langle i_{\mathrm{in}}\rangle - \frac{3}{2}\Big[d_{\mathrm{d}}\langle i_{\mathrm{L1d}}\rangle + d_{\mathrm{q}}\langle i_{\mathrm{L1q}}\rangle\Big]. \tag{2.18}$$

Consequently, the time derivative for the input capacitor voltage can be expressed by

$$\frac{\mathrm{d}\langle u_{\mathrm{Cin}}\rangle}{\mathrm{d}t} = \frac{1}{C_{\mathrm{in}}}\Big[-\frac{3}{2}(d_{\mathrm{d}}\langle i_{\mathrm{L1d}}\rangle + d_{\mathrm{q}}\langle i_{\mathrm{L1q}}\rangle) + \langle i_{\mathrm{in}}\rangle\Big]. \tag{2.19}$$

Furthermore, the input voltage and the output current can be expressed by

$$\langle u_{\mathrm{in}}\rangle = \langle u_{\mathrm{Cin}}\rangle, \tag{2.20}$$

$$\langle \underline{i}^{\mathrm{s}}_{\mathrm{o}}\rangle = \langle \underline{i}^{\mathrm{s}}_{\mathrm{L2}}\rangle. \tag{2.21}$$

Considering the final steady-state formulation, Eqs. (2.15) - (2.21) in the synchronous reference frame are divided into direct and quadrature components as $\underline{x}^{\mathrm{s}}(t) = x_{\mathrm{d}}(t) + jx_{\mathrm{q}}(t)$. Note that Eq. (2.15) contains a u_{in}-term which has to be replaced by (2.20). By substituting (2.20) into (2.15) and dividing the average-valued equations into direct and quadrature components yields:

$$\begin{aligned}\frac{\mathrm{d}\langle i_{\mathrm{L1d}}\rangle}{\mathrm{d}t} = \frac{1}{L_1}\Big[&-(r_{\mathrm{eq}} + r_{\mathrm{C}})\langle i_{\mathrm{L1d}}\rangle + \omega_{\mathrm{s}}L_1\langle i_{\mathrm{L1q}}\rangle + r_{\mathrm{C}}\langle i_{\mathrm{L2d}}\rangle \\ &-\langle u_{\mathrm{Cd}}\rangle + d_{\mathrm{d}}\langle u_{\mathrm{Cin}}\rangle\Big],\end{aligned} \tag{2.22}$$

$$\frac{\mathrm{d}\langle i_{\mathrm{L1q}}\rangle}{\mathrm{d}t} = \frac{1}{L_1}\Big[-(r_{\mathrm{eq}} + r_{\mathrm{C}})\langle i_{\mathrm{L1q}}\rangle - \omega_{\mathrm{s}} L_1 \langle i_{\mathrm{L1d}}\rangle + r_{\mathrm{C}}\langle i_{\mathrm{L2q}}\rangle - \langle u_{\mathrm{Cq}}\rangle + d_{\mathrm{q}}\langle u_{\mathrm{Cin}}\rangle\Big], \tag{2.23}$$

$$\frac{\mathrm{d}\langle i_{\mathrm{L2d}}\rangle}{\mathrm{d}t} = \frac{1}{L_2}\Big[-(r_{\mathrm{L2}} + r_{\mathrm{C}})\langle i_{\mathrm{L2d}}\rangle + \omega_{\mathrm{s}} L_2 \langle i_{\mathrm{L2q}}\rangle + r_{\mathrm{C}}\langle i_{\mathrm{L1d}}\rangle + \langle u_{\mathrm{Cd}}\rangle - \langle u_{\mathrm{od}}\rangle\Big], \tag{2.24}$$

$$\frac{\mathrm{d}\langle i_{\mathrm{L2q}}\rangle}{\mathrm{d}t} = \frac{1}{L_2}\Big[-(r_{\mathrm{L2}} + r_{\mathrm{C}})\langle i_{\mathrm{L2q}}\rangle - \omega_{\mathrm{s}} L_2 \langle i_{\mathrm{L2d}}\rangle + r_{\mathrm{C}}\langle i_{\mathrm{L1q}}\rangle + \langle u_{\mathrm{Cq}}\rangle - \langle u_{\mathrm{oq}}\rangle\Big], \tag{2.25}$$

$$\frac{\mathrm{d}\langle u_{\mathrm{Cin}}\rangle}{\mathrm{d}t} = \frac{1}{C_{\mathrm{in}}}\Big[-\frac{3}{2}\Big(d_{\mathrm{d}}\langle i_{\mathrm{L1d}}\rangle + d_{\mathrm{q}}\langle i_{\mathrm{L1q}}\rangle\Big) + \langle i_{\mathrm{in}}\rangle\Big], \tag{2.26}$$

$$\frac{\mathrm{d}\langle u_{\mathrm{Cd}}\rangle}{\mathrm{d}t} = \frac{1}{C}\Big[\langle i_{\mathrm{L1d}}\rangle - \langle i_{\mathrm{L2d}}\rangle + \omega_{\mathrm{s}} C\langle u_{\mathrm{Cq}}\rangle\Big], \tag{2.27}$$

$$\frac{\mathrm{d}\langle u_{\mathrm{Cq}}\rangle}{\mathrm{d}t} = \frac{1}{C}\Big[\langle i_{\mathrm{L1q}}\rangle - \langle i_{\mathrm{L2q}}\rangle - \omega_{\mathrm{s}} C\langle u_{\mathrm{Cd}}\rangle\Big], \tag{2.28}$$

$$\langle u_{\mathrm{in}}\rangle = \langle u_{\mathrm{Cin}}\rangle, \tag{2.29}$$

$$\langle i_{\mathrm{od}}\rangle = \langle i_{\mathrm{L2d}}\rangle, \tag{2.30}$$

$$\langle i_{\mathrm{oq}}\rangle = \langle i_{\mathrm{L2q}}\rangle. \tag{2.31}$$

Eqs. (2.22) - (2.31) are known as the synchronous-reference-frame average-valued model for a current-fed VSI.

2.2 Operating point

The steady-state operating point can be obtained from the average-valued model by setting the derivatives to zero and all the variables are replaced with their average-valued terms denoted by corresponding upper case letters. As the inverter-side-inductor current is the controlled variable, which is synchronized with the point-of-common coupling (PCC) voltage, then $I_{\mathrm{L1q}} = 0$ and $U_{\mathrm{oq}} = 0$ in the steady state. The q-component of the inverter-side-inductor current (I_{L1q}) is set to zero since unity power factor is desired. However, a small amount of reactive power is transferred into the grid (i.e., $I_{\mathrm{L2q}} \neq 0$), which is usually limited by proper selection of the capacitor.

By considering the operating conditions stated above, the steady state can be derived

as

$$-R_{\mathrm{eq}}I_{\mathrm{L1d}} + r_{\mathrm{C}}I_{\mathrm{L2d}} - U_{\mathrm{Cd}} + D_{\mathrm{d}}U_{\mathrm{in}} = 0, \tag{2.32}$$

$$-k_3 I_{\mathrm{L1d}} + r_{\mathrm{C}}I_{\mathrm{L2q}} - U_{\mathrm{Cq}} + D_{\mathrm{q}}U_{\mathrm{in}} = 0, \tag{2.33}$$

$$U_{\mathrm{in}} = U_{\mathrm{Cin}}, \tag{2.34}$$

$$-\frac{3}{2}D_{\mathrm{d}}I_{\mathrm{L1d}} + I_{\mathrm{in}} = 0, \tag{2.35}$$

$$-k_1 I_{\mathrm{L2q}} - U_{\mathrm{Cd}} = 0, \tag{2.36}$$

$$k_1 I_{\mathrm{L2d}} - k_1 I_{\mathrm{L1d}} - U_{\mathrm{Cq}} = 0, \tag{2.37}$$

$$k_2 U_{\mathrm{Cq}} - k_2 R I_{\mathrm{L2q}} - I_{\mathrm{L2d}} = 0, \tag{2.38}$$

$$Rk_2 I_{\mathrm{L2d}} - k_2 r_{\mathrm{C}} I_{\mathrm{L1d}} - k_2 U_{\mathrm{Cd}} + k_2 U_{\mathrm{od}} - I_{\mathrm{L2q}} = 0, \tag{2.39}$$

where $k_1 = \frac{1}{\omega_{\mathrm{s}} C}$, $k_2 = \frac{1}{\omega_{\mathrm{s}} L_2}$, $R_{\mathrm{eq}} = r_{\mathrm{eq}} + r_{\mathrm{C}}$ and $R = r_{\mathrm{L2}} + r_{\mathrm{C}}$. Now by substituting (2.36) and (2.37) into (2.38) and (2.39) and solving for I_{L2d} and I_{L2q} yield

$$I_{\mathrm{L2d}} = \frac{2I_{\mathrm{in}}K_{\mathrm{ILd}} - 3D_{\mathrm{d}}RU_{\mathrm{od}}}{3D_{\mathrm{d}}K} \tag{2.40}$$

and

$$I_{\mathrm{L2q}} = -\frac{2I_{\mathrm{in}}K_{\mathrm{ILq}} + 3D_{\mathrm{d}}RU_{\mathrm{od}}K_{\mathrm{Uo}}}{3D_{\mathrm{d}}K}, \tag{2.41}$$

where $K_{\mathrm{ILd}} = k_1^2 - k_1 k_2 + Rr_{\mathrm{C}}$, $K_{\mathrm{ILq}} = k_2 r_{\mathrm{C}} + k_1 R - k_1 r_{\mathrm{C}}$, $K_{\mathrm{Uo}} = k_1 - k_2$ and $K = R^2 + (k_1 - k_2)^2$. The steady-state for D_{d} and D_{q} can be calculated by substituting (2.40) and (2.41) into (2.32) and (2.33), respectively. Appendix A provides a complete MATLAB-code for calculating the steady state with parasitics. Simplified values for D_{d} and D_{q} without the parasitic elements can be given by

$$D_{\mathrm{d}} = \frac{U_{\mathrm{od}}}{U_{\mathrm{in}}\left(1 - CL_2\omega_{\mathrm{s}}^2\right)}, \tag{2.42}$$

$$D_{\mathrm{q}} = \frac{2}{3}\frac{I_{\mathrm{in}}\omega_{\mathrm{s}}\left(L_1 + L_2 - L_1L_2C\omega_{\mathrm{s}}^2\right)}{U_{\mathrm{od}}}. \tag{2.43}$$

The linearization process is described in detail in the next section.

2.3 Linearized model

As can be seen from the average-valued model, some equations contain two input or state variables multiplied with each other, e.g. $\underline{d}\langle u_{\mathrm{Cin}}\rangle$. Therefore, the average model, in this case, is actually nonlinear and does not suffice for a small-signal model due to presence of nonlinear dependency between variables. Thus, the equations are linearized by calculating partial derivatives for each state, input and output variables thus removing the aforementioned nonlinearity. Accordingly, the obtained linearized equations can be given by

$$\frac{\mathrm{d}\hat{i}_{\mathrm{L1d}}}{\mathrm{d}t} = \frac{1}{L_1}\Big[-(r_{\mathrm{eq}}+r_{\mathrm{C}})\hat{i}_{\mathrm{L1d}} + \omega_{\mathrm{s}}L_1\hat{i}_{\mathrm{L1q}} + r_{\mathrm{C}}\hat{i}_{\mathrm{L2d}} - \hat{u}_{\mathrm{Cd}} + D_{\mathrm{d}}\hat{u}_{\mathrm{Cin}} + U_{\mathrm{in}}\hat{d}_{\mathrm{d}}\Big], \tag{2.44}$$

$$\frac{\mathrm{d}\hat{i}_{\mathrm{L1q}}}{\mathrm{d}t} = \frac{1}{L_1}\Big[-(r_{\mathrm{eq}}+r_{\mathrm{C}})\hat{i}_{\mathrm{L1q}} - \omega_{\mathrm{s}}L_1\hat{i}_{\mathrm{L1d}} + r_{\mathrm{C}}\hat{i}_{\mathrm{L2q}} - \hat{u}_{\mathrm{Cq}} + D_{\mathrm{q}}\hat{u}_{\mathrm{Cin}} + U_{\mathrm{in}}\hat{d}_{\mathrm{q}}\Big], \tag{2.45}$$

$$\frac{\mathrm{d}\hat{i}_{\mathrm{L2d}}}{\mathrm{d}t} = \frac{1}{L_2}\Big[-(r_{\mathrm{L2}}+r_{\mathrm{C}})\hat{i}_{\mathrm{L2d}} + \omega_{\mathrm{s}}L_2\hat{i}_{\mathrm{L2q}} + r_{\mathrm{C}}\hat{i}_{\mathrm{L1d}} + \hat{u}_{\mathrm{Cd}} - \hat{u}_{\mathrm{od}}\Big], \tag{2.46}$$

$$\frac{\mathrm{d}\hat{i}_{\mathrm{L2q}}}{\mathrm{d}t} = \frac{1}{L_2}\Big[-(r_{\mathrm{L2}}+r_{\mathrm{C}})\hat{i}_{\mathrm{L2q}} - \omega_{\mathrm{s}}L_2\hat{i}_{\mathrm{L2d}} + r_{\mathrm{C}}\hat{i}_{\mathrm{L1q}} + \hat{u}_{\mathrm{Cq}} - \hat{u}_{\mathrm{oq}}\Big], \tag{2.47}$$

$$\frac{\mathrm{d}\hat{u}_{\mathrm{Cin}}}{\mathrm{d}t} = \frac{1}{C_{\mathrm{in}}}\Big[-\frac{3}{2}D_{\mathrm{d}}\hat{i}_{\mathrm{L1d}} - \frac{3}{2}D_{\mathrm{q}}\hat{i}_{\mathrm{L1q}} + \hat{i}_{\mathrm{in}} - \frac{I_{\mathrm{in}}}{D_{\mathrm{d}}}\hat{d}_{\mathrm{d}}\Big], \tag{2.48}$$

$$\frac{\mathrm{d}\hat{u}_{\mathrm{Cd}}}{\mathrm{d}t} = \frac{1}{C}\Big[\hat{i}_{\mathrm{L1d}} - \hat{i}_{\mathrm{L2d}} + \omega_{\mathrm{s}}C\hat{u}_{\mathrm{Cq}}\Big], \tag{2.49}$$

$$\frac{\mathrm{d}\hat{u}_{\mathrm{Cq}}}{\mathrm{d}t} = \frac{1}{C}\Big[\hat{i}_{\mathrm{L1q}} - \hat{i}_{\mathrm{L2q}} - \omega_{\mathrm{s}}C\hat{u}_{\mathrm{Cd}}\Big], \tag{2.50}$$

$$\hat{u}_{\mathrm{in}} = \hat{u}_{\mathrm{Cin}}, \tag{2.51}$$

$$\hat{i}_{\mathrm{od}} = \hat{i}_{\mathrm{L2d}}, \tag{2.52}$$

$$\hat{i}_{\mathrm{oq}} = \hat{i}_{\mathrm{L2q}}. \tag{2.53}$$

According to (2.44) - (2.53), a linearized state-space can be formulated as

$$\begin{aligned} \frac{\mathrm{d}\underline{\hat{x}}(t)}{\mathrm{d}t} &= \mathbf{A}\underline{\hat{x}}(t) + \mathbf{B}\underline{\hat{u}}(t) \\ \underline{\hat{y}}(t) &= \mathbf{C}\underline{\hat{x}}(t) + \mathbf{D}\underline{\hat{u}}(t) \end{aligned} \tag{2.54}$$

where $\underline{\hat{x}} = [\hat{i}_{\mathrm{L1d}}, \hat{i}_{\mathrm{L1q}}, \hat{i}_{\mathrm{L2d}}, \hat{i}_{\mathrm{L2q}}, \hat{u}_{\mathrm{Cd}}, \hat{u}_{\mathrm{Cq}}, \hat{u}_{\mathrm{Cin}}]^{\mathrm{T}}$ represents a vector of state variables, $\underline{\hat{u}} = [\hat{i}_{\mathrm{in}}, \hat{u}_{\mathrm{od}}, \hat{u}_{\mathrm{oq}}, \hat{d}_{\mathrm{d}}, \hat{d}_{\mathrm{q}}]^{\mathrm{T}}$ represents a vector of input variables and $\underline{\hat{y}}$=[$\hat{u}_{\mathrm{in}}$, $\hat{i}_{\mathrm{L1d}}$, $\hat{i}_{\mathrm{L1q}}$, $\hat{i}_{\mathrm{od}}$, $\hat{i}_{\mathrm{oq}}$]$^{\mathrm{T}}$ is the vector for output variables. The state matrices in (2.54) can be given according to (2.44)-(2.53) by

$$\mathbf{A} = \begin{bmatrix} -\frac{r_{\mathrm{eq}}}{L_1} & \omega_{\mathrm{s}} & \frac{r_{\mathrm{C}}}{L_1} & 0 & -\frac{1}{L_1} & 0 & \frac{D_{\mathrm{d}}}{L_1} \\ -\omega_{\mathrm{s}} & -\frac{r_{\mathrm{eq}}}{L_1} & 0 & \frac{r_{\mathrm{C}}}{L_1} & 0 & -\frac{1}{L_1} & \frac{D_{\mathrm{q}}}{L_1} \\ \frac{r_{\mathrm{C}}}{L_2} & 0 & -\frac{r_{\mathrm{L2}}+r_{\mathrm{C}}}{L_2} & \omega_{\mathrm{s}} & \frac{1}{L_2} & 0 & 0 \\ 0 & \frac{r_{\mathrm{C}}}{L_2} & -\omega_{\mathrm{s}} & -\frac{r_{\mathrm{L2}}+r_{\mathrm{C}}}{L_2} & 0 & \frac{1}{L_2} & 0 \\ \frac{1}{C_{\mathrm{f}}} & 0 & -\frac{1}{C_{\mathrm{f}}} & 0 & 0 & \omega_{\mathrm{s}} & 0 \\ 0 & \frac{1}{C_{\mathrm{f}}} & 0 & -\frac{1}{C_{\mathrm{f}}} & -\omega_{\mathrm{s}} & 0 & 0 \\ -\frac{3}{2}\frac{D_{\mathrm{d}}}{C_{\mathrm{in}}} & -\frac{3}{2}\frac{D_{\mathrm{q}}}{C_{\mathrm{in}}} & 0 & 0 & 0 & 0 & 0 \end{bmatrix} \tag{2.55}$$

$$\mathbf{B} = \begin{bmatrix} 0 & 0 & 0 & \frac{U_{\mathrm{in}}}{L_1} & 0 \\ 0 & 0 & 0 & 0 & \frac{U_{\mathrm{in}}}{L_1} \\ 0 & -\frac{1}{L_2} & 0 & 0 & 0 \\ 0 & 0 & -\frac{1}{L_2} & 0 & 0 \\ 0 & 0 & 0 & 0 & 0 \\ 0 & 0 & 0 & 0 & 0 \\ \frac{1}{C_{\mathrm{in}}} & 0 & 0 & -\frac{I_{\mathrm{in}}}{D_{\mathrm{d}}C_{\mathrm{in}}} & 0 \end{bmatrix} \tag{2.56}$$

$$\mathbf{C} = \begin{bmatrix} 0 & 0 & 0 & 0 & 1 \\ 1 & 0 & 0 & 0 & 0 \\ 0 & 1 & 0 & 0 & 0 \\ 0 & 0 & 1 & 0 & 0 \\ 0 & 0 & 0 & 1 & 0 \end{bmatrix} \tag{2.57}$$

$$\mathbf{D} = \mathbf{0} \tag{2.58}$$

The linearized state-space can be given in the Laplace domain by replacing the derivative operator 'd/dt' with the Laplace-operator 's'.

$$\begin{aligned} s\boldsymbol{X}(s) &= \mathbf{A}\boldsymbol{X}(s) + \mathbf{B}\boldsymbol{U}(s) \\ \boldsymbol{Y}(s) &= \mathbf{C}\boldsymbol{X}(s) + \mathbf{D}\boldsymbol{U}(s) \end{aligned}. \tag{2.59}$$

In order to finalize the small-signal modeling procedure, the transfer functions between input and output variables can be solved according to (2.59) as

$$\boldsymbol{Y}(s) = \left[\mathbf{C}(s\mathbf{I} - \mathbf{A})^{-1}\mathbf{B} + \mathbf{D}\right]\boldsymbol{U}(s) = \mathbf{G}_{\mathrm{H}}\boldsymbol{U}(s). \tag{2.60}$$

The transfer function matrix $\mathbf{G}_{\mathrm{H}}$ is known as the H-parameter representation, i.e., when the inverter is analyzed as current-input-current-output system, which was discussed earlier considering the terminal constraints of the converter. Transfer functions of the system can be given by

$$\begin{bmatrix} \hat{u}_{\mathrm{in}} \\ \hat{i}_{\mathrm{L1d}} \\ \hat{i}_{\mathrm{L1q}} \\ \hat{i}_{\mathrm{od}} \\ \hat{i}_{\mathrm{oq}} \end{bmatrix} = \overbrace{\begin{bmatrix} Z^{\mathrm{H}}_{\mathrm{in}} & T^{\mathrm{H}}_{\mathrm{oi\text{-}d}} & T^{\mathrm{H}}_{\mathrm{oi\text{-}q}} & G^{\mathrm{H}}_{\mathrm{ci\text{-}d}} & G^{\mathrm{H}}_{\mathrm{ci\text{-}q}} \\ G^{\mathrm{H}}_{\mathrm{ioL\text{-}d}} & G^{\mathrm{H}}_{\mathrm{oL\text{-}d}} & G^{\mathrm{H}}_{\mathrm{oL\text{-}qd}} & G^{\mathrm{H}}_{\mathrm{cL\text{-}d}} & G^{\mathrm{H}}_{\mathrm{cL\text{-}qd}} \\ G^{\mathrm{H}}_{\mathrm{ioL\text{-}q}} & G^{\mathrm{H}}_{\mathrm{oL\text{-}dq}} & G^{\mathrm{H}}_{\mathrm{oL\text{-}q}} & G^{\mathrm{H}}_{\mathrm{cL\text{-}dq}} & G^{\mathrm{H}}_{\mathrm{cL\text{-}q}} \\ G^{\mathrm{H}}_{\mathrm{io\text{-}d}} & -Y^{\mathrm{H}}_{\mathrm{o\text{-}d}} & -Y^{\mathrm{H}}_{\mathrm{o\text{-}qd}} & G^{\mathrm{H}}_{\mathrm{co\text{-}d}} & G^{\mathrm{H}}_{\mathrm{co\text{-}qd}} \\ G^{\mathrm{H}}_{\mathrm{io\text{-}q}} & -Y^{\mathrm{H}}_{\mathrm{o\text{-}dq}} & -Y^{\mathrm{H}}_{\mathrm{o\text{-}q}} & G^{\mathrm{H}}_{\mathrm{co\text{-}dq}} & G^{\mathrm{H}}_{\mathrm{co\text{-}q}} \end{bmatrix}}^{\mathbf{G}_{\mathrm{H}}} \begin{bmatrix} \hat{i}_{\mathrm{in}} \\ \hat{u}_{\mathrm{od}} \\ \hat{u}_{\mathrm{oq}} \\ \hat{d}_{\mathrm{d}} \\ \hat{d}_{\mathrm{q}} \end{bmatrix}. \tag{2.61}$$

Considering the second and third rows of the matrix, the subscript 'L' denotes inverter-side-current-related transfer functions, which are intermediate output variables. Note that the topology of the converter dictates that the current should flow outwards into

the grid, but the output admittance is determined by the current flowing in it, which is the opposite regarding the originally selected direction in Fig. 2.1. Therefore, the output voltage $u_{\text{o-(d,q)}}$ actually perturbs a current opposite in sign and the corresponding admittances $Y^{\text{H}}_{\text{o-d}}$, $Y^{\text{H}}_{\text{o-qd}}$, $Y^{\text{H}}_{\text{o-dq}}$ and $Y^{\text{H}}_{\text{o-q}}$ have to multiplied by a coefficient '-1'.

In multi-variable systems, e.g., in the *dq*-domain analysis, the inputs, states and outputs can have n channels. Correspondingly, variables can be given as one vector consisting of two or more channels as $\underline{x} = [x_1, x_2, \cdots, x_n]^{\text{T}}$. Naturally for the *dq*-domain, $\underline{x}^{\text{s}} = [x_{\text{d}}, x_{\text{q}}]^{\text{T}}$, i.e., $n = 2$. Consequently, transfer functions between input and output variable vectors can be modeled as $n \times n$ matrices, that is [76, 77]

$$\mathbf{G}(s) = \begin{bmatrix} G_{11} & \cdots & G_{1n} \\ \vdots & \ddots & G_{2n} \\ G_{n1} & G_{n2} & G_{nn} \end{bmatrix}. \tag{2.62}$$

The transfer matrix $\mathbf{G}_{\text{H}}$ in (2.61) can be, thus, simplified and presented by using transfer matrices due to the inherent multi-variable nature of the inverter [52, 76–79]. By combining the d and q-components and their cross-coupling terms into two-by-two matrices, the transfer function matrix $\mathbf{G}_{\text{H}}$ in (2.61) can be given as

$$\mathbf{G}_{\text{H}} = \begin{bmatrix} Z_{\text{in}} & \mathbf{T}_{\text{oi}} & \mathbf{G}_{\text{ci}} \\ \mathbf{G}_{\text{ioL}} & \mathbf{G}_{\text{oL}} & \mathbf{G}_{\text{cL}} \\ \mathbf{G}_{\text{io}} & -\mathbf{Y}_{\text{o}} & \mathbf{G}_{\text{co}} \end{bmatrix}. \tag{2.63}$$

Note that according to topological properties of the inverter in Fig. 2.1, the input voltage $\hat{u}_{\text{in}}$ and the input current $\hat{i}_{\text{in}}$ are scalar variables, hence, the input impedance Z_{in} in (2.63) is also a scalar.

Regarding the dynamical representation of the system, i.e. individual input-to-output responses, corresponding transfer functions are presented for output variables with separate components as well as with the multi-variable representation in (2.64)-(2.71) according to (2.61) and (2.63), respectively.

$$\hat{u}_{\text{in}} = Z^{\text{H}}_{\text{in}}\hat{i}_{\text{in}} + T^{\text{H}}_{\text{oi-d}}\hat{u}_{\text{od}} + T^{\text{H}}_{\text{oi-q}}\hat{u}_{\text{oq}} + G^{\text{H}}_{\text{ci-d}}\hat{d}_{\text{d}} + G^{\text{H}}_{\text{ci-q}}\hat{d}_{\text{q}} \tag{2.64}$$

$$\hat{u}_{\text{in}} = Z_{\text{in}}\hat{i}_{\text{in}} + \mathbf{T}_{\text{oi}}\underline{\hat{u}}_{\text{o}} + \mathbf{G}_{\text{ci}}\underline{\hat{d}} \tag{2.65}$$

$$\hat{i}_{\mathrm{L1d}} = G^{\mathrm{H}}_{\mathrm{ioL\text{-}d}}\hat{i}_{\mathrm{in}} + G^{\mathrm{H}}_{\mathrm{oL\text{-}d}}\hat{u}_{\mathrm{od}} + G^{\mathrm{H}}_{\mathrm{oL\text{-}qd}}\hat{u}_{\mathrm{oq}} + G^{\mathrm{H}}_{\mathrm{cL\text{-}d}}\hat{d}_{\mathrm{d}} + G^{\mathrm{H}}_{\mathrm{cL\text{-}qd}}\hat{d}_{\mathrm{q}} \tag{2.66}$$

$$\hat{i}_{\mathrm{L1q}} = G^{\mathrm{H}}_{\mathrm{ioL\text{-}q}}\hat{i}_{\mathrm{in}} + G^{\mathrm{H}}_{\mathrm{oL\text{-}dq}}\hat{u}_{\mathrm{od}} + G^{\mathrm{H}}_{\mathrm{oL\text{-}q}}\hat{u}_{\mathrm{oq}} + G^{\mathrm{H}}_{\mathrm{cL\text{-}dq}}\hat{d}_{\mathrm{d}} + G^{\mathrm{H}}_{\mathrm{cL\text{-}q}}\hat{d}_{\mathrm{q}} \tag{2.67}$$

$$\underline{\hat{i}}_{\mathrm{L1}} = \mathbf{G}_{\mathrm{ioL}}\hat{i}_{\mathrm{in}} + \mathbf{G}_{\mathrm{oL}}\underline{\hat{u}}_{\mathrm{o}} + \mathbf{G}_{\mathrm{cL}}\underline{\hat{d}} \tag{2.68}$$

$$\hat{i}_{\mathrm{od}} = G^{\mathrm{H}}_{\mathrm{io\text{-}d}}\hat{i}_{\mathrm{in}} - Y^{\mathrm{H}}_{\mathrm{o\text{-}d}}\hat{u}_{\mathrm{od}} - Y^{\mathrm{H}}_{\mathrm{o\text{-}qd}}\hat{u}_{\mathrm{oq}} + G^{\mathrm{H}}_{\mathrm{co\text{-}d}}\hat{d}_{\mathrm{d}} + G^{\mathrm{H}}_{\mathrm{co\text{-}qd}}\hat{d}_{\mathrm{q}} \tag{2.69}$$

$$\hat{i}_{\mathrm{oq}} = G^{\mathrm{H}}_{\mathrm{io\text{-}q}}\hat{i}_{\mathrm{in}} - Y^{\mathrm{H}}_{\mathrm{o\text{-}dq}}\hat{u}_{\mathrm{od}} - Y^{\mathrm{H}}_{\mathrm{o\text{-}q}}\hat{u}_{\mathrm{oq}} + G^{\mathrm{H}}_{\mathrm{co\text{-}dq}}\hat{d}_{\mathrm{d}} + G^{\mathrm{H}}_{\mathrm{co\text{-}q}}\hat{d}_{\mathrm{q}} \tag{2.70}$$

$$\underline{\hat{i}}_{\mathrm{L2}} = \mathbf{G}_{\mathrm{io}}\hat{i}_{\mathrm{in}} - \mathbf{Y}_{\mathrm{o}}\underline{\hat{u}}_{\mathrm{o}} + \mathbf{G}_{\mathrm{co}}\underline{\hat{d}} \tag{2.71}$$

In the aforementioned open-loop output dynamics, considering (2.64) and (2.65), Z_{in} is the input impedance of the system, $T_{\mathrm{oi\text{-}(d,q)}}$ is known as the reverse transfer function and $G_{\mathrm{ci\text{-}(d,q)}}$ is the control-to-input-voltage transfer function. Output current dynamics can be presented by (2.66)-(2.68) for the inverter-side current and by (2.69)-(2.71) for the grid current. Accordingly, $G_{\mathrm{io,ioL\text{-}(d,q)}}$ represent the input-to-output transfer function or the forward current gain, $Y_{\mathrm{o\text{-}(d,q,qd,dq)}}$ is the output admittance with cross-coupling elements, $G_{\mathrm{oL\text{-}(d,q,qd,dq)}}$ is the output-to-inductor current transfer function with cross-coupling elements, $G_{\mathrm{co,cL\text{-}(d,q,qd,dq)}}$ is known as the control-to-output-current transfer function, which also includes cross-coupling terms between components as shown in (2.66)-(2.71).

A linear network model, which characterizes the terminal and dynamical behavior of the converter, depicted in Fig. 2.3, can be presented according to the transfer function matrix (2.63). The effect of the non-ideal source and load is included as a parallel input admittance Y_{s} and a series grid impedance $\mathbf{Z}_{\mathrm{g}}$, respectively. Moreover, the CL-part of the filter is shown separately for demonstrative purposes in order to highlight the intermediate-output-variable-like nature of the inverter-side inductor current. Accordingly, the aforementioned linear network model needs to be further elaborated as the CL-part and corresponding transfer functions are not yet determined.

The small-signal model of the CL-filter can be derived according to Fig. 2.4, where the filter input variables are the inverter-side inductor currents $i_{\mathrm{L1(a,b,c)}}$ and the grid phase-voltages $u_{\mathrm{o(a,b,c)n}}$. Furthermore, the filter output variables are the voltages across the capacitors $u_{\mathrm{C(a,b,c)}}$ and the output currents $i_{\mathrm{L2(a,b,c)}}$. Accordingly, by applying well-known averaging methods shown earlier, state matrices for the CL-filter can be given by

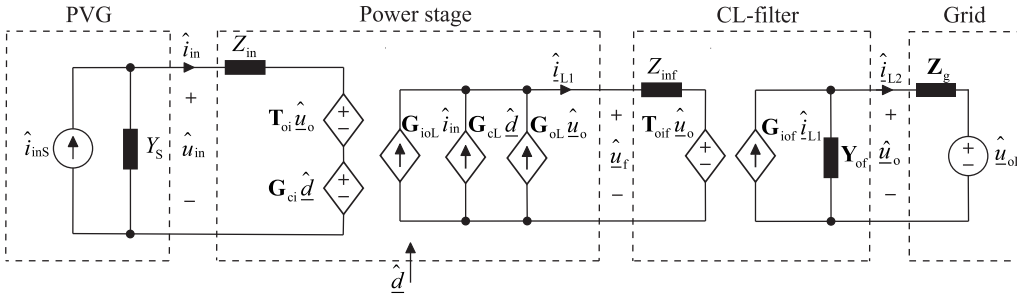

Fig. 2.3: Source-load-affected open-loop model of a three-phase grid-connected PV inverter.

$$\mathbf{A}_{\mathrm{f}} = \begin{bmatrix} -\frac{r_{\mathrm{L2}}+r_{\mathrm{C}}}{L_2} & \omega_{\mathrm{s}} & \frac{1}{L_2} & 0 \\ -\omega_{\mathrm{s}} & -\frac{r_{\mathrm{L2}}+r_{\mathrm{C}}}{L_2} & 0 & \frac{1}{L_2} \\ \frac{1}{C} & 0 & 0 & 0 \\ 0 & \frac{1}{C} & 0 & 0 \end{bmatrix}, \tag{2.72}$$

$$\mathbf{B}_{\mathrm{f}} = \begin{bmatrix} \frac{r_{\mathrm{C}}}{L_2} & 0 & \frac{1}{L_2} & 0 \\ 0 & \frac{r_{\mathrm{C}}}{L_2} & 0 & -\frac{1}{L_2} \\ 1 & 0 & 0 & 0 \\ 0 & 1 & 0 & 0 \end{bmatrix}, \tag{2.73}$$

$$\mathbf{C}_{\mathrm{f}} = \begin{bmatrix} -r_{\mathrm{C}} & 0 & 1 & 0 \\ 0 & -r_{\mathrm{C}} & 0 & 1 \\ 1 & 0 & 0 & 0 \\ 0 & 1 & 0 & 0 \end{bmatrix}, \tag{2.74}$$

$$\mathbf{D}_{\mathrm{f}} = \begin{bmatrix} r_{\mathrm{C}} & 0 & 0 & 0 \\ 0 & r_{\mathrm{C}} & 0 & 0 \\ 0 & 0 & 0 & 0 \\ 0 & 0 & 0 & 0 \end{bmatrix}. \tag{2.75}$$

Clearly, switches are absent from the filter model and, therefore, only one linear circuit is present. The obtained average-valued model is, in fact, also the linear representation of the filter. Accordingly, the transfer function matrix of the filter can be given by

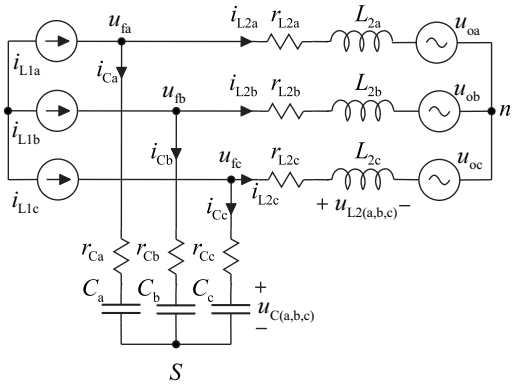

Fig. 2.4: Linear model of a CL-type filter.

$$\begin{bmatrix} \hat{u}_{\mathrm{fd}} \\ \hat{u}_{\mathrm{fq}} \\ \hat{i}_{\mathrm{L2d}} \\ \hat{i}_{\mathrm{L2q}} \end{bmatrix} = \begin{bmatrix} Z_{\mathrm{inf-d}} & Z_{\mathrm{inf-qd}} & T_{\mathrm{oif-d}} & T_{\mathrm{oif-qd}} \\ Z_{\mathrm{inf-dq}} & Z_{\mathrm{inf-q}} & T_{\mathrm{oif-dq}} & T_{\mathrm{oif-q}} \\ G_{\mathrm{iof-d}} & G_{\mathrm{iof-qd}} & -Y_{\mathrm{of-d}} & -Y_{\mathrm{of-qd}} \\ G_{\mathrm{iof-dq}} & G_{\mathrm{iof-q}} & -Y_{\mathrm{of-dq}} & -Y_{\mathrm{of-q}} \end{bmatrix} \begin{bmatrix} \hat{i}_{\mathrm{L1d}} \\ \hat{i}_{\mathrm{L1q}} \\ \hat{u}_{\mathrm{od}} \\ \hat{u}_{\mathrm{oq}} \end{bmatrix} \tag{2.76}$$

Similarly, it should be noted that Eq. (2.76) can be also presented by using the multi-variable notation by

$$\begin{bmatrix} \underline{\hat{u}}_{\mathrm{f}} \\ \underline{\hat{i}}_{\mathrm{L2}} \end{bmatrix} = \begin{bmatrix} \mathbf{Z}_{\mathrm{inf}} & \mathbf{T}_{\mathrm{oif}} \\ \mathbf{G}_{\mathrm{iof}} & -\mathbf{Y}_{\mathrm{of}} \end{bmatrix} \begin{bmatrix} \underline{\hat{i}}_{\mathrm{L1}} \\ \underline{\hat{u}}_{\mathrm{o}} \end{bmatrix} \tag{2.77}$$

Matrices in (2.77) are used to represent the open-loop dynamics of a CL-filter shown in Fig. 2.3.

2.4 Source-affected model

Photovoltaic generator induces varying dynamical resistance (r_{pv}) connected across the input terminal of the converter. This has to be considered in the dynamical model in order to analyze the converter dynamics correctly [4]. As shown in Fig. 2.3, a non-ideal source with finite admittance Y_{s} is assumed here, which can be included in the open-loop dynamics of the system. Accordingly, the real input current ($\hat{i}_{\mathrm{in}}$) of the converter is affected by the non-ideal source current $\hat{i}_{\mathrm{inS}}$ as well as the parallel admittance Y_{s} and can be expressed as

$$\hat{i}_{\mathrm{in}} = \hat{i}_{\mathrm{inS}} - Y_{\mathrm{s}}\hat{u}_{\mathrm{in}}. \tag{2.78}$$

Consequently, the input voltage dynamics can be presented by substituting (2.78) into the nominal open-loop input voltage dynamics as

$$\begin{aligned} \hat{u}_{\mathrm{in}} &= Z_{\mathrm{in}}\left(\hat{i}_{\mathrm{inS}} - Y_{\mathrm{s}}\hat{u}_{\mathrm{in}}\right) + \mathbf{T}_{\mathrm{oi}}\underline{\hat{u}}_{\mathrm{o}} + \mathbf{G}_{\mathrm{ci}}\underline{\hat{d}}, \\ \hat{u}_{\mathrm{in}} &= \tfrac{Z_{\mathrm{in}}}{1+Z_{\mathrm{in}}Y_{\mathrm{s}}}\hat{i}_{\mathrm{inS}} + \tfrac{\mathbf{T}_{\mathrm{oi}}}{1+Z_{\mathrm{in}}Y_{\mathrm{s}}}\underline{\hat{u}}_{\mathrm{o}} + \tfrac{\mathbf{G}_{\mathrm{ci}}}{1+Z_{\mathrm{in}}Y_{\mathrm{s}}}\underline{\hat{d}}. \end{aligned} \tag{2.79}$$

The source-affected input current can be expressed as in (2.80), which is then substituted into the open-loop dynamics of the inverter and grid currents.

$$\hat{i}_{\mathrm{in}} = \left(1 - \frac{Z_{\mathrm{in}}Y_{\mathrm{s}}}{1+Z_{\mathrm{in}}Y_{\mathrm{s}}}\right)\hat{i}_{\mathrm{inS}} - \frac{Y_{\mathrm{s}}\mathbf{T}_{\mathrm{oi}}}{1+Z_{\mathrm{in}}Y_{\mathrm{s}}}\underline{\hat{u}}_{\mathrm{o}} - \frac{Y_{\mathrm{s}}\mathbf{G}_{\mathrm{ci}}}{1+Z_{\mathrm{in}}Y_{\mathrm{s}}}\underline{\hat{d}}. \tag{2.80}$$

Accordingly, the source-affected dynamics for input voltage, inductor current and grid current can be given by

$$\hat{u}_{\mathrm{in}} = \frac{Z_{\mathrm{in}}}{1+Z_{\mathrm{in}}Y_{\mathrm{s}}}\hat{i}_{\mathrm{inS}} + \frac{\mathbf{T}_{\mathrm{oi}}}{1+Z_{\mathrm{in}}Y_{\mathrm{s}}}\underline{\hat{u}}_{\mathrm{o}} + \frac{\mathbf{G}_{\mathrm{ci}}}{1+Z_{\mathrm{in}}Y_{\mathrm{s}}}\underline{\hat{d}}, \tag{2.81}$$

$$\begin{aligned} \underline{\hat{i}}_{\mathrm{L1}} = \mathbf{G}_{\mathrm{ioL}}\left(1 - \frac{Z_{\mathrm{in}}Y_{\mathrm{s}}}{1+Z_{\mathrm{in}}Y_{\mathrm{s}}}\right)\hat{i}_{\mathrm{inS}} + \left(\mathbf{G}_{\mathrm{oL}} - \mathbf{G}_{\mathrm{ioL}}\frac{Y_{\mathrm{s}}\mathbf{T}_{\mathrm{oi}}}{1+Z_{\mathrm{in}}Y_{\mathrm{s}}}\right)\underline{\hat{u}}_{\mathrm{o}} \\ + \left(\mathbf{G}_{\mathrm{cL}} - \mathbf{G}_{\mathrm{ioL}}\frac{Y_{\mathrm{s}}\mathbf{G}_{\mathrm{ci}}}{1+Z_{\mathrm{in}}Y_{\mathrm{s}}}\right)\underline{\hat{d}}, \end{aligned} \tag{2.82}$$

$$\begin{aligned} \underline{\hat{i}}_{\mathrm{L2}} = \mathbf{G}_{\mathrm{io}}\left(1 - \frac{Z_{\mathrm{in}}Y_{\mathrm{s}}}{1+Z_{\mathrm{in}}Y_{\mathrm{s}}}\right)\hat{i}_{\mathrm{inS}} - \left(\mathbf{Y}_{\mathrm{o}} + \mathbf{G}_{\mathrm{io}}\frac{Y_{\mathrm{s}}\mathbf{T}_{\mathrm{oi}}}{1+Z_{\mathrm{in}}Y_{\mathrm{s}}}\right)\underline{\hat{u}}_{\mathrm{o}} \\ + \left(\mathbf{G}_{\mathrm{co}} - \mathbf{G}_{\mathrm{io}}\frac{Y_{\mathrm{s}}\mathbf{G}_{\mathrm{ci}}}{1+Z_{\mathrm{in}}Y_{\mathrm{s}}}\right)\underline{\hat{d}}. \end{aligned} \tag{2.83}$$

The source-affected transfer function matrix can be given according to (2.81)-(2.83) by

$$\begin{bmatrix} Z_{\mathrm{in}}^{\mathrm{s}} & \mathbf{T}_{\mathrm{oi}}^{\mathrm{s}} & \mathbf{G}_{\mathrm{ci}}^{\mathrm{s}} \\ \mathbf{G}_{\mathrm{ioL}}^{\mathrm{s}} & \mathbf{G}_{\mathrm{oL}}^{\mathrm{s}} & \mathbf{G}_{\mathrm{cL}}^{\mathrm{s}} \\ \mathbf{G}_{\mathrm{io}}^{\mathrm{s}} & \mathbf{Y}_{\mathrm{o}}^{\mathrm{s}} & \mathbf{G}_{\mathrm{co}}^{\mathrm{s}} \end{bmatrix}$$

$$= \begin{bmatrix} \frac{Z_{\mathrm{in}}}{1+Z_{\mathrm{in}}Y_{\mathrm{s}}} & \frac{\mathbf{T}_{\mathrm{oi}}}{1+Z_{\mathrm{in}}Y_{\mathrm{s}}} & \frac{\mathbf{G}_{\mathrm{ci}}}{1+Z_{\mathrm{in}}Y_{\mathrm{s}}} \\ \mathbf{G}_{\mathrm{ioL}}\left(1-\frac{Z_{\mathrm{in}}Y_{\mathrm{s}}}{1+Z_{\mathrm{in}}Y_{\mathrm{s}}}\right) & \mathbf{G}_{\mathrm{oL}}-\mathbf{G}_{\mathrm{ioL}}\frac{Y_{\mathrm{s}}\mathbf{T}_{\mathrm{oi}}}{1+Z_{\mathrm{in}}Y_{\mathrm{s}}} & \mathbf{G}_{\mathrm{cL}}-\mathbf{G}_{\mathrm{ioL}}\frac{Y_{\mathrm{s}}\mathbf{G}_{\mathrm{ci}}}{1+Z_{\mathrm{in}}Y_{\mathrm{s}}} \\ \mathbf{G}_{\mathrm{io}}\left(1-\frac{Z_{\mathrm{in}}Y_{\mathrm{s}}}{1+Z_{\mathrm{in}}Y_{\mathrm{s}}}\right) & -\mathbf{Y}_{\mathrm{o}}-\mathbf{G}_{\mathrm{io}}\frac{Y_{\mathrm{s}}\mathbf{T}_{\mathrm{oi}}}{1+Z_{\mathrm{in}}Y_{\mathrm{s}}} & \mathbf{G}_{\mathrm{co}}-\mathbf{G}_{\mathrm{io}}\frac{Y_{\mathrm{s}}\mathbf{G}_{\mathrm{ci}}}{1+Z_{\mathrm{in}}Y_{\mathrm{s}}} \end{bmatrix}. \tag{2.84}$$

The impedance-based stability analysis, elaborated in Chapter 4, can be carried out for the input interface by investigating the impedance ratio (i.e., the minor loop gain) $Z_{\mathrm{in}}/Z_{\mathrm{s}}, Z_{\mathrm{s}} = 1/Y_{\mathrm{s}}$. However, this is not in the scope of this thesis and is not discussed further.

2.5 Load-affected model

So far, an ideal load (i.e., the utility grid) has been assumed in the analysis, which translates to a zero series impedance with the stiff voltage load. However, a real grid contains a finite input impedance, which can significantly affect the behavior of the interconnected inverter and, therefore, the effect of the load should be considered as a part of the converter dynamic model [50]. The procedure shown here yields the load-affected model, which can be utilized to analyze the effect of the grid on an arbitrary system transfer function.

The non-ideal load is shown in Fig. 2.3 as a series impedance $\mathbf{Z}_{\mathrm{g}}$ with the real grid voltage $\underline{\hat{u}}_{\mathrm{oL}}$. It is assumed that no parallel components in the load impedance are present for simplicity. Interactions at the output terminal may occur as the output current of the converter affects the voltage at the PCC ($\underline{\hat{u}}_{\mathrm{o}}$) via the grid impedance. Correspondingly, the grid voltage $\underline{\hat{u}}_{\mathrm{oL}}$ affects the output current via the output admittance $\mathbf{Y}_{\mathrm{o}}$.

Regarding the derivation of the load-affected small-signal model, Fig. 2.5 is used instead of Fig. 2.3 in order to express the load-affected transfer functions according to their nominal open-loop counterparts shown in (2.63). The grid current can be expressed according to Fig. 2.5 by

$$\underline{\hat{i}}_{\mathrm{o}} = \mathbf{G}_{\mathrm{io}}\underline{\hat{i}}_{\mathrm{in}} - \mathbf{Y}_{\mathrm{o}}\underline{\hat{u}}_{\mathrm{o}} + \mathbf{G}_{\mathrm{co}}\underline{\hat{d}}. \tag{2.85}$$

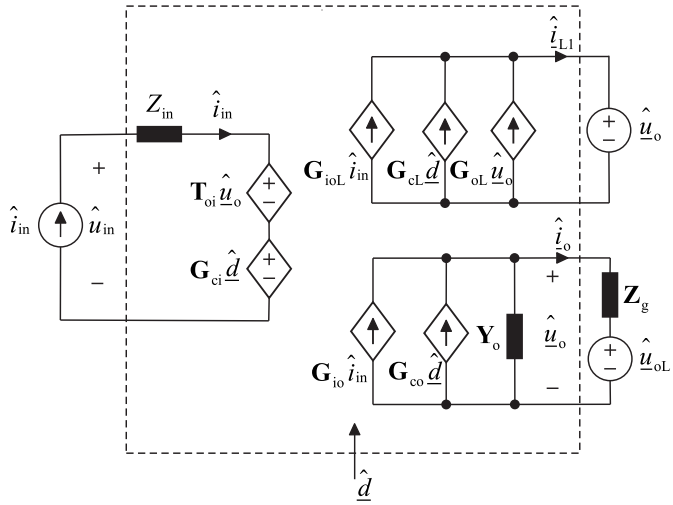

Fig. 2.5: Load-affected model of a grid-connected inverter at open loop.

Moreover, the voltage at the PCC, i.e., $\underline{\hat{u}}_{\mathrm{o}}$ can be given by

$$\underline{\hat{u}}_{\mathrm{o}} = \mathbf{Z}_{\mathrm{g}}\underline{\hat{i}}_{\mathrm{o}} + \underline{\hat{u}}_{\mathrm{oL}}, \tag{2.86}$$

where the grid impedance matrix can be presented by

$$\mathbf{Z}_{\mathrm{g}} = \begin{bmatrix} Z_{\mathrm{g\text{-}d}} & Z_{\mathrm{g\text{-}qd}} \\ Z_{\mathrm{g\text{-}dq}} & Z_{\mathrm{g\text{-}q}} \end{bmatrix}. \tag{2.87}$$

By substituting (2.86) into (2.85) yields

$$\underline{\hat{i}}_{\mathrm{o}} = \mathbf{G}_{\mathrm{io}}\underline{\hat{i}}_{\mathrm{in}} - \mathbf{Y}_{\mathrm{o}}\left(\mathbf{Z}_{\mathrm{g}}\underline{\hat{i}}_{\mathrm{o}} + \underline{\hat{u}}_{\mathrm{oL}}\right) + \mathbf{G}_{\mathrm{co}}\underline{\hat{d}}, \tag{2.88}$$

which can be rearranged as follows

$$\underline{\hat{i}}_{\mathrm{o}} = (\mathbf{I} + \mathbf{Y}_{\mathrm{o}}\mathbf{Z}_{\mathrm{g}})^{-1}\mathbf{G}_{\mathrm{io}}\underline{\hat{i}}_{\mathrm{in}} - (\mathbf{I} + \mathbf{Y}_{\mathrm{o}}\mathbf{Z}_{\mathrm{g}})^{-1}\mathbf{Y}_{\mathrm{o}}\underline{\hat{u}}_{\mathrm{oL}} + (\mathbf{I} + \mathbf{Y}_{\mathrm{o}}\mathbf{Z}_{\mathrm{g}})^{-1}\mathbf{G}_{\mathrm{co}}\underline{\hat{d}}, \tag{2.89}$$

where $\mathbf{I}$ is the identity matrix with suitable dimensions. From (2.89) the load-affected transfer functions for the output current can be presented by

$$\mathbf{G}_{\mathrm{io}}^{\mathrm{L}} = (\mathbf{I} + \mathbf{Y}_{\mathrm{o}}\mathbf{Z}_{\mathrm{g}})^{-1}\mathbf{G}_{\mathrm{io}}, \tag{2.90}$$

$$\mathbf{Y}_{\mathrm{o}}^{\mathrm{L}} = (\mathbf{I} + \mathbf{Y}_{\mathrm{o}}\mathbf{Z}_{\mathrm{g}})^{-1}\mathbf{Y}_{\mathrm{o}}, \tag{2.91}$$

$$\mathbf{G}_{\mathrm{co}}^{\mathrm{L}} = (\mathbf{I} + \mathbf{Y}_{\mathrm{o}}\mathbf{Z}_{\mathrm{g}})^{-1}\mathbf{G}_{\mathrm{co}}, \tag{2.92}$$

where the superscript 'L' denotes the load-affected transfer functions.

The effect of the grid impedance on the inverter-side inductor current $\hat{\underline{i}}_{\mathrm{L1}}$ can be derived as follows. By substituting (2.89) into (2.86) and solving for $\hat{\underline{u}}_{\mathrm{o}}$ yields

$$\begin{aligned}\hat{\underline{u}}_{\mathrm{o}} = \mathbf{Z}_{\mathrm{G}}[&(\mathbf{I} + \mathbf{Y}_{\mathrm{o}}\mathbf{Z}_{\mathrm{g}})^{-1}\mathbf{G}_{\mathrm{io}}\hat{\underline{i}}_{\mathrm{in}} - (\mathbf{I} + \mathbf{Y}_{\mathrm{o}}\mathbf{Z}_{\mathrm{g}})^{-1}\mathbf{Y}_{\mathrm{o}}\hat{\underline{u}}_{\mathrm{oL}} && (2.93)\\ &+(\mathbf{I} + \mathbf{Y}_{\mathrm{o}}\mathbf{Z}_{\mathrm{g}})^{-1}\mathbf{G}_{\mathrm{co}}\hat{\underline{d}}] + \hat{\underline{u}}_{\mathrm{oL}}. && (2.94)\end{aligned}$$

Furthermore, the open-loop representation for inverter-side inductor current can be given by

$$\hat{\underline{i}}_{\mathrm{L1}} = \mathbf{G}_{\mathrm{ioL}}\hat{\underline{i}}_{\mathrm{in}} + \mathbf{G}_{\mathrm{oL}}\hat{\underline{u}}_{\mathrm{o}} + \mathbf{G}_{\mathrm{cL}}\hat{\underline{d}}. \tag{2.95}$$

By substituting $\hat{\underline{u}}_{\mathrm{o}}$ in (2.95) by (2.93) and solving for $\hat{\underline{i}}_{\mathrm{L1}}$ yields the load-affected inverter-side inductor current, which can be now presented by

$$\begin{aligned}\hat{\underline{i}}_{\mathrm{L1}} =&[\mathbf{G}_{\mathrm{ioL}} + \mathbf{G}_{\mathrm{oL}}\mathbf{Z}_{\mathrm{g}}(\mathbf{I} + \mathbf{Y}_{\mathrm{o}}\mathbf{Z}_{\mathrm{g}})^{-1}\mathbf{G}_{\mathrm{io}}]\hat{\underline{i}}_{\mathrm{in}}\\ &+[\mathbf{G}_{\mathrm{oL}} - \mathbf{G}_{\mathrm{oL}}\mathbf{Z}_{\mathrm{g}}(\mathbf{I} + \mathbf{Y}_{\mathrm{o}}\mathbf{Z}_{\mathrm{g}})^{-1}\mathbf{Y}_{\mathrm{o}}]\hat{\underline{u}}_{\mathrm{oL}}\\ &+[\mathbf{G}_{\mathrm{cL}} + \mathbf{G}_{\mathrm{oL}}\mathbf{Z}_{\mathrm{g}}(\mathbf{I} + \mathbf{Y}_{\mathrm{o}}\mathbf{Z}_{\mathrm{g}})^{-1}\mathbf{G}_{\mathrm{co}}]\hat{\underline{d}}.\end{aligned} \tag{2.96}$$

Accordingly, the load-affected transfer functions for the inverter-side inductor current can be given by

$$\mathbf{G}_{\mathrm{ioL}}^{\mathrm{L}} = \mathbf{G}_{\mathrm{ioL}} + \mathbf{G}_{\mathrm{oL}}\mathbf{Z}_{\mathrm{g}}(\mathbf{I} + \mathbf{Y}_{\mathrm{o}}\mathbf{Z}_{\mathrm{g}})^{-1}\mathbf{G}_{\mathrm{io}}, \tag{2.97}$$

$$\mathbf{G}_{\mathrm{oL}}^{\mathrm{L}} = \mathbf{G}_{\mathrm{oL}} - \mathbf{G}_{\mathrm{oL}}\mathbf{Z}_{\mathrm{g}}(\mathbf{I} + \mathbf{Y}_{\mathrm{o}}\mathbf{Z}_{\mathrm{g}})^{-1}\mathbf{Y}_{\mathrm{o}}, \tag{2.98}$$

$$\mathbf{G}_{\mathrm{cL}}^{\mathrm{L}} = \mathbf{G}_{\mathrm{cL}} + \mathbf{G}_{\mathrm{oL}}\mathbf{Z}_{\mathrm{g}}(\mathbf{I} + \mathbf{Y}_{\mathrm{o}}\mathbf{Z}_{\mathrm{g}})^{-1}\mathbf{G}_{\mathrm{co}}. \tag{2.99}$$

3 ACTIVE-DAMPING-AFFECTED CLOSED-LOOP MODEL

This chapter discusses on the inherent properties of active damping as well as presents the closed-loop model of a grid-connected converter with both single and multi-current-feedback active-damping schemes. First, the closed-loop model in case of the multi-current-feedback scheme is derived, which is followed by the single-current-feedback counterpart. Furthermore, control system design and stability evaluation are presented in case of both multi and single-current schemes, which are supported by Bode-plot and root-locus analyses. The operating point and the component values used in the following analysis are given in Table 3.1. The controller parameters can be found in Appendix B. For clarification, the power stage as well as the control system configuration are illustrated in Fig. 3.1.

Table 3.1: Operating point and component values.

Parameter	Value	Parameter	Value
U_{in}	415 V	C_{in}	1.9 mF
I_{in}	6.6 A	L_1	2.5 mH
$U_{\mathrm{grid,rms}}$	120 V	r_{L1}	65 mΩ
$\omega_{\mathrm{grid}}, \omega_{\mathrm{s}}$	2π60 rad/s	C_{f}	10 μF
f_{s}	6–8–20 kHz	r_{Cf}	10 mΩ
f_{res}	2.29 kHz	L_2	0.6 mH
$f_{\mathrm{s}}/f_{\mathrm{res}}$	2.6–3.5–8.7	r_{L2}	22 mΩ
r_{sw}	10 mΩ		

3.1 Active damping considerations

This section briefly discusses the relevant factors in the design of active damping. Accordingly, the derivation of the active-damping-feedback coefficient is performed, and its physical meaning regarding the system dynamics is elaborated. Moreover, as the system delay imposes significant design constraints for active damping, the effect of delay on frequency-domain analysis is discussed.

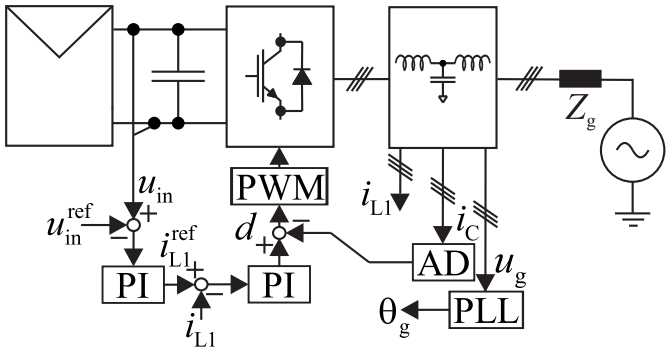

Fig. 3.1: Depiction of the power stage and control system configuration.

3.1.1 Active damping feedback coefficient

The active damping affects the open-loop dynamics via the capacitor-current feedback by changing the linearized equations describing the state-space of the converter (cf. Eqs. (2.44)-(2.53)). This effect can be realized by replacing the perturbed duty ratio in the open-loop state space by the active-damping-affected form. Accordingly, the selection of the active damping gain as $R_\mathrm{d}/U_\mathrm{in}$ can be well justified. By considering the effect of active damping feedback on the system state space, its physical meaning can be also clearly understood.

Active damping affects directly the perturbed duty ratio as (by neglecting the delay for simplicity)

$$\underline{\hat{d}} = \underline{\hat{c}} - \mathbf{G}_\mathrm{AD}\underline{\hat{i}}_\mathrm{Cf}, \tag{3.1}$$

where $\underline{\hat{c}}$ is the control-signal vector (i.e., the output of the current controller) and $\mathbf{G}_\mathrm{AD}$ is the active damping transfer matrix. Different duty-ratio-affecting active damping methods can be implemented by modifying the corresponding feedback matrix or the feedback signal. However, only the capacitor-current-feedback method is discussed for simplicity. Accordingly, the linearized state-space equations, directly affected by the duty ratio perturbation, are the d and q-component of the inverter-side inductor current as

$$\begin{aligned}\frac{\mathrm{d}\hat{i}_\mathrm{L1d}}{\mathrm{d}t} = \frac{1}{L_1}\Big[&-(r_\mathrm{eq}+r_\mathrm{C})\,\hat{i}_\mathrm{L1d} + \omega_\mathrm{s}L_1\hat{i}_\mathrm{L1q} + r_\mathrm{C}\hat{i}_\mathrm{L2d} \\ &-\hat{u}_\mathrm{Cfd} + D_\mathrm{d}\hat{u}_\mathrm{Cin} + U_\mathrm{in}\hat{d}_\mathrm{d}\Big],\end{aligned} \tag{3.2}$$

$$\frac{\mathrm{d}\hat{i}_{\mathrm{L1q}}}{\mathrm{d}t} = \frac{1}{L_1}\Big[-(r_{\mathrm{eq}} + r_{\mathrm{C}})\,\hat{i}_{\mathrm{L1q}} - \omega_{\mathrm{s}} L_1 \hat{i}_{\mathrm{L1d}} + r_{\mathrm{C}}\hat{i}_{\mathrm{L2q}} \\ -\hat{u}_{\mathrm{Cfq}} + D_{\mathrm{q}}\hat{u}_{\mathrm{Cin}} + U_{\mathrm{in}}\hat{d}_{\mathrm{q}}\Big], \tag{3.3}$$

where $r_{\mathrm{eq}} = r_{\mathrm{L1}} + r_{\mathrm{switch}}$.

In a passively damped system, the filter capacitor is connected in series with an additional damping resistor. Thus, considering Eqs. (3.2) and (3.3), the parameter r_{C} would be relatively high. Resonance damping is, therefore, achieved when the virtual resistor R_{d} is implemented in series with the filter capacitor, i.e. $r_{\mathrm{C,new}} = r_{\mathrm{C,old}} + R_{\mathrm{d}}$, by modifying the duty ratios $\hat{d}_{\mathrm{d}}$ and $\hat{d}_{\mathrm{q}}$. This is obtained when the d and q-component duty ratios are modified as given in (3.4) and (3.5), respectively.

$$\hat{d}_{\mathrm{d}} = \hat{c}_{\mathrm{d}} - \frac{R_{\mathrm{d}}}{U_{\mathrm{in}}}\hat{i}_{\mathrm{Cfd}} = \hat{c}_{\mathrm{d}} - \frac{R_{\mathrm{d}}}{U_{\mathrm{in}}}(\,\hat{i}_{\mathrm{L1d}} - \hat{i}_{\mathrm{L2d}}) \tag{3.4}$$

$$\hat{d}_{\mathrm{q}} = \hat{c}_{\mathrm{q}} - \frac{R_{\mathrm{d}}}{U_{\mathrm{in}}}\hat{i}_{\mathrm{Cfq}} = \hat{c}_{\mathrm{q}} - \frac{R_{\mathrm{d}}}{U_{\mathrm{in}}}(\,\hat{i}_{\mathrm{L1q}} - \hat{i}_{\mathrm{L2q}}) \tag{3.5}$$

In Eqs. (3.4) and (3.5), R_{d} is the virtual resistor value and U_{in} is the steady-state input voltage. The active damping gain matrix shown, e.g., in (3.25) can be formed according to (3.4) and (3.5) yielding

$$\mathbf{G}_{\mathrm{AD}} = \begin{bmatrix} \frac{R_{\mathrm{d}}}{U_{\mathrm{in}}} & 0 \\ 0 & \frac{R_{\mathrm{d}}}{U_{\mathrm{in}}} \end{bmatrix}. \tag{3.6}$$

The effectiveness of the active damping can be adjusted by changing the value of the virtual damping resistor R_{d}. It is worth noting that the use of virtual resistor incorporates design constraints concerning the stability of the inverter. As discussed in [29, 80], the effect of computation delay changes the behavior of the active damping feedback and may introduce open-loop RHP poles into the control system. Accordingly, limitations are imposed for the selection of the active damping gain. The effect of the delay can be minimized by using modified feedback methods as discussed, e.g., in [33, 80–82]. The active damping implementations, which mitigates the effect of the delay, are analyzed further by means of the root locus analysis presented in Section 3.5.

3.1.2 Properties of delay

In digital control systems, the system variables, i.e., voltages or currents, are sampled by means of analog-to-digital converters (ADC), and the samples are processed with various control algorithms. Accordingly, different types of delays affect the signal processing and may effectively increase the risk of instability. Delay in the signal path originates, e.g., from computation, sample-and-hold, and PWM reference update actions.

Generally, a delay of one switching cycle is caused by the PWM transport delay mechanism, i.e., a PWM reference calculated at a time instant $t = t_0$ is loaded after one switching period as $t = t_0 + T_\mathrm{s}$ in order to avoid intermediate transitions of the PWM reference value [83]. Moreover, the PWM is usually implemented either in single-update or double-update mode, which affects the overall delay. By using the single-update mode, the output of the PWM is updated either when the carrier wave (i.e., a digital counter) is at its maximum or at zero, that is, once per switching cycle. Therefore, the single-update PWM induces approximately half of the modulation period as delay in the system dynamics, which is considered in the following analysis. In the double-update mode, the output of the PWM is updated when the carrier signal is zero and again at its maximum. Accordingly, the output is updated twice per modulation period, which effectively decreases the delay compared to the single-update mode.

The delay causes time-shift between the system input and output as $y(t) = u(t - T_\mathrm{d})$, which can be given in the frequency-domain as $Y(s) = U(s)e^{-sT_\mathrm{d}}$, where T_d is the finite time-delay. However, in order to incorporate the delay into the frequency-domain analysis, a rational transfer function is required as $G(s) = N(s)/D(s)$, where the order of $D(s) \geq N(s)$. Therefore, Padé-approximations are often used to approximate the exponential function of the delay. These rational approximations do not represent exactly the ideal delay and they may be inaccurate especially at high frequencies. However, the delay needs to be approximated only within a finite frequency range, and different order of (i.e., different accuracies) approximations can be utilized depending on the application.

The 1st, 2nd and 3rd-order Padé-approximations can be given in the frequency-domain as

$$
\begin{aligned}
e_{\mathrm{1st}}^{-sT_\mathrm{d}} &\approx \frac{-\frac{1}{2}T_\mathrm{d}s + 1}{\frac{1}{2}T_\mathrm{d}s + 1}, \\
e_{\mathrm{2nd}}^{-sT_\mathrm{d}} &\approx \frac{\frac{1}{12}(T_\mathrm{d}s)^2 - \frac{1}{2}T_\mathrm{d}s + 1}{\frac{1}{12}(T_\mathrm{d}s)^2 + \frac{1}{2}T_\mathrm{d}s + 1}, \\
e_{\mathrm{3rd}}^{-sT_\mathrm{d}} &\approx \frac{-\frac{1}{120}(T_\mathrm{d}s)^3 + \frac{1}{10}(T_\mathrm{d}s)^2 - \frac{1}{2}T_\mathrm{d}s + 1}{\frac{1}{120}(T_\mathrm{d}s)^3 + \frac{1}{10}(T_\mathrm{d}s)^2 + \frac{1}{2}T_\mathrm{d}s + 1}.
\end{aligned}
\tag{3.7}
$$

Fig. 3.2 shows the frequency-domain behavior of different delay approximations and, for comparison, the ideal delay ($T_\mathrm{d} = 1.5T_\mathrm{s}$). The lowest sampling frequency used in the analysis is 6 kHz and, therefore, $T_\mathrm{s} = 1/6$ ms, where T_s denotes the sampling interval. These represent the actual parameters used in the analysis.

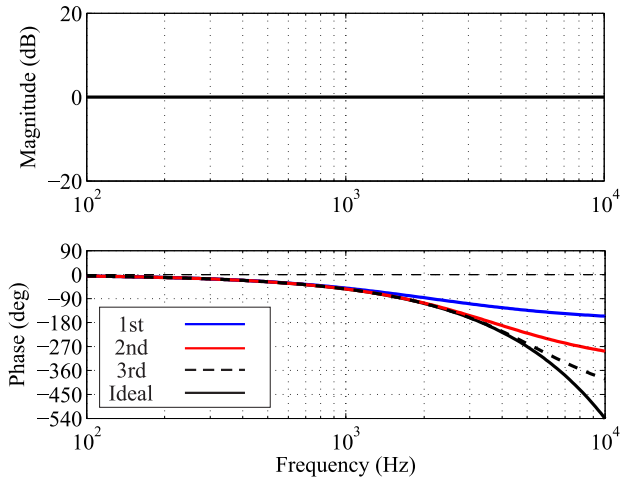

Fig. 3.2: Depiction of an ideal delay with the 1st, 2nd and 3rd-order Padé approximations.

The magnitude of the signal remains unaffected regardless of the approximation method. However, major phase differences may occur with low order approximations. Regarding the small-signal modeling, the obtained model is accurate up to half the switching frequency and, therefore, the approximation of the delay should guarantee accuracy for up to aforementioned frequency. According to Fig. 3.2, the first-order approximation may not be sufficient for the delay as large deviations occur even around 2 kHz. However, the second-order approximation is accurate up to half the minimum switching frequency of 6 kHz, which can be considered appropriate in this case.

As discussed earlier, the active damping, along with the control system, is affected by the system delay. Considering active damping, the condition, where the resonant frequency of the LCL-filter (f_res) equals one-sixth of the sampling frequency (f_s) has been noticed to be critical for stability of a grid-connected converter [28, 29, 31, 34, 36, 37, 84]. Similar critical frequency is found also for converters with L-filters as the phenomenon is related to the delay and not necessarily to the filter topology [76].

The reason for aforementioned delay-dependent behavior may not be clear and, therefore, it is explained here further. Considering Figs. 3.3 and 3.7, the block-diagram can

be slightly manipulated, and the active damping feedback can be given by

$$\mathbf{L}_{\mathrm{AD}} = \mathbf{G}_{\mathrm{AD}}\mathbf{G}_{\mathrm{del}} = \begin{bmatrix} \frac{R_{\mathrm{d}}}{U_{\mathrm{in}}} & 0 \\ 0 & \frac{R_{\mathrm{d}}}{U_{\mathrm{in}}} \end{bmatrix} \begin{bmatrix} e^{-kT_{\mathrm{s}}s} & 0 \\ 0 & e^{-kT_{\mathrm{s}}s} \end{bmatrix}, \tag{3.8}$$

where $e^{-kT_{\mathrm{s}}s}$ is the ideal system delay and $k = 1.5$ in order to represent a realistic system delay [85]. The d and q-components can be expressed as $G_{\mathrm{AD-(d,q)}} = R_{\mathrm{d}}/U_{\mathrm{in}} \cdot e^{-kT_{\mathrm{s}}s}$. By substituting $s = j\omega$, the frequency-dependent behavior of the feedback term can be given according to Euler's formula by

$$G_{\mathrm{AD-(d,q)}} = R_{\mathrm{d}}/U_{\mathrm{in}}[\cos(kT_{\mathrm{s}}\omega) - j\sin(kT_{\mathrm{s}}\omega)] \tag{3.9}$$

The real part in (3.9) damps the LCL-filter resonance and the imaginary part can be considered to induce either phase-lag or phase-boost depending on its sign. According to the active-damping-feedback derivation shown in Section 3.1.1, the capacitor current has to be subtracted from the duty ratio in order to obtain a correct damping term in the linearized converter currents in (3.2) and (3.3). However, the real part of the active damping feedback (i.e., the cosine-term) changes its sign depending on the resonant frequency. This sign change of the feedback term can be evaluated by analyzing the zero-crossing frequency of the cosine-term. Accordingly, the corresponding critical frequency for the real part in (3.9) can be derived as

$$\begin{aligned} &\mathrm{Re}\left\{ G_{\mathrm{AD-(d,q)}} \right\} = 0 \\ &\rightarrow \cos(kT_{\mathrm{s}}\omega) = 0 \\ &\rightarrow kT_{\mathrm{s}}\omega = n\tfrac{\pi}{2}, \quad \omega = 2\pi f, \quad n \in \mathbb{Z} \\ &\rightarrow kT_{\mathrm{s}}2\pi f = n\tfrac{\pi}{2} \\ &\rightarrow f = n\tfrac{1}{2}\tfrac{1}{kT_{\mathrm{s}}2} = n\tfrac{1}{4kT_{\mathrm{s}}} = n\tfrac{f_{\mathrm{s}}}{6}, |k = 1.5 \ , \end{aligned} \tag{3.10}$$

where $n = 1$ suffices for analysis. Eq. (3.10) indicates that depending on whether the LCL-filter resonant frequency is $f_{\mathrm{res}} < f_{\mathrm{s}}/6$ or $f_{\mathrm{res}} > f_{\mathrm{s}}/6$, the sign of the active damping gain has to be changed accordingly to guarantee stability. This behavior or constraint has been noticed in various publications to be one of the major factors affecting the stable operation of active damping [29, 34, 39].

Similar analysis can be used for the imaginary part of the active damping gain as

$$\begin{aligned}
&\mathrm{Im}\left\{ G_{\mathrm{AD}-(\mathrm{d,q})} \right\} = 0 \\
&\rightarrow \sin(kT_\mathrm{s}\omega) = 0 \\
&\rightarrow kT_\mathrm{s}\omega = n\pi, \quad \omega = 2\pi f, \quad n \in \mathbb{Z} \\
&\rightarrow kT_\mathrm{s}2\pi f = n\pi \\
&\rightarrow f = n\tfrac{1}{kT_\mathrm{s}2} = n\tfrac{f_\mathrm{s}}{3}, |k = 1.5,
\end{aligned} \tag{3.11}$$

which reveals that it changes sign from negative to positive and *vice versa* when $f_\mathrm{res} = f_\mathrm{s}/3$. Correspondingly, the imaginary term induces either phase boost or phase lag to the active damping feedback, which can cause decreased performance of active damping if neglected. It has been observed, e.g., in [29, 80] that recognizing the effect of the imaginary part is important for the robustness of the converter stability if a modified active damping feedback, e.g., with a high-pass filter, is used.

3.2 Open-loop dynamics in case of multi-current-feedback scheme

Fig. 3.3 shows a complete closed-loop diagram of a grid-connected inverter with cascaded control scheme. It is formed by adding the necessary control functions, i.e., controllers, active damping feedback, delays and measurement gains to a system shown in Fig. 2.3. As the DC-link voltage must be controlled, e.g., in PV applications, a cascaded-control scheme is used as a control strategy. The outer loop, i.e., the input-voltage control-loop in Fig. 3.3, provides the d-component-current reference to the inner output-current control-loop. It should be noted that the q-component output-current reference is usually set to zero in order to obtain unity power factor.

Active damping affects directly the duty ratio generation by forming an inner loop inside the output-current control loop. The effect of the active damping can be added into the model by replacing the control signal $\underline{\hat{d}}$ shown in Fig. 3.3 by (3.12), which represents the active-damping-affected duty ratio.

$$\underline{\hat{d}} = \mathbf{G}_\mathrm{del} \left(\underline{\hat{c}} - \mathbf{G}_\mathrm{AD} \overbrace{\left(\underline{\hat{i}}_\mathrm{L1} - \underline{\hat{i}}_\mathrm{L2} \right)}^{\underline{\hat{i}}_\mathrm{c}} \right) \tag{3.12}$$

It is noteworthy that also the PLL affects the duty ratio generation, however, it is omitted from the following derivation in order to simplify the analysis and to present the effect of active damping more explicitly. The effect of the PLL will be considered later during the derivation of output-current-controlled model.

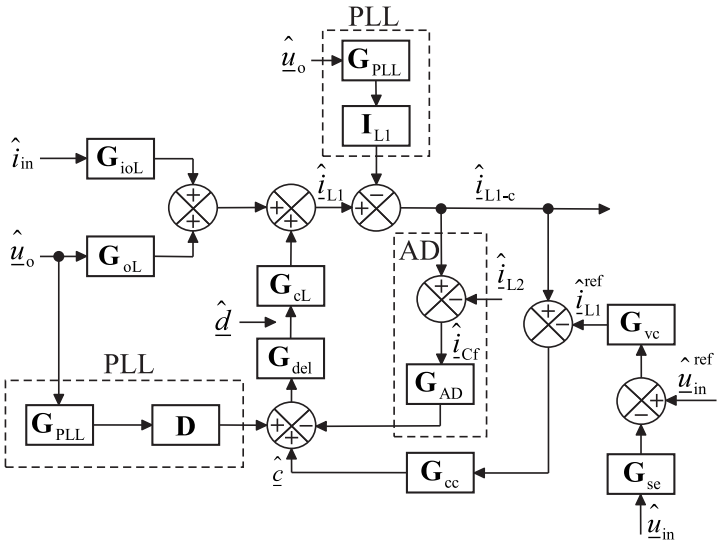

Fig. 3.3: Closed-loop control block diagram of a grid-connected converter with multi-current-feedback active damping.

According to the matrix given in (2.63), Eq. (3.12) can be expressed as a function of input and control variables as in (3.13).

$$\begin{aligned}\hat{\underline{d}} = \; & \mathbf{G}_{\mathrm{del}}\hat{\underline{c}} - \mathbf{G}_{\mathrm{del}}\mathbf{G}_{\mathrm{AD}}\Big(\mathbf{G}_{\mathrm{ioL}}\hat{\underline{i}}_{\mathrm{in}} + \mathbf{G}_{\mathrm{oL}}\hat{\underline{u}}_{\mathrm{o}} + \mathbf{G}_{\mathrm{cL}}\hat{\underline{d}} \\ & -\mathbf{G}_{\mathrm{io}}\hat{\underline{i}}_{\mathrm{in}} - \mathbf{Y}_{\mathrm{o}}\hat{\underline{u}}_{\mathrm{o}} - \mathbf{G}_{\mathrm{co}}\hat{\underline{d}}\Big).\end{aligned} \tag{3.13}$$

Solving (3.13) for $\hat{\underline{d}}$ yields

$$\begin{aligned}\hat{\underline{d}} = \; & \left[\mathbf{I} + \mathbf{G}_{\mathrm{del}}\mathbf{G}_{\mathrm{AD}}\left(\mathbf{G}_{\mathrm{cL}} - \mathbf{G}_{\mathrm{co}}\right)\right]^{-1}\mathbf{G}_{\mathrm{del}}\Big[\hat{\underline{c}} - \mathbf{G}_{\mathrm{AD}}\mathbf{G}_{\mathrm{ioL}}\hat{\underline{i}}_{\mathrm{in}} \\ & -\mathbf{G}_{\mathrm{AD}}\mathbf{G}_{\mathrm{oL}}\hat{\underline{u}}_{\mathrm{o}} + \mathbf{G}_{\mathrm{AD}}\mathbf{G}_{\mathrm{io}}\hat{\underline{i}}_{\mathrm{in}} + \mathbf{G}_{\mathrm{AD}}\mathbf{Y}_{\mathrm{o}}\hat{\underline{u}}_{\mathrm{o}}\Big].\end{aligned} \tag{3.14}$$

By substituting (3.14) into the open-loop dynamics presented in Section 2.3, the active damping-affected transfer functions can be solved. First, the input dynamics can be given by

$$Z_{\text{in}}^{\text{AD}} = Z_{\text{in}} + \mathbf{G}_{\text{ci}}[\mathbf{I} + \mathbf{G}_{\text{del}}\mathbf{G}_{\text{AD}}(\mathbf{G}_{\text{cL}} - \mathbf{G}_{\text{co}})]^{-1} \times \mathbf{G}_{\text{del}}\mathbf{G}_{\text{AD}}[\mathbf{G}_{\text{io}} - \mathbf{G}_{\text{ioL}}], \tag{3.15}$$

$$\mathbf{T}_{\text{oi}}^{\text{AD}} = \mathbf{T}_{\text{oi}} + \mathbf{G}_{\text{ci}}[\mathbf{I} + \mathbf{G}_{\text{del}}\mathbf{G}_{\text{AD}}(\mathbf{G}_{\text{cL}} - \mathbf{G}_{\text{co}})]^{-1} \times \mathbf{G}_{\text{del}}\mathbf{G}_{\text{AD}}[\mathbf{Y}_{\text{o}} - \mathbf{G}_{\text{oL}}], \tag{3.16}$$

$$\mathbf{G}_{\text{ci}}^{\text{AD}} = \mathbf{G}_{\text{ci}}[\mathbf{I} + \mathbf{G}_{\text{del}}\mathbf{G}_{\text{AD}}(\mathbf{G}_{\text{cL}} - \mathbf{G}_{\text{co}})]^{-1}\mathbf{G}_{\text{del}}, \tag{3.17}$$

where $Z_{\text{in}}^{\text{AD}}$, $\mathbf{T}_{\text{oi}}^{\text{AD}}$ and $\mathbf{G}_{\text{ci}}^{\text{AD}}$ are the matrices for input impedance, transmittance and control-to-input-voltage transfer functions, respectively.

Additionally, the input-current-to-inductor-current transfer function, output-voltage-to-inductor-current transfer function and the control-to-inductor-current transfer functions can be given as shown in (3.18)-(3.20), respectively.

$$\mathbf{G}_{\text{ioL}}^{\text{AD}} = \mathbf{G}_{\text{ioL}} + \mathbf{G}_{\text{cL}}[\mathbf{I} + \mathbf{G}_{\text{del}}\mathbf{G}_{\text{AD}}(\mathbf{G}_{\text{cL}} - \mathbf{G}_{\text{co}})]^{-1} \times \mathbf{G}_{\text{del}}\mathbf{G}_{\text{AD}}[\mathbf{G}_{\text{io}} - \mathbf{G}_{\text{ioL}}] \tag{3.18}$$

$$\mathbf{G}_{\text{oL}}^{\text{AD}} = \mathbf{G}_{\text{oL}} + \mathbf{G}_{\text{cL}}[\mathbf{I} + \mathbf{G}_{\text{del}}\mathbf{G}_{\text{AD}}(\mathbf{G}_{\text{cL}} - \mathbf{G}_{\text{co}})]^{-1} \times \mathbf{G}_{\text{del}}\mathbf{G}_{\text{AD}}[\mathbf{Y}_{\text{o}} - \mathbf{G}_{\text{oL}}] \tag{3.19}$$

$$\mathbf{G}_{\text{cL}}^{\text{AD}} = \mathbf{G}_{\text{cL}}[\mathbf{I} + \mathbf{G}_{\text{del}}\mathbf{G}_{\text{AD}}(\mathbf{G}_{\text{cL}} - \mathbf{G}_{\text{co}})]^{-1}\mathbf{G}_{\text{del}} \tag{3.20}$$

Furthermore, the grid-current-related forward transfer function, output admittance and control-to-grid-current transfer function can be given by

$$\mathbf{G}_{\text{io}}^{\text{AD}} = \mathbf{G}_{\text{io}} + \mathbf{G}_{\text{co}}[\mathbf{I} + \mathbf{G}_{\text{del}}\mathbf{G}_{\text{AD}}(\mathbf{G}_{\text{cL}} - \mathbf{G}_{\text{co}})]^{-1} \times \mathbf{G}_{\text{del}}\mathbf{G}_{\text{AD}}[\mathbf{G}_{\text{io}} - \mathbf{G}_{\text{ioL}}], \tag{3.21}$$

$$\mathbf{Y}_{\text{o}}^{\text{AD}} = \mathbf{Y}_{\text{o}} + \mathbf{G}_{\text{co}}[\mathbf{I} + \mathbf{G}_{\text{del}}\mathbf{G}_{\text{AD}}(\mathbf{G}_{\text{cL}} - \mathbf{G}_{\text{co}})]^{-1} \times \mathbf{G}_{\text{del}}\mathbf{G}_{\text{AD}}[\mathbf{Y}_{\text{o}} - \mathbf{G}_{\text{oL}}], \tag{3.22}$$

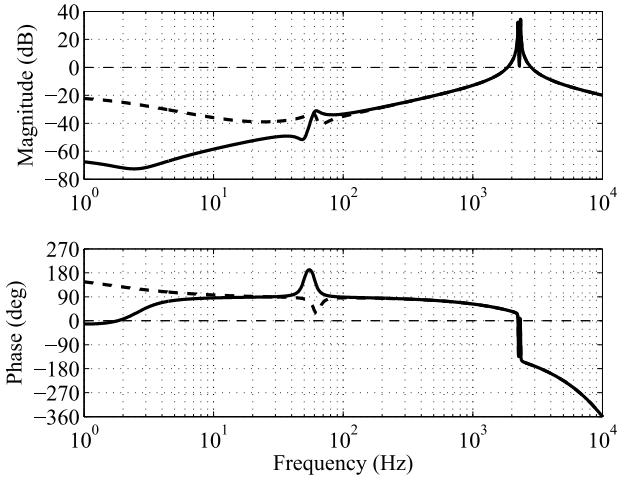

Fig. 3.4: Active damping control loop for the d and q-components (solid and dashed lines).

$$\mathbf{G}_{\mathrm{co}}^{\mathrm{AD}} = \mathbf{G}_{\mathrm{co}}[\mathbf{I} + \mathbf{G}_{\mathrm{del}}(\mathbf{G}_{\mathrm{AD}}\mathbf{G}_{\mathrm{cL}} - \mathbf{G}_{\mathrm{AD}}\mathbf{G}_{\mathrm{co}})]^{-1}\mathbf{G}_{\mathrm{del}}. \tag{3.23}$$

The system delay matrix $\mathbf{G}_{\mathrm{del}}$ and active-damping-feedback-gain matrix $\mathbf{G}_{\mathrm{AD}}$ in Fig. 3.3 are as follows:

$$\mathbf{G}_{\mathrm{del}} = \begin{bmatrix} \frac{1-k_1 s+k_2 s^2}{1+k_1 s+k_2 s^2} & 0 \\ 0 & \frac{1-k_1 s+k_2 s^2}{1+k_1 s+k_2 s^2} \end{bmatrix} \tag{3.24}$$

$$\mathbf{G}_{\mathrm{AD}} = \begin{bmatrix} \frac{R_{\mathrm{d}}}{U_{\mathrm{in}}} & 0 \\ 0 & \frac{R_{\mathrm{d}}}{U_{\mathrm{in}}} \end{bmatrix} \tag{3.25}$$

In Eq. (3.24), a second order Padé approximation is used to represent the ideal delay ($e^{-T_{\mathrm{d}}s}$) with $k_1 = 1/2 \cdot T_{\mathrm{d}}$ and $k_2 = 1/12 \cdot T_{\mathrm{d}}^2$. The system delay is chosen as $T_{\mathrm{d}} = 1.5T_{\mathrm{s}}$ according to [85], where T_{s} is the sampling interval. In practice, the delay consists of PWM loading, analog-to-digital conversion and processing delays.

Considering the multi-current-feedback active damping implementation, the feedback loop processes a signal from the capacitor current, which is a difference between the inverter and grid currents (i.e., two output variables) as $\underline{i}_{\mathrm{C}} = \underline{i}_{\mathrm{L1}} - \underline{i}_{\mathrm{L2}}$. Consequently, the stability of the system may be affected, because the output variables are fed back into the system. Conversely, if the processed variable would be an input variable, a feed-forward loop is formed, which does not impose direct risk for instability. It is important to observe

the fundamental nature of the active damping, which imposes a control-loop-like structure as shown in Fig. 3.3 as well as in (3.15)-(3.23). The active-damping loop can be extracted from aforementioned equations and presented as $\mathbf{L}_{\mathrm{AD}} = \mathbf{G}_{\mathrm{delay}}\mathbf{G}_{\mathrm{AD}}(\mathbf{G}_{\mathrm{cL}} - \mathbf{G}_{\mathrm{co}})$.

In order to further elaborate the issue, active damping control loops for the d and q-components are shown in Fig. 3.4, where the virtual resistor value $R_{\mathrm{d}} = 15\ \Omega$. Evidently, the active-damping loop is effective only in vicinity of the resonant frequency, where the loop regulates the capacitor current to its steady-state value. The open-loop system transfer functions are, therefore, only affected around the corresponding frequency. This is logical since the capacitor acts as an open circuit for lower frequencies, and the current flows mainly through the two filtering inductors, L_1 and L_2. Accordingly, the low-frequency active-damping-loop gain is negligible.

Other important transfer functions in the forthcoming analysis are the active-damping-affected open-loop control-to-inverter-current and output admittance transfer functions $\mathbf{G}_{\mathrm{cL}}^{\mathrm{AD}}$ and $\mathbf{Y}_{\mathrm{o}}^{\mathrm{AD}}$, respectively. Accordingly, the current control loop is designed with $\mathbf{G}_{\mathrm{cL}}^{\mathrm{AD}}$, and the effect of active damping on the shape of the current control loop can be analyzed. Furthermore, the effect of the operation point on the corresponding transfer function should be addressed since it affects the control design.

The open-loop active-damping-affected output admittance can be used to examine the active-damping-induced behavior around the resonant frequency, which is not affected by the output-current control. Furthermore, the effect of the varying operating point at open loop can be analyzed. The source-affected control-to-inductor-current transfer function $\mathbf{G}_{\mathrm{cL}}^{\mathrm{AD}}$ and output admittance $\mathbf{Y}_{\mathrm{o}}^{\mathrm{AD}}$ are presented in Figs. 3.5 and 3.6, respectively.

As can be observed, the shape of the transfer functions at higher frequencies remains practically identical between different operating points, and the operating point affects mainly the low-frequency behavior of the $\mathbf{G}_{\mathrm{cL}}^{\mathrm{AD}}$ due to the operating-point-dependent zero [4]. The low-frequency zero is located either in the RHP, imaginary axis or LHP depending on the operating point (i.e., CCR, MPP or CVR), which causes input-voltage-control-design constraints. These are discussed in detail in Section 3.4. Note that minor gain differences between operating points at higher frequencies, especially in $\mathbf{G}_{\mathrm{cL}}^{\mathrm{AD}}$, are also evident, which should be taken into account in the active damping design.

3.3 Open-loop dynamics in case of single-current-feedback scheme

In single-current-feedback scheme, the capacitor-current measurement is omitted, which reduces the number of sensors required for operation. Instead, either the converter or grid current is measured and the former is used in this thesis. Correspondingly, the measured inverter-side current is used for both active damping and control purposes. Hence, the duty ratio generation (cf. Fig. 3.7) is dependent only on one current instead of two, which changes the active-damping-affected transfer functions shown in previous section.

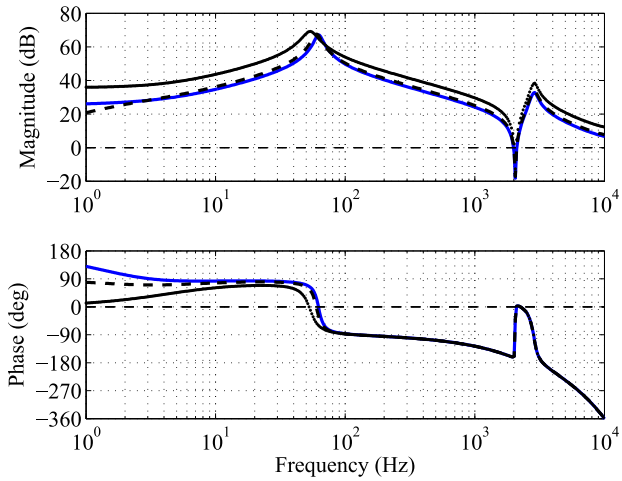

Fig. 3.5: Open-loop control-to-inductor-current transfer functions for multi-current-feedback active damping scheme in CCR (blue line), CVR (black dotted line) and at MPP (black dashed line).

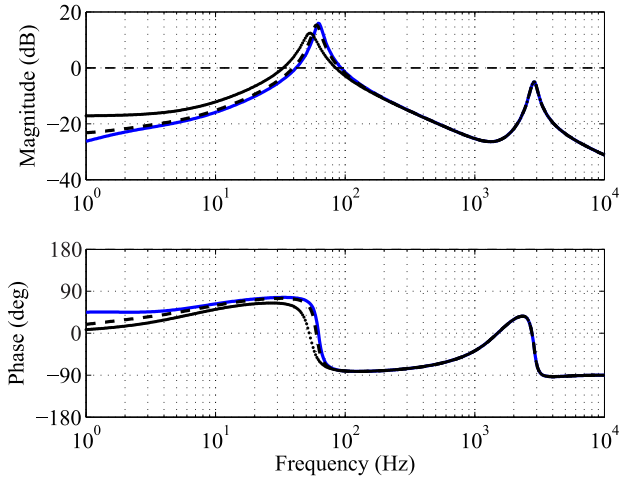

Fig. 3.6: Open-loop output admittance for multi-current-feedback active damping scheme in CCR (blue line), CVR (black dotted line) and at MPP (black dashed line).

Similarly to the capacitor-current-based active damping, the duty ratio can be expressed as

$$\underline{\hat{d}} = \mathbf{G}_{\text{del}} \left(\underline{\hat{c}} - \mathbf{G}_{\text{AD}} \underline{\hat{i}}_{\text{L1}} \right), \tag{3.26}$$

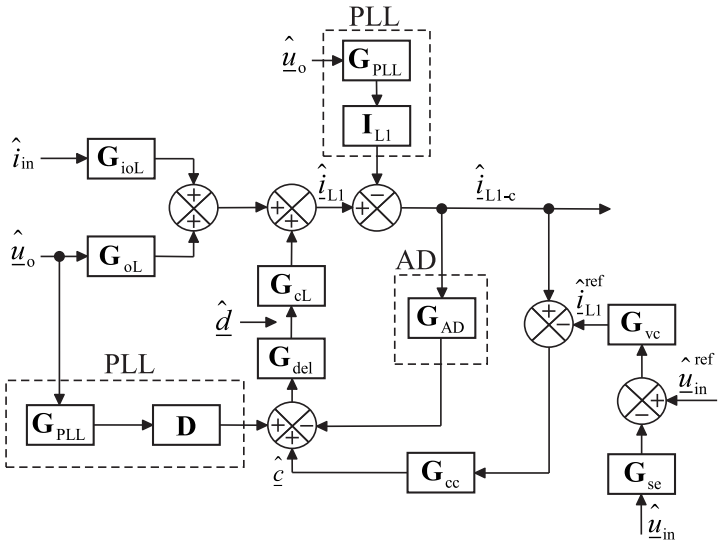

Fig. 3.7: Closed-loop control block diagram of a grid-connected converter with single-current-feedback active damping.

which is substituted into the open-loop dynamics presented in (2.63). Thus, the active-damping-affected duty ratio can be given by following the same procedure as in previous section yielding

$$\underline{\hat{d}} = \left[\mathbf{I} + \mathbf{G}_{\text{del}}\mathbf{G}_{\text{AD}}\mathbf{G}_{\text{cL}}\right]^{-1}\mathbf{G}_{\text{del}}\Big(\underline{\hat{c}} - \mathbf{G}_{\text{AD}}\mathbf{G}_{\text{ioL}}\underline{\hat{i}}_{\text{in}} - \mathbf{G}_{\text{AD}}\mathbf{G}_{\text{oL}}\underline{\hat{u}}_{\text{o}}\Big). \tag{3.27}$$

The transfer function representing the input dynamics can be given as follows.

$$Z_{\text{in}}^{\text{AD}} = Z_{\text{in}} + \mathbf{G}_{\text{ci}}[\mathbf{I} + \mathbf{G}_{\text{del}}\mathbf{G}_{\text{AD}}\mathbf{G}_{\text{cL}}]^{-1}\,\mathbf{G}_{\text{del}}\,[-\mathbf{G}_{\text{AD}}\mathbf{G}_{\text{ioL}}]\,, \tag{3.28}$$

$$\mathbf{T}_{\text{oi}}^{\text{AD}} = \mathbf{T}_{\text{oi}} + \mathbf{G}_{\text{ci}}\,[\mathbf{I} + \mathbf{G}_{\text{del}}\mathbf{G}_{\text{AD}}\mathbf{G}_{\text{cL}}]^{-1}\,\mathbf{G}_{\text{del}}\,[-\mathbf{G}_{\text{AD}}\mathbf{G}_{\text{oL}}]\,, \tag{3.29}$$

$$\mathbf{G}_{\text{ci}}^{\text{AD}} = \mathbf{G}_{\text{ci}}[\mathbf{I} + \mathbf{G}_{\text{del}}\mathbf{G}_{\text{AD}}\mathbf{G}_{\text{cL}}]^{-1}\,\mathbf{G}_{\text{del}}, \tag{3.30}$$

where $Z_{\text{in}}^{\text{AD}}$, $\mathbf{T}_{\text{oi}}^{\text{AD}}$ and $\mathbf{G}_{\text{ci}}^{\text{AD}}$ are the matrices for input impedance, transmittance and control-to-input-voltage transfer functions, respectively.

Additionally, the input-current-to-inductor-current transfer function, output-voltage-to-inductor-current transfer function and the control-to-inductor-current transfer func-

tions can be given as in (3.31)-(3.33), respectively.

$$\mathbf{G}_{\mathrm{ioL}}^{\mathrm{AD}} = \mathbf{G}_{\mathrm{ioL}} + \mathbf{G}_{\mathrm{cL}}[\mathbf{I} + \mathbf{G}_{\mathrm{del}}\mathbf{G}_{\mathrm{AD}}\mathbf{G}_{\mathrm{cL}}]^{-1}\,\mathbf{G}_{\mathrm{del}}\,[-\mathbf{G}_{\mathrm{AD}}\mathbf{G}_{\mathrm{ioL}}] \tag{3.31}$$

$$\mathbf{G}_{\mathrm{oL}}^{\mathrm{AD}} = \mathbf{G}_{\mathrm{oL}} + \mathbf{G}_{\mathrm{cL}}[\mathbf{I} + \mathbf{G}_{\mathrm{del}}\mathbf{G}_{\mathrm{AD}}\mathbf{G}_{\mathrm{cL}}]^{-1}\,\mathbf{G}_{\mathrm{del}}\,[-\mathbf{G}_{\mathrm{AD}}\mathbf{G}_{\mathrm{oL}}] \tag{3.32}$$

$$\mathbf{G}_{\mathrm{cL}}^{\mathrm{AD}} = \mathbf{G}_{\mathrm{cL}}[\mathbf{I} + \mathbf{G}_{\mathrm{del}}\mathbf{G}_{\mathrm{AD}}\mathbf{G}_{\mathrm{cL}}]^{-1}\,\mathbf{G}_{\mathrm{del}} \tag{3.33}$$

Furthermore, the output dynamics can be given by

$$\mathbf{G}_{\mathrm{io}}^{\mathrm{AD}} = \mathbf{G}_{\mathrm{io}} + \mathbf{G}_{\mathrm{co}}[\mathbf{I} + \mathbf{G}_{\mathrm{del}}\mathbf{G}_{\mathrm{AD}}\mathbf{G}_{\mathrm{cL}}]^{-1}\,\mathbf{G}_{\mathrm{del}}\,[-\mathbf{G}_{\mathrm{AD}}\mathbf{G}_{\mathrm{ioL}}]\,, \tag{3.34}$$

$$\mathbf{Y}_{\mathrm{o}}^{\mathrm{AD}} = \mathbf{Y}_{\mathrm{o}} + \mathbf{G}_{\mathrm{co}}[\mathbf{I} + \mathbf{G}_{\mathrm{del}}\mathbf{G}_{\mathrm{AD}}\mathbf{G}_{\mathrm{cL}}]^{-1}\,\mathbf{G}_{\mathrm{del}}\,[-\mathbf{G}_{\mathrm{AD}}\mathbf{G}_{\mathrm{oL}}]\,, \tag{3.35}$$

$$\mathbf{G}_{\mathrm{co}}^{\mathrm{AD}} = \mathbf{G}_{\mathrm{co}}[\mathbf{I} + \mathbf{G}_{\mathrm{del}}\mathbf{G}_{\mathrm{AD}}\mathbf{G}_{\mathrm{cL}}]^{-1}\,\mathbf{G}_{\mathrm{del}}. \tag{3.36}$$

The system delay matrix $\mathbf{G}_{\mathrm{del}}$ and active damping feedback gain matrix $\mathbf{G}_{\mathrm{AD}}$ are as given in Section 3.2 (cf. Eqs. 3.24 and 3.25).

According to the analogy presented to the multi-current-feedback active damping, a feedback loop is formed by the single-current-feedback active damping as it feds back the system output variable, which in this case is the inverter-side inductor current. The active frequency ranges of the active damping loop are visible in Fig. 3.8 and its structure in (3.28)-(3.36). The virtual resistor value was selected similarly to the multi-current-feedback case as $R_{\mathrm{d}} = 15\ \Omega$. In case of the single-current-feedback scheme, the active-damping loop gain can be given as $\mathbf{L}_{\mathrm{AD}} = \mathbf{G}_{\mathrm{delay}}\mathbf{G}_{\mathrm{AD}}\mathbf{G}_{\mathrm{cL}}$. Clearly, the loop gain lacks the term $\mathbf{G}_{\mathrm{co}}$ present in the multi-current-feedback counterpart, which naturally affects the shape of the loop gain as shown in Fig. 3.8 for the d and q-components. It is important to notice that the control gain is also active at the lower frequencies as well as in vicinity of the filter resonant frequency. Consequently, the inverter-side inductor acts as a short circuit at lower frequencies allowing the current to flow freely. This, in turn, translates to substantial current signal in the active damping loop, and the active-damping-affected transfer functions are modified for a wider frequency range than in case of the multi-current-feedback scheme.

Similarly as in the previous section, active-damping-affected control-to-inverter-current and output admittance transfer functions are shown here due to their importance in the analysis later in this thesis. Figs. 3.9 and 3.10 show frequency responses of the

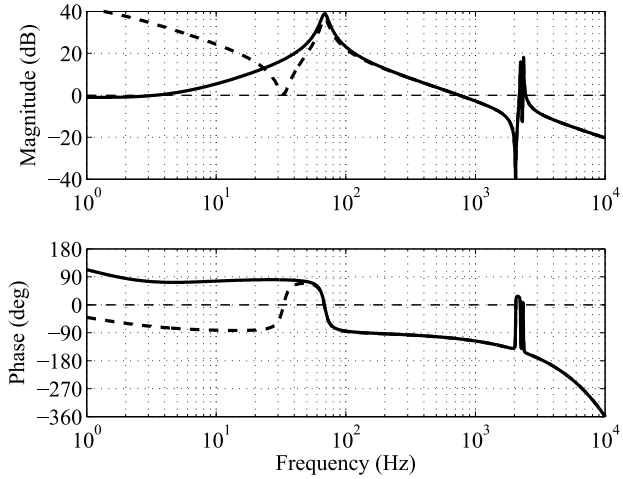

Fig. 3.8: Active damping control loop for the d and q-components (solid and dashed lines).

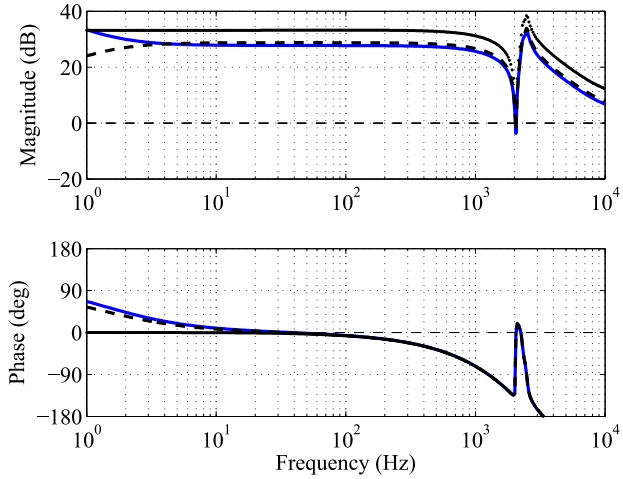

Fig. 3.9: Open-loop control-to-output transfer functions for single-current-feedback active damping scheme in CCR (blue line), CVR (black dotted line) and at MPP (black dashed line).

corresponding transfer functions, respectively. Comparing Figs. 3.9 and 3.10 to Figs. 3.5 and 3.6, it can be observed that the frequency responses are constant within the active-damping loop gain. This behavior is caused by the direct control-loop-like structure of active damping, which induces a constant magnitude in the control-to-inductor-current transfer function ($\hat{i}_{\mathrm{L1d}}/\hat{d}_{\mathrm{d}} \approx I_{\mathrm{L1d}}/D_{\mathrm{d}}$) within its bandwidth. Moreover, the low-frequency behavior of $\mathbf{G}_{\mathrm{cL}}^{\mathrm{AD}}$ exhibits similar phase shifting due to the operating-point-dependent zero as was observed with multi-current-feedback scheme, although, its effect

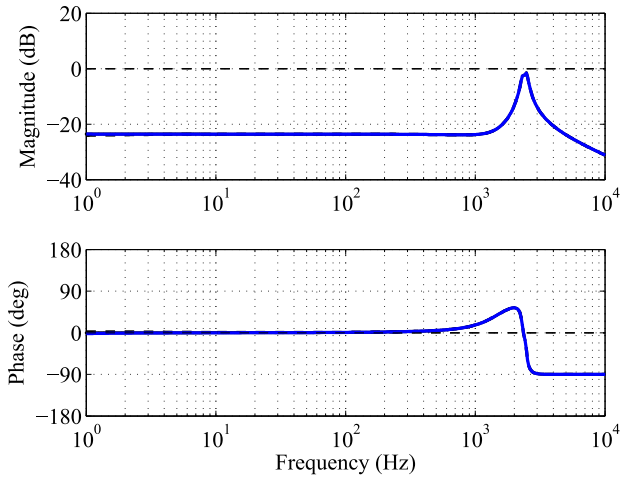

Fig. 3.10: Open-loop output admittance for single-current-feedback active damping scheme in CCR (blue line), CVR (black dotted line) and at MPP (black dashed line).

is insignificant. The open-loop output admittance, on the other hand, does not change along the changes in the operating point. However, significantly lower magnitude of the admittance (or higher impedance) can be observed for single-current-feedback scheme, which eventually affects the closed-loop characteristics. These observations are analyzed more in detail in Section 4.2.

3.4 Closed-loop dynamics

Fig. 3.11 presents the active-damping-affected closed-loop block diagram of output-current and input-voltage dynamics of a grid-connected converter. The models of both multi and single-current-feedback active damping schemes, derived in previous sections, act as 'open-loop' systems for the outer control structures, i.e., for the output current control and, subsequently, for the input-voltage control. The control loops are designed according to the obtained active-damping-affected transfer functions in Sections 3.2 and 3.3. The open-loop transfer functions presented hereinafter are active-damping-affected by default and the superscript 'AD' is omitted, where applicable, for simplicity.

3.4.1 Output-current control

In a cascaded control scheme, the inner loop has to be designed first, and it should have high control bandwidth in order to guarantee proper tracking performance. The closed-loop transfer functions of an output-current-controlled inverter can be solved according to Fig. 3.11 by considering the output current reference (obtained from the voltage

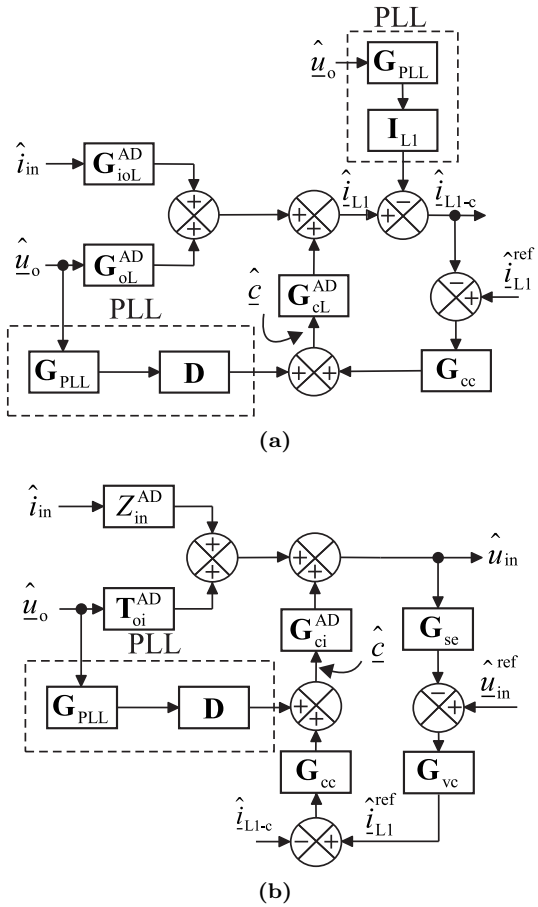

Fig. 3.11: Closed-loop block-diagram in a matrix form of a) output and b) input dynamics of a cascade-controlled VSI-based inverter with active damping.

controller) as a new control variable, thus, neglecting the input-voltage loop. The input voltage dynamics of an output-current-controlled inverter can be given by

$$\hat{\underline{u}}_{in} = Z^{out}_{in}\hat{\underline{i}}_{in} + \mathbf{T}^{out}_{oi}\hat{\underline{u}}_o + \mathbf{G}^{out}_{ci}\hat{\underline{i}}^{ref}_{L1} \tag{3.37}$$

where the superscript 'out' denotes that only the output-current loops are closed. Transfer functions for the output-current-control-affected input impedance, transmittance and control-to-input-voltage in (3.37) can be given by

$$Z^{out}_{in} = Z_{in} - \mathbf{G}_{ci}(\mathbf{I} + \mathbf{L}_{out})^{-1}\mathbf{L}_{out}\mathbf{G}_{cL}{}^{-1}\mathbf{G}_{ioL}, \tag{3.38}$$

$$\mathbf{T}_{\mathrm{oi}}^{\mathrm{out}} = \mathbf{T}_{\mathrm{oi}} - \mathbf{G}_{\mathrm{ci}}(\mathbf{I}+\mathbf{L}_{\mathrm{out}})^{-1}\left[\mathbf{L}_{\mathrm{out}}{\mathbf{G}_{\mathrm{cL}}}^{-1}\mathbf{G}_{\mathrm{oL}} - \mathbf{L}_{\mathrm{out}}{\mathbf{G}_{\mathrm{cL}}}^{-1}\mathbf{I}_{\mathrm{L1}}\mathbf{G}_{\mathrm{PLL}} - \mathbf{D}\mathbf{G}_{\mathrm{PLL}}\right], \tag{3.39}$$

$$\mathbf{G}_{\mathrm{ci}}^{\mathrm{out}} = \mathbf{G}_{\mathrm{ci}}(\mathbf{I}+\mathbf{L}_{\mathrm{out}})^{-1}\mathbf{L}_{\mathrm{out}}{\mathbf{G}_{\mathrm{cL}}}^{-1}, \tag{3.40}$$

where the output-current loop gain $\mathbf{L}_{\mathrm{out}} = \mathbf{G}_{\mathrm{cc}}\mathbf{G}_{\mathrm{cL}}$. Matrices $\mathbf{D}$ and $\mathbf{I}_{\mathrm{L1}}$ are gains for the steady-state duty-ratio and inductor current as shown in (3.41). The matrix $\mathbf{G}_{\mathrm{PLL}}$ contains the PLL transfer functions, which can be expressed as follows [66].

$$\mathbf{D} = \begin{bmatrix} 0 & D_{\mathrm{q}} \\ 0 & D_{\mathrm{d}} \end{bmatrix}, \quad \mathbf{I}_{\mathrm{L1}} = \begin{bmatrix} 0 & I_{\mathrm{L1q}} \\ 0 & I_{\mathrm{L1d}} \end{bmatrix} \tag{3.41}$$

$$\mathbf{G}_{\mathrm{PLL}} = \begin{bmatrix} 0 & 0 \\ 0 & G_{\mathrm{PLL}} \end{bmatrix}, \tag{3.42}$$

$$G_{\mathrm{PLL}} = \frac{1}{U_{\mathrm{od}}}\frac{L_{\mathrm{PLL}}}{1+L_{\mathrm{PLL}}}, \tag{3.43}$$

$$L_{\mathrm{PLL}} = -G_{\mathrm{PI-PLL}}\frac{U_{\mathrm{od}}}{s}, \tag{3.44}$$

$$G_{\mathrm{PI-PLL}} = K_{\mathrm{p}} + \frac{K_{\mathrm{i}}}{s}. \tag{3.45}$$

The matrices of the PI-based current controller $\mathbf{G}_{\mathrm{cc}}$ can be given by

$$\mathbf{G}_{\mathrm{cc}} = \begin{bmatrix} G_{\mathrm{cc-d}} & 0 \\ 0 & G_{\mathrm{cc-q}} \end{bmatrix} = \begin{bmatrix} K_{\mathrm{p}} + \frac{K_{\mathrm{i}}}{s} & 0 \\ 0 & K_{\mathrm{p}} + \frac{K_{\mathrm{i}}}{s} \end{bmatrix} \tag{3.46}$$

Note that decoupling between the d and q-components in the current control is not utilized and, therefore, the corresponding cross-coupling entries in (3.46) are null-elements.

Respectively, the inverter-side inductor current can be given by

$$\hat{\underline{i}}_{\mathrm{L1}} = \mathbf{G}_{\mathrm{ioL}}^{\mathrm{out}} \hat{\underline{i}}_{\mathrm{in}} + \mathbf{G}_{\mathrm{oL}}^{\mathrm{out}} \hat{\underline{u}}_{\mathrm{o}} + \mathbf{G}_{\mathrm{cL}}^{\mathrm{out}} \hat{\underline{u}}_{\mathrm{iL1}}^{\mathrm{ref}} \tag{3.47}$$

where the transfer function matrices are

$$\mathbf{G}_{\mathrm{ioL}}^{\mathrm{out}} = \mathbf{G}_{\mathrm{ioL}} - \mathbf{G}_{\mathrm{cL}}(\mathbf{I} + \mathbf{L}_{\mathrm{out}})^{-1} \mathbf{L}_{\mathrm{out}} {\mathbf{G}_{\mathrm{cL}}}^{-1} \mathbf{G}_{\mathrm{ioL}}, \tag{3.48}$$

$$\begin{aligned} \mathbf{G}_{\mathrm{oL}}^{\mathrm{out}} = \mathbf{G}_{\mathrm{oL}} - \mathbf{G}_{\mathrm{cL}}(\mathbf{I} + \mathbf{L}_{\mathrm{out}})^{-1} \big[& \mathbf{L}_{\mathrm{out}} {\mathbf{G}_{\mathrm{cL}}}^{-1} \mathbf{G}_{\mathrm{oL}} \\ & - \mathbf{L}_{\mathrm{out}} {\mathbf{G}_{\mathrm{cL}}}^{-1} \mathbf{I}_{\mathrm{L1}} \mathbf{G}_{\mathrm{PLL}} - \mathbf{D} \mathbf{G}_{\mathrm{PLL}} \big], \end{aligned} \tag{3.49}$$

$$\mathbf{G}_{\mathrm{cL}}^{\mathrm{out}} = \mathbf{G}_{\mathrm{cL}}(\mathbf{I} + \mathbf{L}_{\mathrm{out}})^{-1} \mathbf{L}_{\mathrm{out}} {\mathbf{G}_{\mathrm{cL}}}^{-1}. \tag{3.50}$$

Furthermore, the grid-current dynamics can be given as follows.

$$\mathbf{G}_{\mathrm{oL}}^{\mathrm{out}} = \mathbf{G}_{\mathrm{oL}} - \mathbf{G}_{\mathrm{co}}(\mathbf{I} + \mathbf{L}_{\mathrm{out}})^{-1} \mathbf{L}_{\mathrm{out}} {\mathbf{G}_{\mathrm{cL}}}^{-1} \mathbf{G}_{\mathrm{ioL}} \tag{3.51}$$

$$\begin{aligned} \mathbf{Y}_{\mathrm{o}}^{\mathrm{out}} = \mathbf{Y}_{\mathrm{o}} - \mathbf{G}_{\mathrm{co}}(\mathbf{I} + \mathbf{L}_{\mathrm{out}})^{-1} \big[& \mathbf{L}_{\mathrm{out}} {\mathbf{G}_{\mathrm{cL}}}^{-1} \mathbf{G}_{\mathrm{oL}} \\ & - \mathbf{L}_{\mathrm{out}} {\mathbf{G}_{\mathrm{cL}}}^{-1} \mathbf{I}_{\mathrm{L1}} \mathbf{G}_{\mathrm{PLL}} - \mathbf{D} \mathbf{G}_{\mathrm{PLL}} \big] \end{aligned} \tag{3.52}$$

$$\mathbf{G}_{\mathrm{co}}^{\mathrm{out}} = \mathbf{G}_{\mathrm{co}}(\mathbf{I} + \mathbf{L}_{\mathrm{out}})^{-1} \mathbf{L}_{\mathrm{out}} {\mathbf{G}_{\mathrm{cL}}}^{-1} \tag{3.53}$$

The output-current control for both d and q-components is designed by shaping the loop gain $\mathbf{L}_{\mathrm{out}}$. Accordingly, the bandwidth of the loop should be relatively high in order to obtain good current tracking response and fast dynamics, which are required in grid-connected applications in order to achieve good power quality. As shown earlier, the loop is designed according to the active-damping-affected control-to-output transfer function $\mathbf{G}_{\mathrm{cL}}$, which is operating-point dependent [4]. Fig. 3.12 presents the loop gain in CCR, CVR and at MPP in case of the multi-current-feedback active damping scheme.

As can be seen, the operating-point-dependent RHP-zero is induced at low frequencies and the corresponding 180 degree phase transition from CCR to CVR and *vice versa* is visible. If only the output-current control is used, the low-frequency RHP-zero limits the current control bandwidth in the CCR, which would yield highly insufficient current tracking performance. Therefore, the high-bandwidth current control is designed in the CVR, which is stabilized by the cascaded control structure in the CCR. The operating-point-dependent zero is, thus, considered only in the input-voltage-control design.

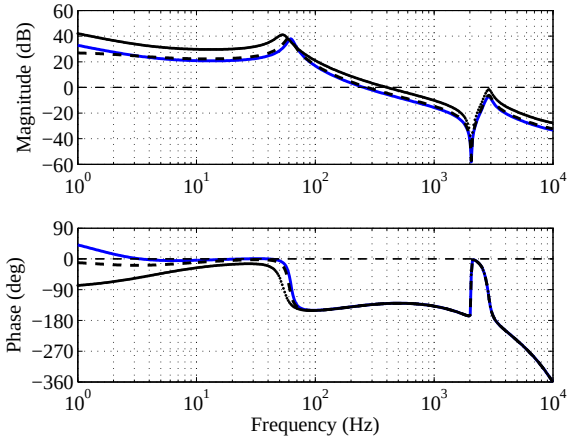

Fig. 3.12: Output current loop gains for multi-current-feedback active damping scheme in CCR (blue line), CVR (black solid line) and at MPP (black dashed line).

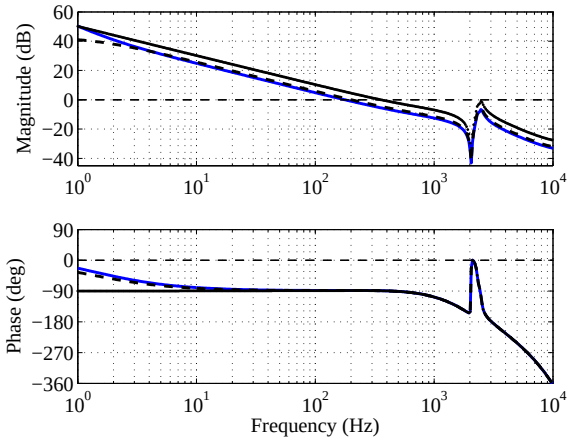

Fig. 3.13: Output current loop gains for single-current-feedback active damping scheme in CCR (blue line), CVR (black solid line) and at MPP (black dashed line).

Regarding the single-current-feedback scheme, Fig. 3.13 shows the current-control loop gain in case of the corresponding active damping scheme. As can be concluded from the observations in Section 3.3, the resonant behavior near 100 Hz is absent. Moreover, the inner active damping loop exhibits constant gain dynamics within its bandwidth and, therefore, the shape of the output-current loop is determined by the current controller. Accordingly, the characteristics of a pure I-controller (integral) are present since the phase stays at -90 degrees with the gain decreasing by 20 dB/decade. Consequently,

higher phase margin can be easily obtained within a wide frequency range, which simplifies the control loop design and reduces risk for oscillation in the current response. In addition, the operating-point-dependent behavior, visible in the multi-current-feedback implementation, does not exist.

3.4.2 Input-voltage control

The input-voltage controller regulates the power extracted from the photovoltaic generator by adjusting the input voltage of the converter (or the output voltage of the PV generator) according to the MPPT algorithms. This is performed indirectly by controlling the d-component of the output current and, therefore, the current flow into the input capacitor. However, the role of the d-component in the controlling of the maximum power might be unclear, which is explained next.

The instantaneous power of the DC-link capacitor can be given as $P_{\mathrm{Cin}} = \mathrm{d}W_{\mathrm{Cin}}/\mathrm{d}t = C_{\mathrm{in}}/2 \cdot \mathrm{d}u_{\mathrm{in}}^2/\mathrm{d}t = P_{\mathrm{in}} - P_{\mathrm{out}}$. As $P_{\mathrm{out}} = \mathrm{Re}\{\mathbf{S}_{\mathrm{out}}\} \approx u_{\mathrm{od}} i_{\mathrm{od}}$ according to the instantaneous power theory, the inverter-side inductor current i_{L1d} (active-power-producing component) indirectly controls the power flow into the input capacitor and, therefore, its reference is determined by the input-voltage controller. Furthermore, since reactive power is not controlled, the q-component of the inverter-side inductor current does not require an outer control loop.

Fig. 3.14 shows the closed-loop block diagram of an input-voltage-controlled grid-connected inverter. Similarly with the output-current-controlled converter in the previous section, the input-voltage reference is considered as the new control variable. Furthermore, the input-voltage control loop generates the d-component of the inverter-side inductor current reference (i.e., $\hat{i}_{\mathrm{L1d}}^{\mathrm{ref}}$). The output-current-control-affected transfer functions, derived in the previous section, form the new 'open-loop' system for the input-voltage control.

The output-current reference can be presented according to Fig. 3.14b by

$$\hat{\underline{i}}_{\mathrm{L1}}^{\mathrm{ref}} = \mathbf{G}_{\mathrm{vc}} \mathbf{G}_{\mathrm{se}} \hat{u}_{\mathrm{in}} - \mathbf{G}_{\mathrm{vc}} \hat{\underline{u}}_{\mathrm{in}}^{\mathrm{ref}}, \tag{3.54}$$

where the vector for input-voltage reference, the voltage sensing gain matrix and voltage controller matrix can be given by

$$\hat{\underline{u}}_{\mathrm{in}}^{\mathrm{ref}} = \begin{bmatrix} \hat{u}_{\mathrm{in}}^{\mathrm{ref}} \\ \hat{i}_{\mathrm{L1q}}^{\mathrm{ref}} \end{bmatrix}, \tag{3.55}$$

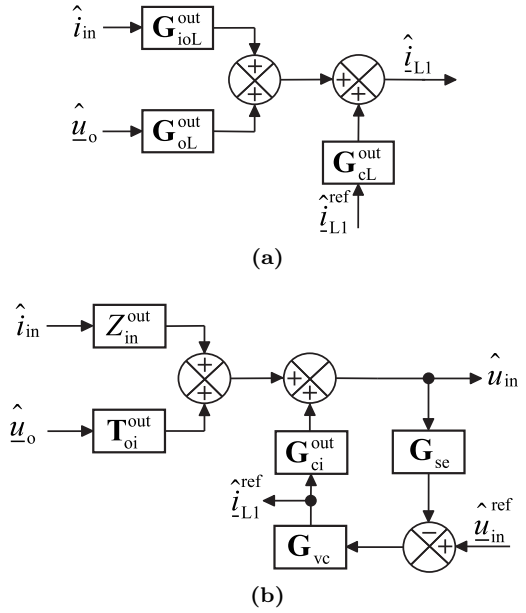

Fig. 3.14: Closed-loop block-diagram in a matrix form of a) input and b) output dynamics of a cascade-controlled VSI-based inverter with active damping.

$$\mathbf{G}_{\text{se}} = \begin{bmatrix} G_{\text{se}} & 0 \\ 0 & 0 \end{bmatrix} = \begin{bmatrix} 1 & 0 \\ 0 & 0 \end{bmatrix}, \tag{3.56}$$

$$\mathbf{G}_{\text{vc}} = \begin{bmatrix} -G_{\text{vc}} & 0 \\ 0 & 1 \end{bmatrix} = \begin{bmatrix} -(K_{\text{p}} + K_{\text{i}}/s) & 0 \\ 0 & 1 \end{bmatrix}, \tag{3.57}$$

respectively. Thus, the input voltage of the output-current-controlled inverter can be expressed according to Fig. 3.14b by

$$\hat{\underline{u}}_{\text{in}} = Z_{\text{in}}^{\text{out}} \hat{\underline{i}}_{\text{in}} + \mathbf{T}_{\text{oi}}^{\text{out}} \hat{\underline{u}}_{\text{o}} + \mathbf{G}_{\text{ci}}^{\text{out}} \hat{\underline{i}}_{\text{L1}}^{\text{ref}}. \tag{3.58}$$

By substituting (3.54) into (3.58), the complete closed-loop input voltage dynamics can be solved as

$$\hat{\underline{u}}_{\text{in}} = (\mathbf{I} + \mathbf{L}_{\text{in}})^{-1} Z_{\text{in}}^{\text{out}} \hat{\underline{i}}_{\text{in}} + (\mathbf{I} + \mathbf{L}_{\text{in}})^{-1} \mathbf{T}_{\text{oi}}^{\text{out}} \hat{\underline{u}}_{\text{o}} - (\mathbf{I} + \mathbf{L}_{\text{in}})^{-1} \mathbf{G}_{\text{ci}}^{\text{out}} \mathbf{G}_{\text{vc}} \hat{\underline{u}}_{\text{in}}^{\text{ref}}, \tag{3.59}$$

where the input-voltage loop gain $\mathbf{L}_{\mathrm{in}} = \mathbf{G}_{\mathrm{ci}}^{\mathrm{out}}\mathbf{G}_{\mathrm{vc}}\mathbf{G}_{\mathrm{se}}$. Hence, the closed-loop transfer functions for input-voltage-controlled converter can be presented by

$$Z_{\mathrm{in}}^{\mathrm{tot}} = (\mathbf{I} + \mathbf{L}_{\mathrm{in}})^{-1} Z_{\mathrm{in}}^{\mathrm{out}}, \tag{3.60}$$

$$\mathbf{T}_{\mathrm{oi}}^{\mathrm{tot}} = (\mathbf{I} + \mathbf{L}_{\mathrm{in}})^{-1} \mathbf{T}_{\mathrm{oi}}^{\mathrm{out}}, \tag{3.61}$$

$$\mathbf{G}_{\mathrm{ci}}^{\mathrm{tot}} = (\mathbf{I} + \mathbf{L}_{\mathrm{in}})^{-1} \mathbf{G}_{\mathrm{ci}}^{\mathrm{out}}\mathbf{G}_{\mathrm{vc}}, \tag{3.62}$$

where the superscript 'tot' denotes the complete closed-loop transfer functions. Respectively, the closed-loop dynamics for the inverter-side inductor current can be given as

$$\hat{\underline{i}}_{\mathrm{L1}} = \mathbf{G}_{\mathrm{ioL}}^{\mathrm{tot}}\hat{\underline{i}}_{\mathrm{in}} + \mathbf{G}_{\mathrm{oL}}^{\mathrm{tot}}\hat{\underline{u}}_{\mathrm{o}} + \mathbf{G}_{\mathrm{cL}}^{\mathrm{tot}}\hat{\underline{u}}_{\mathrm{in}}^{\mathrm{ref}}, \tag{3.63}$$

where

$$\mathbf{G}_{\mathrm{ioL}}^{\mathrm{tot}} = \mathbf{G}_{\mathrm{ioL}}^{\mathrm{out}} - \mathbf{G}_{\mathrm{cL}}^{\mathrm{out}}\mathbf{G}_{\mathrm{vc}}\mathbf{G}_{\mathrm{se}}(\mathbf{I} + \mathbf{L}_{\mathrm{in}})^{-1} Z_{\mathrm{in}}^{\mathrm{out}}, \tag{3.64}$$

$$\mathbf{G}_{\mathrm{oL}}^{\mathrm{tot}} = \mathbf{G}_{\mathrm{oL}}^{\mathrm{out}} - \mathbf{G}_{\mathrm{cL}}^{\mathrm{out}}\mathbf{G}_{\mathrm{vc}}\mathbf{G}_{\mathrm{se}}(\mathbf{I} + \mathbf{L}_{\mathrm{in}})^{-1} \mathbf{T}_{\mathrm{oi}}^{\mathrm{out}}, \tag{3.65}$$

$$\mathbf{G}_{\mathrm{cL}}^{\mathrm{tot}} = -\mathbf{G}_{\mathrm{cL}}^{\mathrm{out}}\left[\mathbf{G}_{\mathrm{vc}}\mathbf{G}_{\mathrm{se}}(\mathbf{I} + \mathbf{L}_{\mathrm{in}})^{-1}\mathbf{G}_{\mathrm{ci}}^{\mathrm{out}}\mathbf{G}_{\mathrm{vc}} - \mathbf{G}_{\mathrm{vc}}\right]. \tag{3.66}$$

Similarly, the closed-loop transfer functions for the grid current are given as follows.

$$\mathbf{G}_{\mathrm{io}}^{\mathrm{tot}} = \mathbf{G}_{\mathrm{io}}^{\mathrm{out}} - \mathbf{G}_{\mathrm{co}}^{\mathrm{out}}\mathbf{G}_{\mathrm{vc}}\mathbf{G}_{\mathrm{se}}(\mathbf{I} + \mathbf{L}_{\mathrm{in}})^{-1} Z_{\mathrm{in}}^{\mathrm{out}} \tag{3.67}$$

$$\mathbf{Y}_{\mathrm{o}}^{\mathrm{tot}} = \mathbf{Y}_{\mathrm{o}}^{\mathrm{out}} - \mathbf{G}_{\mathrm{co}}^{\mathrm{out}}\mathbf{G}_{\mathrm{vc}}\mathbf{G}_{\mathrm{se}}(\mathbf{I} + \mathbf{L}_{\mathrm{in}})^{-1} \mathbf{T}_{\mathrm{oi}}^{\mathrm{out}} \tag{3.68}$$

$$\mathbf{G}_{\mathrm{co}}^{\mathrm{tot}} = -\mathbf{G}_{\mathrm{co}}^{\mathrm{out}}\left[\mathbf{G}_{\mathrm{vc}}\mathbf{G}_{\mathrm{se}}(\mathbf{I} + \mathbf{L}_{\mathrm{in}})^{-1}\mathbf{G}_{\mathrm{ci}}^{\mathrm{out}}\mathbf{G}_{\mathrm{vc}} - \mathbf{G}_{\mathrm{vc}}\right] \tag{3.69}$$

As discussed earlier, the d-component of the open-loop source-affected control-to-inductor-current transfer function $G_{\mathrm{cL-d}}$ incorporates an RHP-zero when the operating point is in the CCR. This induces design constraints for the input-voltage control. Correspondingly, analyzing the output-current-control-affected control-to-input transfer func-

tion $G_{\mathrm{ci-d}}^{\mathrm{out}}$, by neglecting the cross-couplings between the d and q-components, reveals that

$$G_{\mathrm{ci-d}}^{\mathrm{out}} \approx \frac{G_{\mathrm{ci-d}}}{G_{\mathrm{cL-d}}} \frac{L_{\mathrm{out-d}}}{1 + L_{\mathrm{out-d}}}. \tag{3.70}$$

The input-voltage control loop gain can be, therefore, given as

$$\begin{aligned} L_{\mathrm{in}} = G_{\mathrm{se}} G_{\mathrm{vc}} G_{\mathrm{ci-d}}^{\mathrm{out}} &\approx G_{\mathrm{se}} G_{\mathrm{vc}} G_{\mathrm{ci-d}} \frac{1}{G_{\mathrm{cL-d}}} \frac{L_{\mathrm{out-d}}}{1 + L_{\mathrm{out-d}}} \\ &\approx G_{\mathrm{se}} G_{\mathrm{vc}} G_{\mathrm{ci-d}} \frac{1}{G_{\mathrm{cL-d}}}, \end{aligned} \tag{3.71}$$

when $L_{\mathrm{out-d}}/(1 + L_{\mathrm{out-d}}) \approx 1$ inside the output-current-control bandwidth. As can be seen from (3.71), the control-to-inverter-current transfer function $G_{\mathrm{cL-d}}$ is in the denominator of the input-voltage loop gain L_{in}. Therefore, the RHP zero, which appears in the CCR, turns to an RHP pole in the input-voltage control loop. This imposes design constraints for the input-voltage controller and has to be taken into account in the control design (i.e., minimum control bandwidth).

Usually, the maximum angular frequency of the pole is in the range of 1-20 Hz, and can be expressed as [4, 6]

$$\omega_{\mathrm{pole}} = \frac{I_{\mathrm{in}}}{C_{\mathrm{in}} U_{\mathrm{in}}}. \tag{3.72}$$

According to the control engineering principles, the control-loop bandwidth has to exceed the RHP-pole frequency in order to guarantee stability. Another constraint for the input-voltage-controller bandwidth comes from the input voltage ripple at 100 Hz caused by unbalanced grid voltages. The bandwidth of the voltage controller should be designed to provide enough attenuation at the aforementioned frequency in order to avoid polluting the output-current reference (i.e., maximum control bandwidth).

The input-voltage-control-loop gains in case of both multi and single-current-feedback active damping schemes are shown in Figs. 3.15 and 3.16, respectively. As is evident, the effect of the active damping implementation is negligible on the voltage control dynamics as it is active at higher frequencies. In the CVR, the photovoltaic generator resembles an ideal voltage source, unaffected by the changing input current, thus the input voltage control has very slow dynamics. Conversely, as the operating point shifts to the MPP and CCR, the ideal current-source-like characteristics appear and higher control bandwidth is obtained similarly for both operating points.

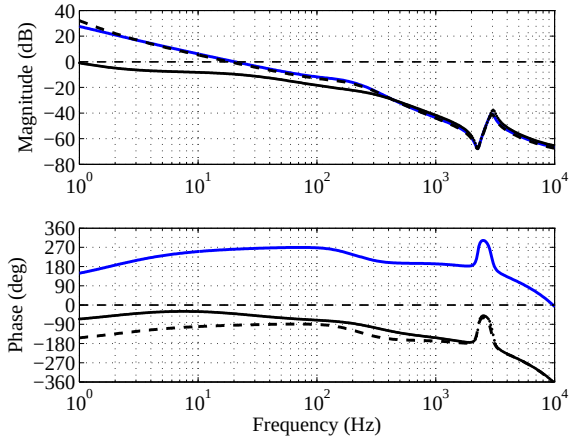

Fig. 3.15: Input voltage loop gains for multi-current-feedback active damping scheme in CCR (blue line), CVR (black solid line) and at MPP (black dashed line).

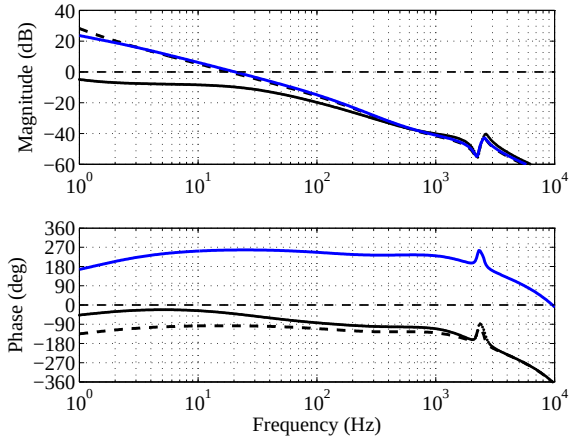

Fig. 3.16: Input voltage loop gains for single-current-feedback active damping scheme in CCR (blue line), CVR (black solid line) and at MPP (black dashed line).

3.5 Root locus analysis

Optimized active damping feedback design is explicitly shown for GCF converters in [28, 38] with proportional capacitor-current feedback, where a symbolic form of the optimum active damping feedback gain is proposed. Conversely, the root locus methods have been popular in case of ICF converters for analyzing the stability with capacitor-current or voltage-feedback active damping [31, 81, 82, 86], which are based on analysis of a

particular case and are not generally applicable. Optimum active damping feedback for ICF converter is proposed in [32], which does not address the effect of the system delay on the overall performance. Therefore, its validity regarding a real system with a 'worst-case' delay is questionable.

Accordingly, this section presents the stability analysis regarding the active damping design. Root-locus methods are often utilized, when determining the system stability with varying operational parameter, which usually is the controller gain K. The same methodology can be used also for active damping, where the system roots are drawn with respect to the varying active-damping gain and, thus, stable ranges for the gain can be obtained. The root-locus method could be replaced with Bode-plot analysis, but the former can be considered more convenient in this case as the time-domain behavior can be predicted. Additionally, root-locus methods are widely used in the literature regarding the design of active damping [26, 33, 36, 80–82, 86]. The location of the system roots determines the closed-loop transient response, i.e., the frequency and magnitude of oscillations as well as the rate of exponential decay. The transient performance of the current control also correlate with the output impedance characteristics, which is shown later in Chapter 4.

The stability of the current control is analyzed by investigating the closed-loop transfer function from the current reference to the output current, which was given in Section 3.4 as

$$\mathbf{G}_{\mathrm{cL}}^{\mathrm{out}} = \mathbf{G}_{\mathrm{cL}}^{\mathrm{AD}}(\mathbf{I}+\mathbf{L}_{\mathrm{out}})^{-1}\mathbf{L}_{\mathrm{out}}\left(\mathbf{G}_{\mathrm{cL}}^{\mathrm{AD}}\right)^{-1}. \tag{3.73}$$

Analyzing Eq. (3.73) instead of only the active damping loop reveals the transient behavior of the whole current loop. Practically, the performance of active damping is, thus, simultaneously evaluated, which simplifies the stability analysis of the current control. Note that only the d-component of (3.73) is analyzed in Sections 3.5.2 and 3.5.3, because the resonant-frequency behavior between the d and q-components is similar.

3.5.1 Mitigation of delay in active damping feedback

The delay significantly changes the behavior of the active damping feedback, thus affecting the converter stability. In order to improve the system stability characteristics, high-pass-filtered (HPF) capacitor-current feedback method is proposed for GCF converters in [80], where the HPF is used to mitigate the impact of the delay. Similar filtered feedback implementations are also analyzed in Sections 3.5.2 and 3.5.3 in order to improve the performance of active damping.

It was shown in Section 3.1.2 that also the imaginary part in (3.9) changes its sign

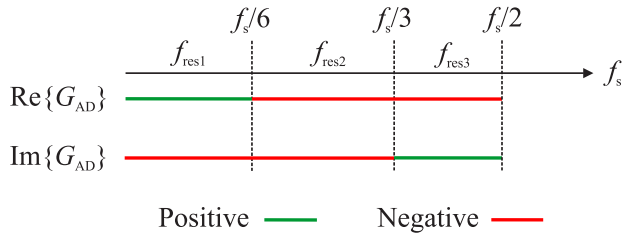

Fig. 3.17: Frequency-dependent behavior of the active damping feedback gain.

depending on the filter resonant frequency. This may not necessarily cause instability but it can still worsen the performance of the converter. Generally, the frequency-dependent behavior of active damping gain can be depicted as shown in Fig. 3.17. The real part is positive when $f_{\mathrm{res}} < f_{\mathrm{s}}/6$ whereas the imaginary part is negative. Therefore, the effect of the imaginary part is reduced by inducing phase boost on the feedback signal. However, the real and imaginary parts have same signs when $f_{\mathrm{s}}/6 < f_{\mathrm{res}} < f_{\mathrm{s}}/3$. This does not necessarily cause instability since the sign of the virtual resistor R_{d} can be changed. However, the HPF cannot improve the system performance when $f_{\mathrm{res}} > f_{\mathrm{s}}/6$ since it induces phase boost. To eliminate the effect of the imaginary part, a low-pass filter (LPF) must be implemented in order to induce phase lag around the resonant frequency.

Correspondingly, by further increasing the resonant frequency to $f_{\mathrm{s}}/3 < f_{\mathrm{res}} < f_{\mathrm{s}}/2$, where $f_{\mathrm{s}}/2$ is the Nyquist frequency, the real and imaginary parts have again the opposite signs. As a positive real part is required for active damping, the imaginary part becomes negative after the feedback inversion. Therefore, active damping characteristics are similar as in the case of $f_{\mathrm{res}} < f_{\mathrm{s}}/6$ and the HPF should be used to induce phase boost in order to negate the effect of the imaginary part.

Considering the high and low-pass filters, the HPF can be presented in the s-domain as $G_{\mathrm{HPF}} = s/(s + \omega_{\mathrm{cutoff}})$ where ω_{cutoff} is the desired cutoff frequency. The active damping gain in (3.25) is multiplied by the corresponding transfer function, thus, the virtual resistor value is used to adjust the gain of the HPF. Similarly, a low-pass filter can be presented in the s-domain as $G_{\mathrm{LPF}} = \omega_{\mathrm{cutoff}}/(s + \omega_{\mathrm{cutoff}})$, where ω_{cutoff} is the desired cutoff frequency. Due to the lack of explicit design rules regarding the HPF or LPF for ICF converters, the root locus diagrams in Sections 3.5.2 and 3.5.3 represent only the most optimized cases for corresponding filtered feedback implementations.

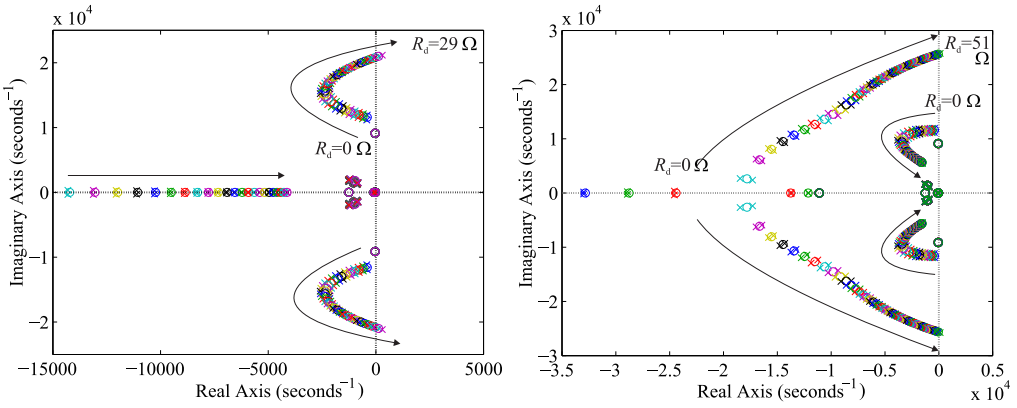

Fig. 3.18: Root locus of (a) proportional active damping and (b) high-pass-filtered active damping when $f_{\text{res}} < f_{\text{s}}/6$.

3.5.2 Multi-current-feedback active damping scheme

Case: $f_{\text{res}} < f_{\text{s}}/6$

Inverter with ICF control is naturally stable, due to inherent damping characteristics [32, 34], if the resonant frequency is less than $f_{\text{s}}/6$. Therefore, guaranteeing stability is quite straightforward and theoretically the active damping gain can be set to $R_{\text{d}} = 0\ \Omega$. This can be seen from Fig. 3.18a, which shows the root locus of (3.73) for proportional capacitor-current-feedback active damping. As evident, the poles lie in the LHP with $R_{\text{d}} = 0\ \Omega$ indicating inherent stability. By increasing the virtual resistor value, the poles shift first deeper in to the LHP and, thus, the converter exhibits more damped response with less oscillations. The maximum frequency for roots can be obtained with $R_{\text{d}} = 14\ \Omega$ yielding a frequency of $\omega_{\text{MAX}} \approx 2500$rad/s. Eventually, the root trajectory circles back to the RHP and crosses the imaginary-axis when $R_{\text{d}} = 29\ \Omega$, which is the maximum allowed virtual resistor value in this case.

Considering the high-pass filter, similar design rules as in [80] are adopted here. First, the converter cutoff-frequency must be set properly in order to provide necessary phase boost required by the active damping feedback. Here, the HPF cutoff frequency is set at the resonant frequency as $\omega_{\text{cutoff}} = \omega_{\text{res}}$. Clearly, the HPF in Fig. 3.18b improves the system stability as the poles are first moved deep into the LHP and closer to the x-axis, when compared to the case with proportional capacitor-current feedback and, therefore, this decreases the oscillations and increases the speed of transient decay. The maximum frequency of the poles is obtained with $R_{\text{d}} = 13\ \Omega$ as $\omega_{\text{MAX}} \approx 5000$rad/s. However, instability may still occur with higher virtual resistor values as the roots move

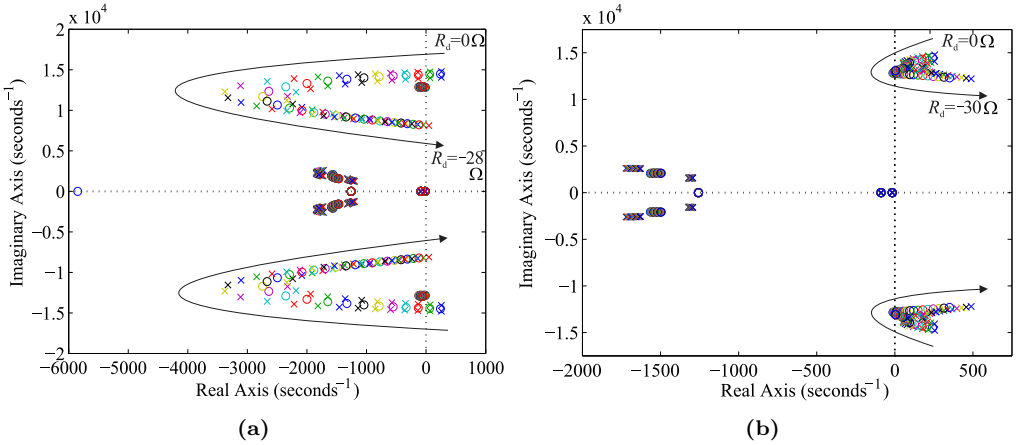

Fig. 3.19: Root locus of (a) proportional active damping and (b) high-pass-filtered active damping when $f_s/6 < f_{res} < f_s/3$, $\omega_{HPF} = \omega_{res}$.

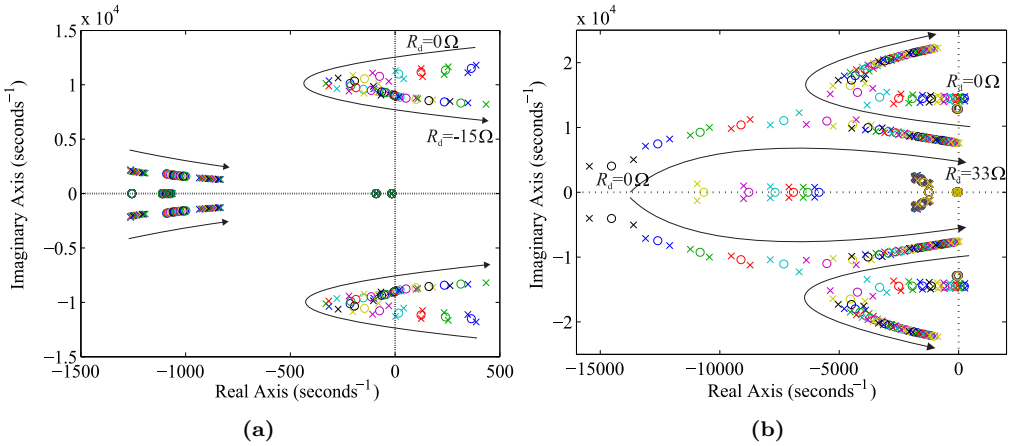

Fig. 3.20: Root locus of (a) high-pass-filtered active damping and (b) low-pass-filtered active damping when $f_s/6 < f_{res} < f_s/3$, $\omega_{HPF} = 0.2\omega_{res}$, $\omega_{LPF} = 2\omega_{res}$.

back into the RHP at $R_d = 51\ \Omega$. Comparing Figs. 3.18a and 3.18b, it is evident that the filtered feedback technique provides better current response (i.e., faster response with less oscillations).

Case: $f_{res} > f_s/6$

Regarding the stability of the converter, decreasing the sampling frequency will significantly affect the design of stable control system. When operating at frequencies $f_{res} > f_s/6$, the converter is no longer inherently stable and active damping must be used to ensure stable operation [34]. Similarly as for $f_{res} < f_s/6$, first the proportional

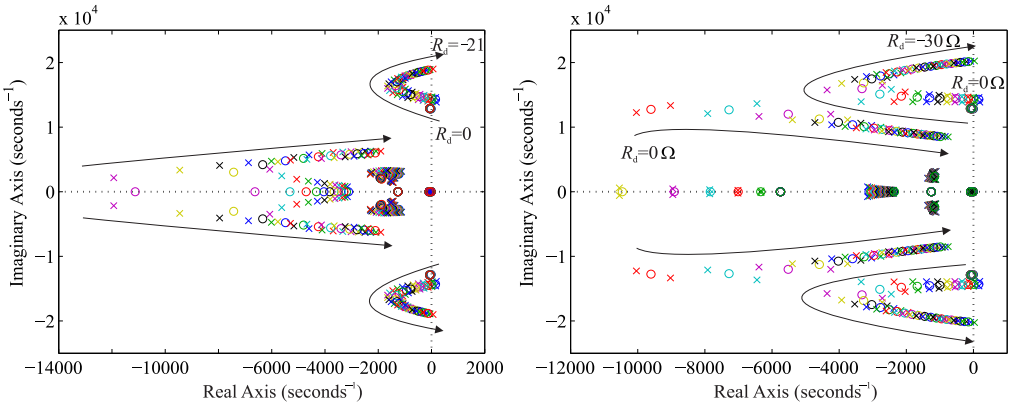

Fig. 3.21: Root locus of (a) proportional active damping and (b) high-pass-filtered active damping when $f_\mathrm{s}/3 < f_\mathrm{res} < f_\mathrm{s}/2$, $\omega_\mathrm{HPF} = 0.5\omega_\mathrm{res}$.

active damping feedback is analyzed when $f_\mathrm{s}/6 < f_\mathrm{res} < f_\mathrm{s}/3$ in Fig. 3.19a. Evidently, using $R_\mathrm{d} = 0\ \Omega$ causes unstable inverter dynamics, since the poles are located in the RHP, conversely to the case when $f_\mathrm{res} < f_\mathrm{s}/6$. However, similar parabolic root locus can be seen comparing to the case with $f_\mathrm{res} < f_\mathrm{s}/6$ (cf. Figs. 3.18a and 3.18b). Accordingly, first the roots move deeper into the LHP, which indicates improved stability margins. The maximum frequency of the roots is obtained when $R_\mathrm{d} = -12\ \Omega$ yielding $\omega_\mathrm{MAX} \approx 2200$rad/s. Similarly, the roots move back into the RHP, when the virtual resistor value is increased to $R_\mathrm{d} = -28\ \Omega$.

As discussed earlier, the high-pass filter provides improved stability characteristics when $f_\mathrm{res} < f_\mathrm{s}/6$. However, when $f_\mathrm{s}/6 < f_\mathrm{res} < f_\mathrm{s}/3$, the HPF will worsen the stability characteristics, which is demonstrated in Fig. 3.19b, where the cutoff frequency was chosen similarly as in the case for $f_\mathrm{res} < f_\mathrm{s}/6$, i.e., $\omega = \omega_\mathrm{res}$. Evidently, the HPF causes the roots to stay in the RHP at least with the used parameters, which indicates highly impaired stability margins. By lowering the HPF cutoff frequency from $\omega = \omega_\mathrm{res}$ to $\omega = 0.2\omega_\mathrm{res}$ the stability can be recovered as shown in Fig. 3.20a. However, the root trajectory is inferior compared to its proportional feedback counterpart shown in Fig. 3.19a as the optimum root location is obtained with $R_\mathrm{d} = -6\ \Omega$ yielding $\omega_\mathrm{MAX} \approx 200$rad/s. Maximum virtual resistor value can be observed to be around $R_\mathrm{d} = -15\ \Omega$.

To overcome the aforementioned stability problems, a low-pass filter must be implemented to reduce the effect of the delay-imposed imaginary part of the active damping feedback and to improve system stability. This case is shown in Fig. 3.20b, where the LPF cutoff-frequency was chosen as $\omega = 2\omega_\mathrm{res}$. Clearly, the system poles move deeper into the LHP compared to the case in Fig. 3.19a, which indicates fast and well-damped

step response of the current control. Accordingly, the most optimal properties regarding the stability are obtained when $R_\mathrm{d} = -15\ \Omega$ yielding $\omega_\mathrm{MAX} \approx 3500\mathrm{rad/s}$. Thus, the converter exhibits improved current-control response compared to the proportional active damping feedback and, therefore, the utilization of the low-pass filter is justified for $f_\mathrm{s}/6 < f_\mathrm{res} < f_\mathrm{s}/3$.

The last distinct resonant frequency region is restricted only by the Nyquist frequency as $f_\mathrm{s}/3 < f_\mathrm{res} < f_\mathrm{s}/2$, where the converter is still naturally unstable without the active damping, since the roots are located in the RHP when $R_\mathrm{d} = 0\ \Omega$. However, the imaginary part changes its sign from the previous case in this region and active damping feedback dynamics resemble the case of $f_\mathrm{res} < f_\mathrm{s}/6$. Fig. 3.21a shows the root trajectory in case of proportional active damping feedback when $f_\mathrm{s}/3 < f_\mathrm{res} < f_\mathrm{s}/2$. The optimal value for the virtual resistor is $R_\mathrm{d} = -12\ \Omega$ yielding $\omega_\mathrm{MAX} \approx 1500\mathrm{rad/s}$. Maximum value is limited to $R_\mathrm{d} = -21\ \Omega$. Moreover, the effect of the HPF is shown in Fig. 3.21b with the HPF cutoff-frequency of $\omega = 0.5\omega_\mathrm{res}$. Clearly, the roots are moved deeper into the LHP and the optimum current-controller response is obtained with $R_\mathrm{d} = -12\ \Omega$, $\omega_\mathrm{MAX} \approx 2300\mathrm{rad/s}$, which is significantly better than with the proportional feedback and, therefore, its necessity can be justified.

As a conclusion, it is important to acknowledge the overall effect of the delay on the system stability. Accordingly, active damping design must be performed carefully, especially with higher $f_\mathrm{res}/f_\mathrm{s}$-ratios. Furthermore, in order to eliminate the effect of the system delay on the active damping performance, the selection of capacitor current filtering method is essential. That is, a HPF should be utilized when $f_\mathrm{res} < f_\mathrm{s}/6$ and $f_\mathrm{s}/3 < f_\mathrm{res} < f_\mathrm{s}/2$. Moreover, a LPF is necessary for improved robustness when $f_\mathrm{s}/6 < f_\mathrm{res} < f_\mathrm{s}/3$.

3.5.3 Single-current-feedback active damping scheme

Design constraints on single-current-feedback scheme

As discussed earlier, the frequency region $f_\mathrm{res} > f_\mathrm{s}/6$ can be divided into two distinct parts, similar to the multi-current feedback system, as the frequency-dependent behavior of the delay does not change. Accordingly, $f_\mathrm{s}/6 < f_\mathrm{res} < f_\mathrm{s}/3$ and $f_\mathrm{s}/3 < f_\mathrm{res} < f_\mathrm{s}/2$ can be identified. However, the active damping loop changes the single-current-feedback scheme profoundly, and the same design rules do not apply as for the multi-current counterpart.

Regarding the available literature on the design constraints, it has been observed in case of GCF converters that the system stability is difficult to achieve when $f_\mathrm{s}/3 < f_\mathrm{res} < f_\mathrm{s}/2$ due to unavoidable nonminimum-phase characteristics [36]. In fact, $f_\mathrm{res} < 0.28 f_\mathrm{s}$ has been found to be practical upper limit to the resonant frequency as the HPF implementation inside the control system becomes inaccurate due to the noise amplification

and sampling errors. This lowers the achievable operating range to $f_s/6 < f_{res} < 0.28 f_s$. Similar restrictions can be found for ICF converter, which are analyzed through the frequency-domain behavior of the active damping loop.

According to Figs. 3.3 and 3.7, the active damping loops for multi and single-current-feedback schemes can be given by

$$\begin{aligned} L_{AD-d}^{multi} &= G_{delay} G_{AD} (G_{cL-d} - G_{co-d}) \\ L_{AD-q}^{multi} &= G_{delay} G_{AD} (G_{cL-q} - G_{co-q}) \end{aligned} , \tag{3.74}$$

$$\begin{aligned} L_{AD-d}^{single} &= G_{delay} G_{AD} G_{cL-d} \\ L_{AD-q}^{single} &= G_{delay} G_{AD} G_{cL-q} \end{aligned} , \tag{3.75}$$

respectively. Since the d and q-components in both open-loop G_{cL} and G_{co} are practically identical with each other at high frequencies, only the d-component is considered here for simplicity. Fig. 3.22 shows the comparison of the active damping loop of multi and single-current-feedback schemes. Additionally, for a single-current scheme, both negative and positive damping gains (i.e., inverted and non-inverted) are presented. As discussed in the previous section in case of multi-current-feedback scheme, the active damping gain must be inverted to negative when the critical frequency ($f_{res} = f_s/6$) is exceeded. However, in case of single-current-feedback scheme, this logic does not hold anymore.

The active damping loop under single-current-feedback system may pose instability problems due to its phase behavior, and the instability is partially caused by the sign of the active damping gain. Accordingly, it is evident from Fig. 3.22 that the phase crosses over -180 degrees when $|L_{AD}^{single}| \geq 1$ if a negative virtual resistor value is used. This differs from the multi-current-feedback counterpart, where a negative value would be used for active damping gain when $f_{res} > f_s/6$. Aforementioned phase crossing at the middle frequencies can be overcome by using a positive active damping gain, but the loop is still prone to instability due to the low phase margin in vicinity of the LCL-filter resonant frequency.

In order to decrease the gain at the mid frequencies and increase the phase at the higher frequencies, a high-pass filter is utilized. Ideally, a 90 degree phase boost could be obtained with a pure derivative gain 's'. However, high-frequency noise would be excessively amplified and, moreover, the realization of such ideal derivative element is difficult. Instead, a high-pass filter, which can be implemented in digital controllers quite easily, is used to produce the desired phase boost for a certain frequency range. Accordingly, the filter cutoff frequency must be higher than the resonant frequency as the phase boost is required for higher frequencies.

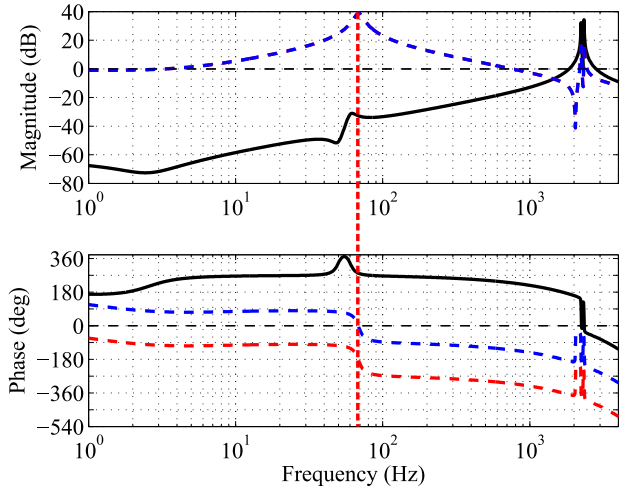

Fig. 3.22: Active damping loop gains for capacitor-current feedback with $R_\mathrm{d} \leq 0\ \Omega$ (solid black line), inverter-current feedback with $R_\mathrm{d} \geq 0\ \Omega$ (blue dashed line) and inverter-current feedback with $R_\mathrm{d} \leq 0\ \Omega$ (red dashed line). Note that the magnitude plots for inverter current feedback active damping overlap each other. Phase crossing over -180^o is denoted with a vertical dashed line.

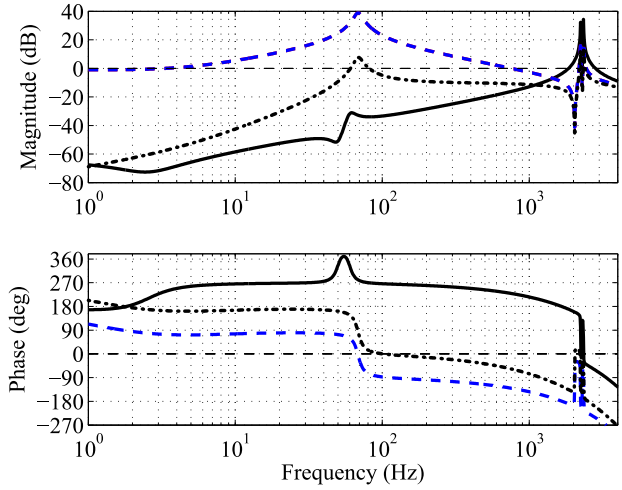

Fig. 3.23: Active damping loop gains for capacitor-current feedback (solid black line), inverter-current feedback with $R_\mathrm{d} \geq 0\ \Omega$ (blue dashed line) and high-pass-filtered inverter-current feedback with $R_\mathrm{d} \geq 0\ \Omega$ (black dash-dotted line).

Figs. 3.23 and 3.24 show the proportional and high-pass-filtered active damping loop gains in case of single-current-feedback schemes as well as the proportional multi-current-feedback counterpart. As evident in Fig. 3.24, if the HPF is not utilized, the active damping loop exhibits two -180 degree crossings to the same direction (i.e., two

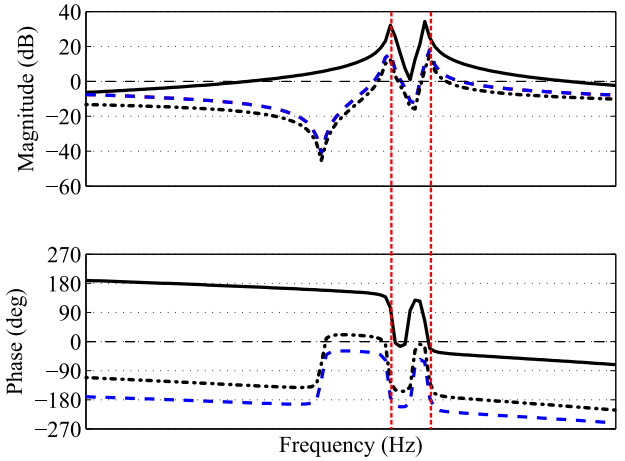

Fig. 3.24: Enlarged depiction of the resonant frequency behavior in Fig. 3.23. Phase crossings over −180 degrees are denoted with red vertical dashed lines, $f_{\mathrm{res}} > f_{\mathrm{s}}/6$.

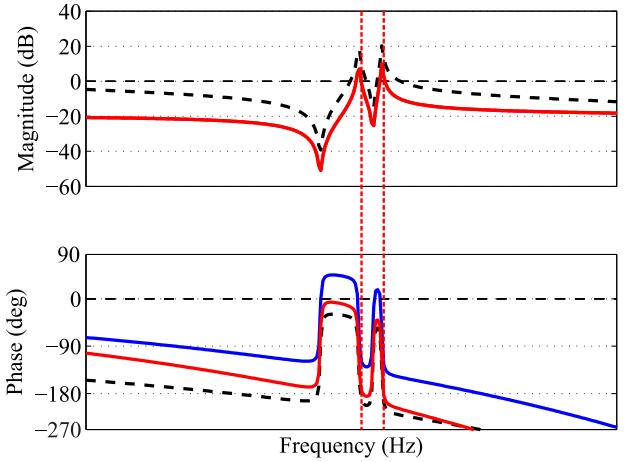

Fig. 3.25: Active damping loop gains for single-current-feedback schemes: HPF AD $f_{\mathrm{s}}/6 < f_{\mathrm{res}} < f_{\mathrm{s}}/3$ (solid blue line), HPF AD $f_{\mathrm{s}}/3 < f_{\mathrm{res}} < f_{\mathrm{s}}/2$ (solid red line) and proportional AD (dashed black line). Note that the red line overlaps with the blue line in the upper figure.

Nyquist plot encirclements around (-1,0)) with $|L_{\mathrm{AD}}^{\mathrm{single}}| \geq 1$ indicating unstable dynamics. However, the high-pass filter increases the phase sufficiently and the stability can be, therefore, guaranteed. Furthermore, the HPF prevents the low-frequency harmonics from passing through the active damping loop and, therefore, the high-pass-filtered gain exhibits highly attenuated low-frequency behavior and resembles the capacitor-current-feedback active damping.

Considering the frequency region of $f_{\mathrm{s}}/3 < f_{\mathrm{res}} < f_{\mathrm{s}}/2$ in case of the single-current-feedback scheme, stability is hardly achieved. Fig. 3.25 presents comparison between the

active damping loops when $f_s/3 < f_{res} < f_s/2$ and $f_s/6 < f_{res} < f_s/3$. Accordingly, the sampling frequency is set exactly at $f_{res} = f_s/3 \rightarrow f_s = 3f_{res}$. Clearly, the phase crosses -180 degrees when $|L_{AD}^{single}| \geq 1$ even with the phase boost induced by the HPF. Thus, the observation agrees with the results proposed in [36] for GCF converters.

In conclusion, a high-pass filter must be used for single-current-feedback active damping when operating under $f_{res} > f_s/6$. Moreover, the limit for the minimum sampling frequency can be given as $f_s \approx 3f_{res}$, which is the same result as obtained for GCF converters. Therefore, the same active damping design logic seems to apply for both single-current-feedback ICF and GCF converters with active damping.

Case: $f_{res} < f_s/6$

Fig. 3.26a presents the root locus for proportional active damping in single-current-feedback scheme. Regarding the resonant frequency region, active damping is not necessarily required for stability, and the converter can operate with $R_d = 0\ \Omega$, which would still lead to highly oscillatory as well as long transient response due to minimal stability margins. By increasing the virtual resistor value, the stability margins can be improved and the optimal damping is obtained when $R_d = 23\ \Omega$ yielding $\omega_{MAX} \approx 2200$rad/s. The root locus crosses the imaginary-axis into the RHP when $R_d = 41\ \Omega$, which is the maximum value for virtual resistor in this case.

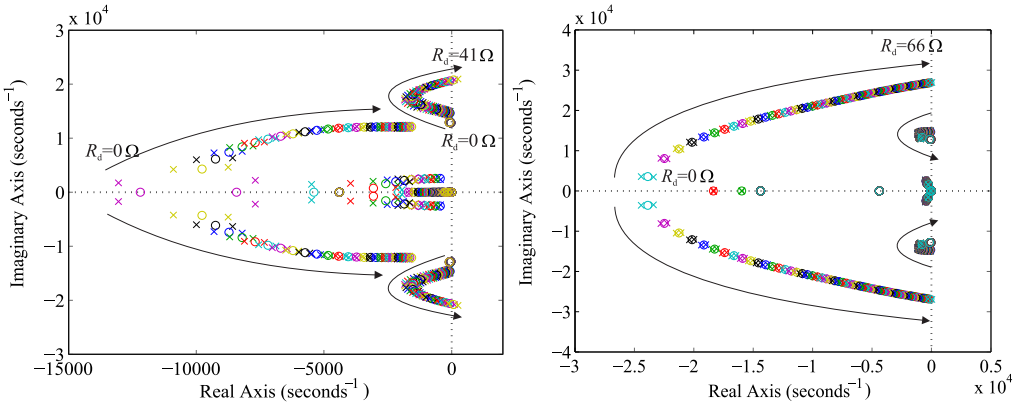

Fig. 3.26: Root locus of (a) proportional active damping and (b) high-pass-filtered active damping when $f_{res} < f_s/6$, $\omega_{HPF} = \omega_{res}$.

As the frequency region of $f_{res} < f_s/6$ is considered, a high-pass filter should improve the stability characteristics of active damping. Root locus for the corresponding case is shown in Fig. 3.26b. Inherent stability is obtained similarly to the proportional feedback case, but the root locus is inferior. More accurately, the roots do not move far from the

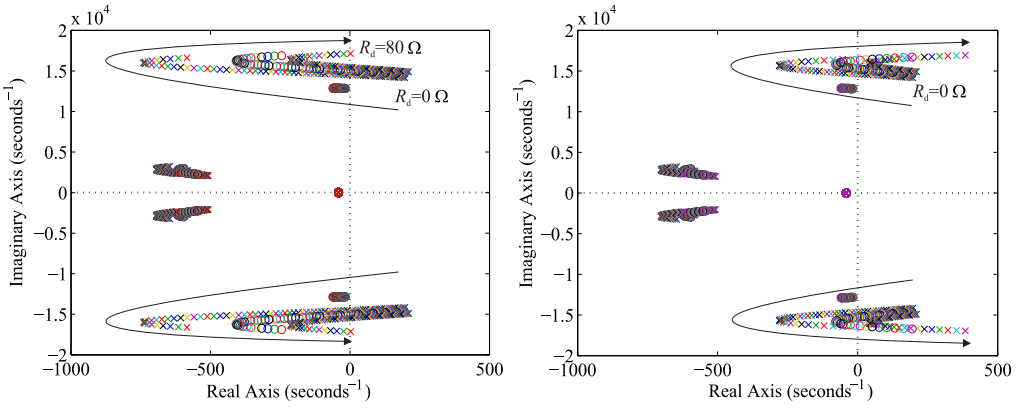

Fig. 3.27: Root locus of high-pass-filtered active damping when (a) high cutoff frequency and (b) low cutoff-frequency is used, $f_s/6 < f_{res} < 0.28f_s$, $\omega_{HPF\text{-}high} = 3.5\omega_{res}$, $\omega_{HPF\text{-}low} = 1.5\omega_{res}$.

imaginary axis, and the poles with the lowest frequency are at the maximum distance from the imaginary axis when $R_d = 27\ \Omega$ yielding $\omega_{MAX} \approx 2000$rad/s. Clearly, the high-pass filter does not improve the system response as it does in the multi-current scheme under the same conditions. However, the gain can be adjusted for a wider range as the maximum virtual resistor value is $R_d = 66\ \Omega$. This behavior can be explained by analyzing Figs. 3.24 and 3.25, which show that the high-pass filter slightly decreases the gain at the resonant frequency compared to the proportional feedback counterpart. Furthermore, the gain margin is quite low as the phase crosses -180 degrees immediately after the resonant peaks. Therefore, the effect of the active damping feedback on the resonance attenuation is decreased, which is observed as inferior root locus. Later in Section 4, it is shown that this root locus behavior affects significantly the output impedance at the resonant frequency.

Case: $f_{res} > f_s/6$

As discussed earlier, only filtered feedback methods for active damping suffice for analysis when $f_{res} > f_s/6$ due to the persistent unstable characteristics. Moreover, the sampling frequency is restricted as $f_s/6 < f_{res} < f_s/3$. For comparison, two cases with different high-pass filter cutoff frequencies are shown in Figs. 3.27a and 3.27b. In the former, high-pass filter is designed to introduce sufficient phase boost at the resonant frequency and, therefore, the converter is stable. Considering the root locus, slightly inferior dynamics can be observed (cf. Figs. 3.26a and 3.26b) as the maximum distance of the system roots from the imaginary axis are obtained with $R_d = 56\ \Omega$ yielding $\omega_{MAX} \approx 200$rad/s, which indicates rather slow current response and the system being close to marginal stability.

As evident from Fig. 3.27b, the high-pass filter with low cutoff-frequency yields unstable converter dynamics due to insufficient phase boost by the HPF, which was shown in Fig. 3.24. It can be, therefore, concluded that single-current-feedback ICF converter should be operated in the resonant frequency region of $f_{\mathrm{res}} < f_{\mathrm{s}}/6$ for improved stability. Furthermore, the active damping design when operating under $f_{\mathrm{res}} > f_{\mathrm{s}}/6$ should be performed carefully since the converter is highly susceptible to instability. Especially, optimizing the HPF design and the active damping gain is essential.

4 OUTPUT IMPEDANCE WITH ACTIVE DAMPING

This chapter presents the output-impedance-properties of a three-phase grid-connected inverter with active damping. The relation between the shape of the output impedance and the active damping design is elaborated according to the observations regarding the root-locus analysis in Sections 3.5.2 and 3.5.3. Furthermore, a comprehensive comparison between the multi and single-current-feedback active damping schemes considering the output impedance is presented.

4.1 Output impedance analysis

Regarding the output-impedance analysis, some practical matters are addressed next for clarification. The output *impedance* (i.e., $1/Y_\mathrm{o}$) is analyzed in this section as it is more comprehensible regarding the impedance-based stability evaluation. However, the output *admittance* is analyzed considering the active-damping-affected open-loop characteristics in Section 4.2.

The effect of active damping on the output impedance is visible at frequencies higher than the current-controller bandwidth due to lack of control gain in the current loop. Accordingly, the most interesting properties of the impedance are concentrated in vicinity of the resonant frequency and, therefore, the frequency-domain impedance plots are presented only from 100 Hz upwards. It should be also noted that only the d-component is analyzed, since the mid-to-high-frequency characteristics (>100 Hz) between the d and q-components are nearly identical as shown later in Chapter 5.

4.1.1 Multi-current feedback scheme

Case: $f_\mathrm{res} < f_\mathrm{s}/6$

Fig. 4.1 shows the d-component of the output impedance with proportional capacitor-current feedback. Accordingly, R_d values of $[5, 15, 27]$ Ω are chosen for the analysis as they represent the important points in the corresponding root locus in Fig. 3.18a, i.e., the minimum and maximum distances from the real and imaginary axes. Fig. 4.1 shows that the shape of the impedance in vicinity of the resonant frequency varies as the virtual resistor value is modified. First, by increasing the virtual resistor from $R_\mathrm{d} = 5$ Ω (solid line) to $R_\mathrm{d} = 15$ Ω (dashed line) the magnitude of the impedance in vicinity of the

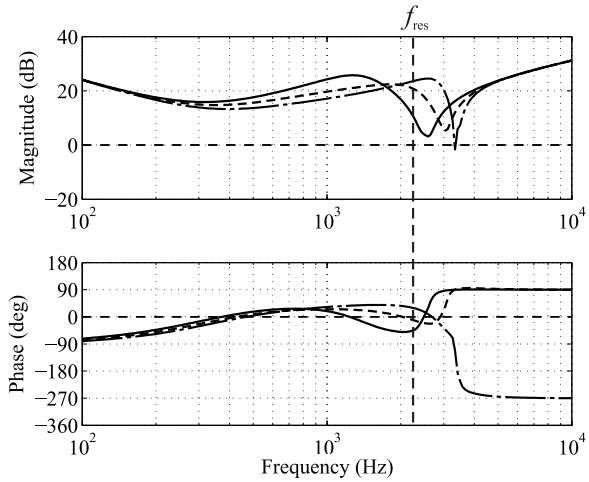

Fig. 4.1: Predicted d-component of the output impedance with proportional AD, R_{d}= 5 Ω (solid line), R_{d}= 15 Ω (dashed line) and R_{d}= 27 Ω (dash-dotted line).

resonant frequency increases from 4 dB to its highest value at 8 dB. Regarding the root locus, when $R_{\mathrm{d}} = 5\Omega \rightarrow 15\Omega$, the system roots move farther from the imaginary axis yielding faster current control response. The output impedance is impaired and decreases below 0 dB if the active-damping-feedback gain is set to $R_{\mathrm{d}} = 27\ \Omega$, which is close to the maximum limit as shown in Fig. 3.18a. Moreover, the output impedance loses its passive characteristics, i.e., the phase $\theta \notin [-90^{\mathrm{o}}...90^{\mathrm{o}}]$.

To decrease the effect of the imaginary part of the active-damping feedback, a high-pass filter is inserted in the active-damping loop in order to provide the necessary phase boost. Fig. 4.2 shows an identical case to Fig. 4.1 regarding the virtual-resistor values. The HPF cutoff frequency was chosen as $\omega_{\mathrm{cutoff}} = \omega_{\mathrm{res}}$ complying with the design rules proposed in [80]. Clearly, the output-impedance magnitude in vicinity of the resonant frequency is significantly increased compared to the case with pure proportional capacitor-current feedback. The highest magnitude of 15 dB is obtained with R_{d}= 15 Ω. Correspondingly, the root locus in Fig. 3.18b was also observed to exhibit improved properties as the poles move farther from the imaginary axis (cf. Fig. 3.18a). As an outcome of the higher impedance magnitude, grid-voltage harmonics are mitigated more effectively and the grid-current response would be improved. In addition, the phase of the output impedance is passive even with larger virtual resistor values, which decreases the possibility for impedance-based instability.

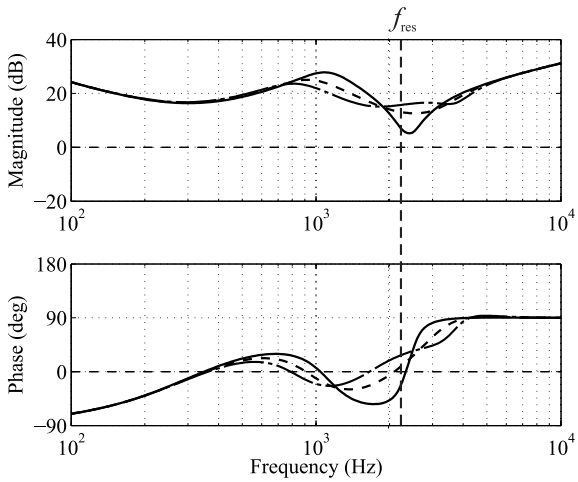

Fig. 4.2: Predicted d-component of the output impedance with HPF AD, R_d= 5 Ω (solid line), R_d= 15 Ω (dashed line) and R_d= 27 Ω (dash-dotted line), $\omega_\mathrm{cutoff} = \omega_\mathrm{res}$.

Case: $f_\mathrm{res} > f_\mathrm{s}/6$

Fig. 4.3 shows the output impedance using proportional AD feedback with $R_\mathrm{d} = [-5, -10, -20]$ Ω, where the resonant frequency is set as $f_\mathrm{s}/6 < f_\mathrm{res} < f_\mathrm{s}/3$. The sign of the active-damping-feedback gain is changed as required by the operating conditions. Considering Fig. 4.3, the magnitude of the impedance in vicinity of the resonant frequency changes similarly as in Fig. 4.1 for $f_\mathrm{res} < f_\mathrm{s}/6$. That is, the magnitude is first increased from 0 dB to its maximum value at 10 dB as the virtual resistor value is decreased from $R_\mathrm{d} = -5$ Ω to $R_\mathrm{d} = -10$ Ω, respectively. Furthermore, the magnitude decreases as the virtual resistor value is further decreased to $R_\mathrm{d} = -20$ Ω. As can be observed, the output impedance is not passive and, therefore, the possibility for high-frequency impedance-based interactions is evident [50]. In fact, this active-type behavior is an inherent property of the output impedance when $f_\mathrm{res} > f_\mathrm{s}/6$, which is explained in detail in Section 4.2.

Considering the frequency region of $f_\mathrm{s}/6 < f_\mathrm{res} < f_\mathrm{s}/3$, a high-pass filter in the AD feedback loop impairs the stability characteristics as predicted by the root locus in Fig. 3.19b. This also yields inferior output impedance characteristics as shown in Fig. 4.4, where $\omega_\mathrm{cutoff} = 0.5\omega_\mathrm{res}$ and $R_\mathrm{d} = [-5, -10, -20]$ Ω. Comparing Figs. 4.3 and 4.4, it is evident that the HPF impairs the output impedance in vicinity of the resonant frequency as the magnitude in Fig. 4.4 remains below 0 dB with all virtual resistor values and, therefore, voltage harmonics can easily affect the grid current.

Conversely, low-pass filtering the capacitor current yields a considerable improvement in the impedance characteristics, which is in agreement with the observations regarding

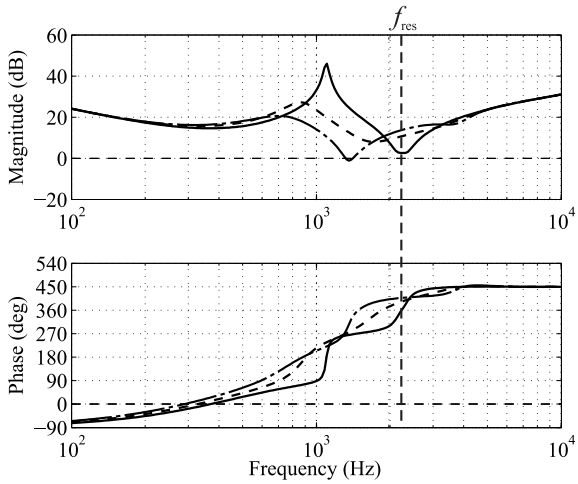

Fig. 4.3: Predicted d-component of the output impedance with prop. AD, R_d= -5 Ω (solid line), R_d= -10 Ω (dashed line) and R_d= -14 Ω (dash-dotted line), $\omega_\mathrm{cutoff} = \omega_\mathrm{res}$.

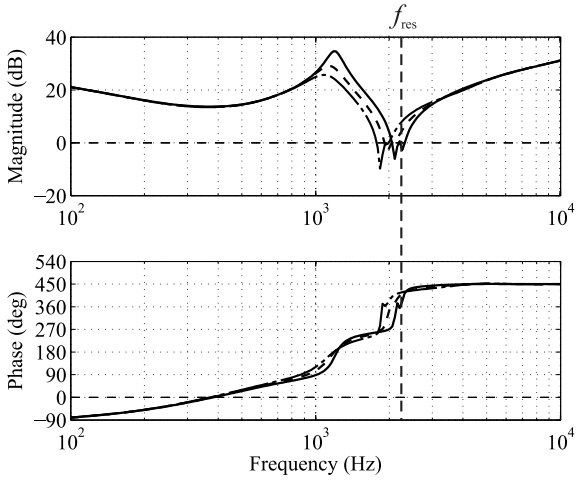

Fig. 4.4: Predicted d-component of the output impedance with HPF AD, R_d= -5 Ω (solid line), R_d= -10 Ω (dashed line) and R_d= -14 Ω (dash-dotted line), $\omega_\mathrm{cutoff} = \omega_\mathrm{res}$.

the root-locus analysis in Fig. 3.20b. Fig. 4.5 shows the output impedance with $R_\mathrm{d} = [-5, -10, -20]$ Ω and $\omega_\mathrm{cutoff} = 2\omega_\mathrm{res}$. Clearly, the impedance magnitude in vicinity of the resonant frequency is considerably higher compared with the HPF AD case shown in Fig. 4.4 and slightly higher compared with the case of pure proportional AD feedback shown in Fig. 4.3. The highest impedance magnitude with LPF AD can be obtained by selecting R_d= -15 Ω as indicated by the corresponding root trajectory (cf. Fig. 3.20b). Moreover, the output impedance is passive with small virtual-resistor values and, therefore, the risk

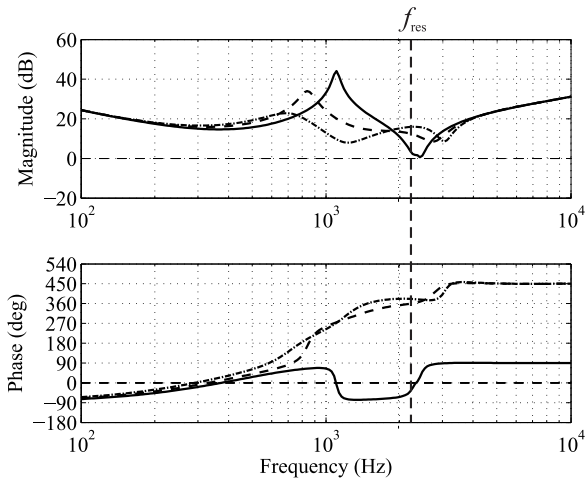

Fig. 4.5: Predicted d-component of the output impedance with LPF AD, R_d= -5 Ω (solid line), R_d= -10 Ω (dashed line) and R_d= -20 Ω (dash-dotted line), $\omega_\mathrm{cutoff} = \omega_\mathrm{res}$.

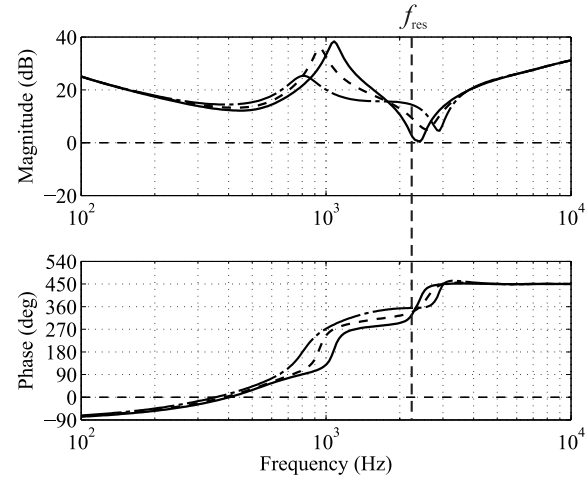

Fig. 4.6: Predicted d-component of the output impedance with prop. AD, R_d= -5 Ω (solid line), R_d= -15 Ω (dashed line) and R_d= -25 Ω (dash-dotted line).

for impedance-based instability is negligible in that case. However, small virtual-resistor value causes relatively low impedance magnitude in vicinity of the resonant frequency, which indicates poor robustness against the grid-voltage harmonics.

By further changing the sampling frequency as $f_\mathrm{s}/3 < f_\mathrm{res} < f_\mathrm{s}/2$, the active damping implementation must be again changed in order to achieve improved performance. Fig. 4.6 shows the output impedance with pure proportional active-damping feedback, where $R_\mathrm{d} = [-5, -15, -25]$ Ω. The overall magnitude is low, which can be slightly improved

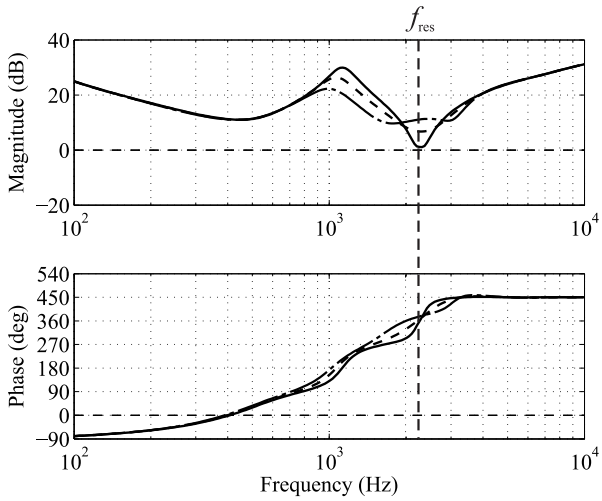

Fig. 4.7: Predicted d-component of the output impedance with HPF AD, R_d= -5 Ω (solid line), R_d= -15 Ω (dashed line) and R_d= -25 Ω (dash-dotted line), $\omega_\mathrm{cutoff} = \omega_\mathrm{res}$.

by selecting the active damping feedback gain properly. As discussed in Section 3.5, the HPF with the present sampling frequency induces improved current-control properties as is evident in the root locus in Fig. 3.21b. This yields higher impedance magnitude in vicinity of the resonant frequency as is shown in Fig. 4.7 with $R_\mathrm{d} = [-5, -15, -25]$ Ω. Accordingly, the magnitude of the output impedance can be increased from 1 dB to over 10 dB, which is a significant improvement, and has positive effect on robustness of the converter against grid background voltage harmonics.

By considering the aforementioned impedance analysis in case of the multi-current-feedback scheme, it can be concluded that the HPF is not needed when $f_\mathrm{s}/6 < f_\mathrm{res} < f_\mathrm{s}/3$, and should it be omitted considering the output impedance magnitude as well as the overall converter stability. Instead, a low-pass filter in the capacitor-current feedback should be used to increase the magnitude of the output impedance near the resonant frequency and to improve converter stability. Conversely, the HPF is recommended regarding the overall stability and the output impedance characteristics when $f_\mathrm{res} < f_\mathrm{s}/6$ and $f_\mathrm{s}/3 < f_\mathrm{res} < f_\mathrm{s}/2$. Regarding the relation between the root locus analysis and the shape of the output impedance, it is worth noting that the root locus may suffice in order to design the output impedance with high magnitude in vicinity of the resonant frequency. However, the phase behavior cannot be concluded from such loci and, therefore, pure root-locus design does not guarantee stable operation as the impedance-based interactions are based also on the phase behavior.

4.1.2 Single-current-feedback scheme

As discussed in Section 3.5.3, the single-current-feedback scheme exhibits inherent constraints for the control system design, which, in turn, limits the analysis of the output impedance for resonant frequency regions of $f_{\mathrm{res}} < f_{\mathrm{s}}/6$ and $f_{\mathrm{s}}/6 < f_{\mathrm{res}} < f_{\mathrm{s}}/3$. In the naturally stable frequency region, both proportional and HPF active damping feedback schemes are analyzed. Conversely, for $f_{\mathrm{res}} > f_{\mathrm{s}}/6$, only the HPF feedback scheme is evaluated.

Case: $f_{\mathrm{res}} < f_{\mathrm{s}}/6$

Fig. 4.8 shows the output impedance with proportional active damping feedback using virtual resistor values of $R_{\mathrm{d}} = [-10, -20, -30]\ \Omega$. As can be observed, the behavior of the impedance magnitude is similar to the multi-current-feedback scheme due to the parabolic root locus (cf. Fig. 3.26a), which induces corresponding behavior on the output impedance. Accordingly, the magnitude is at highest, when the root trajectory is farthest from the imaginary axis as shown in Fig. 3.26a with $R_{\mathrm{d}} = -21\ \Omega$. However, the magnitude from 100 Hz to 1 kHz is increased compared to its multi-current-feedback-scheme counterpart shown in Fig. 4.1. The impedance exhibits also a phase flip over 180 degrees at lower frequencies, when a small active damping gain is used, which indicates a positive real part and non-passivity of the impedance, i.e., $\mathrm{Re}\{Z_{\mathrm{o}}\} \geq 0$.

Regarding the magnitude increase when $100 < f < 1000$ Hz, it is related to the active-damping-affected open-loop dynamics, which are more elaborated in Section 4.2. The low-frequency phase flip, in turn, was observed to be related to the design of the input-voltage control. More precisely, the input-voltage-control loop should contain a high phase margin in order to avoid the low-frequency phase flip. However, the input-control optimization regarding the aforementioned phenomenon is not included in this thesis, although it affects the impedance-based behavior of the converter and should be addressed in the future research. A simple method to overcome the active-type impedance in this case is by the filtering the active-damping feedback, which maintains the passive output-impedance characteristics.

Fig. 4.9 shows the output impedance affected by the HPF active-damping method with $R_{\mathrm{d}} = [-10, -20, -30]\ \Omega$ and $\omega_{\mathrm{cutoff}} = \omega_{\mathrm{res}}$. It can be observed that the phase of the impedance is passive, and the low-frequency phase flip shown in Fig. 4.8 is absent. However, the output impedance magnitude in vicinity of the resonant frequency can be considered slightly inferior or equivalent compared to the case with pure proportional active-damping feedback, which is in accordance with the root-locus analysis shown in Figs. 3.26a and 3.26b. Furthermore, the magnitude increase in the range of 100-1000 Hz observed in the pure proportional active-damping scheme is absent, because the charac-

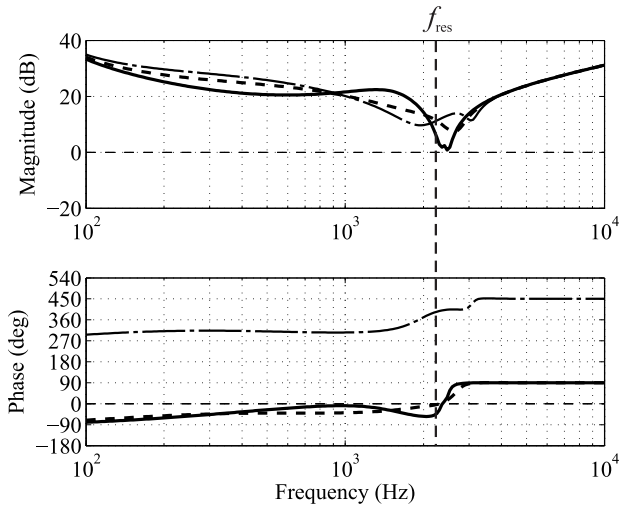

Fig. 4.8: Predicted d-component of the output impedance with proportional AD, R_d= -10 Ω (solid line), R_d= -20 Ω (dashed line) and R_d= -30 Ω (dash-dotted line).

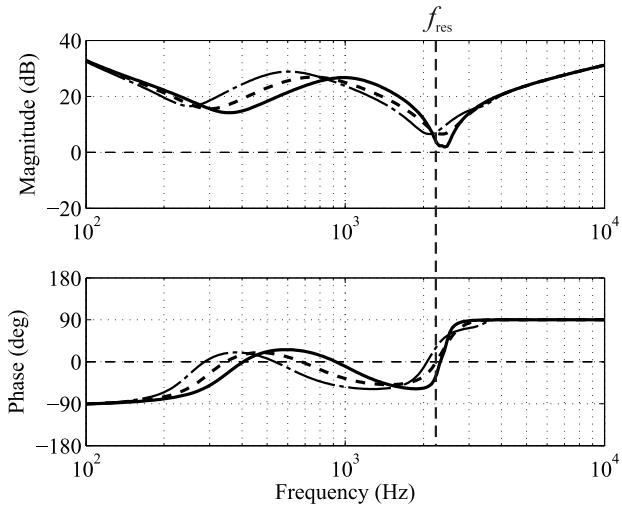

Fig. 4.9: Predicted d-component of the output impedance with HPF AD, R_d= -10 Ω (solid line), R_d= -20 Ω (dashed line) and R_d= -30 Ω (dash-dotted line), $\omega_\mathrm{cutoff} = \omega_\mathrm{res}$.

teristics resemble the capacitor-current-feedback active damping as discussed in Section 3.5.3.

Case: $f_\mathrm{res} > f_\mathrm{s}/6$

Only the filtered active-damping-feedback implementation provides stable dynamics, when $f_\mathrm{res} > f_\mathrm{s}/6$ in case of the single-current-feedback scheme. Accordingly, Fig. 4.10

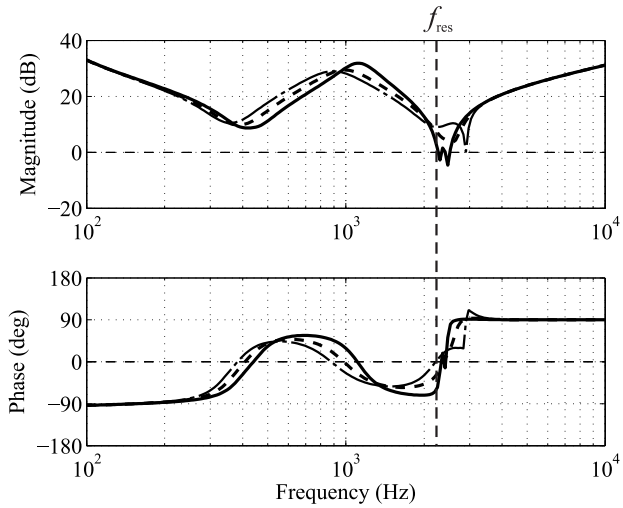

Fig. 4.10: Predicted d-component of the output impedance with HPF AD, R_{d}= 20 Ω (solid line), R_{d}= 40 Ω (dashed line) and R_{d}= 60 Ω (dash-dotted line), $\omega_{\mathrm{cutoff}} = 3.5\omega_{\mathrm{res}}$.

shows the output impedance with incrementing virtual resistor value as $R_{\mathrm{d}} = [20, 40, 60]$ Ω. The high-pass-filter cutoff frequency was set at relatively high frequency ($\omega_{\mathrm{cutoff}} = 3.5\omega_{\mathrm{res}}$) in order to provide the necessary phase boost at the resonant frequency. Evidently, the shape of the impedance resembles the case shown in Fig. 4.9 for $f_{\mathrm{res}} < f_{\mathrm{s}}/6$. Regarding the root locus shown in Fig. 3.27a, it is hard to obtain high output impedance in this case as the roots stay in the vicinity of the imaginary axis. The highest magnitude is obtained by setting the virtual resistor value between 50-60, which subsequently yields an impedance magnitude of around 5 dB. Moreover, the output impedance is passive, which is contrary to the multi-current-feedback scheme operating under $f_{\mathrm{res}} > f_{\mathrm{s}}/6$. The explanation for the aforementioned behavior is given in the following section.

4.2 Comparison of single and multi-current-feedback schemes

Considering the analysis in the previous sections, the multi and single-current-feedback active-damping schemes exhibit different output admittance properties, yet the causes might not be clear. For example, the single-current-feedback scheme has lower admittance below the resonant frequency. When the HPF is utilized, it resembles the behavior of the multi-current-feedback active damping scheme. Moreover, the admittance remains passive in case of the single-current-feedback implementation when $f_{\mathrm{res}} > f_{\mathrm{s}}/6$. Accordingly, this section discusses the matter by analyzing the detailed effect of the active damping on specific system transfer functions in order to clarify the observed properties such as:

- The differences in the low-frequency (100-1000 Hz) magnitude of the output admittance between the single and multi-current-feedback schemes.
- The non-passivity of the output admittance in case of the multi-current-feedback active damping implementation inside the frequency region of $500 < f < 2000$ Hz.

4.2.1 Magnitude of output admittance

The active-damping feedback modifies the corresponding open-loop transfer functions inside its control bandwidth as discussed in Sections 3.2 and 3.3. Therefore, in the multi-current-feedback scheme, the transfer functions are modified in vicinity of the resonant frequency, and the single-current-feedback scheme modifies the transfer functions also at medium frequencies. Accordingly, Eqs. (4.1) and (4.2) present the active-damping-affected output admittances (cf. Eqs. 3.22 and 3.35) as

$$\begin{aligned} Y_{\mathrm{o-d}}^{\mathrm{AD-multi}} &= Y_{\mathrm{o-d}} - \frac{G_{\mathrm{delay}} G_{\mathrm{AD}} G_{\mathrm{co-d}} \left(G_{\mathrm{oL-d}} - Y_{\mathrm{o-d}}\right)}{1 + G_{\mathrm{delay}} G_{\mathrm{AD}} \left(G_{\mathrm{cL-d}} - G_{\mathrm{co-d}}\right)} \\ &= Y_{\mathrm{o-d}} - \frac{L_{\mathrm{AD-d}}^{\mathrm{multi}}}{1 + L_{\mathrm{AD-d}}^{\mathrm{multi}}} \frac{G_{\mathrm{co-d}} \left(G_{\mathrm{oL-d}} - Y_{\mathrm{o-d}}\right)}{G_{\mathrm{cL-d}} - G_{\mathrm{co-d}}} \\ &= Y_{\mathrm{o-d}} - G_{\mathrm{mod-d}}^{\mathrm{multi}}, \end{aligned} \tag{4.1}$$

for the multi-current scheme, and

$$\begin{aligned} Y_{\mathrm{o-d}}^{\mathrm{AD-single}} &= Y_{\mathrm{o-d}} - \frac{G_{\mathrm{delay}} G_{\mathrm{AD}} G_{\mathrm{co-d}} G_{\mathrm{oL-d}}}{1 + G_{\mathrm{delay}} G_{\mathrm{AD}} G_{\mathrm{cL-d}}} \\ &= Y_{\mathrm{o-d}} - \frac{L_{\mathrm{AD-d}}^{\mathrm{single}}}{1 + L_{\mathrm{AD-d}}^{\mathrm{single}}} \frac{G_{\mathrm{co-d}} G_{\mathrm{oL-d}}}{G_{\mathrm{cL-d}}} \\ &= Y_{\mathrm{o-d}} - G_{\mathrm{mod-d}}^{\mathrm{single}}, \end{aligned} \tag{4.2}$$

for the single-current-feedback scheme. Note that $L_{\mathrm{AD-d}}^{\mathrm{multi/single}}/(1 + L_{\mathrm{AD-d}}^{\mathrm{multi/single}}) \approx 1$ within the active-damping-loop bandwidth, where the active-damping-affected multi and single-current-feedback scheme output admittances are changed by the corresponding modifier terms, i.e., $G_{\mathrm{co-d}} \left(G_{\mathrm{oL-d}} - Y_{\mathrm{o-d}}\right)/(G_{\mathrm{cL-d}} - G_{\mathrm{co-d}})$ and $G_{\mathrm{co-d}} G_{\mathrm{oL-d}}/G_{\mathrm{cL-d}}$, respectively.

Figs. 4.11 and 4.12 illustrate the frequency-domain behavior of different components in (4.1) and (4.2), respectively. The open-loop output admittance is the same with both multi and single-current-feedback active damping schemes. However, the modifier part $G_{\mathrm{mod-d}}^{\mathrm{multi/single}}$ changes significantly, which yields different active-damping-affected open-loop characteristics of the output admittances.

Considering the multi-current-feedback active damping scheme, in order to properly damp the resonance and induce deviations to the nominal open-loop dynamics, $|G_{\mathrm{mod-d}}^{\mathrm{multi}}| \approx |Y_{\mathrm{o-d}}|$ and $\theta_1 - \theta_2 \approx 180^{\mathrm{o}}$. In Fig. 4.11 the modifier magnitude is relatively small compared to the open-loop output admittance ($|G_{\mathrm{mod-d}}^{\mathrm{multi}}| \ll |Y_{\mathrm{o-d}}|$) when $f < 1000$ Hz and, therefore, the active-damping-affected output admittance exhibits similar characteristics with the nominal open-loop output admittance. However, $|G_{\mathrm{mod-d}}^{\mathrm{multi}}| \approx |Y_{\mathrm{o-d}}|$ when $600 < f < 3000$ Hz, which induces the damping effect seen in the active-damping-affected output admittance

The single-current-feedback scheme, on the other hand, imposes quite different characteristics on the output admittance. As evident from Fig. 4.12, the behavior of the modifier part is different from the multi-current-feedback counterpart. This can be explained by considering the modifier term in (4.2) and the control-loop-like structure discussed in Section 3.3. Accordingly, the active-damping loop has high gain also at lower frequencies, which changes the modifier term in (4.2). The nominal open-loop output admittance and the modifier have nearly the same gain, i.e., $|G_{\mathrm{mod-d}}^{\mathrm{single}}| \approx |Y_{\mathrm{o-d}}|$ with $\theta_1 - \theta_2 \approx 180^{\mathrm{o}}$ for a wide frequency range ($10 < f < 700$ Hz). Therefore, the active-damping-affected output admittance exhibits low and nearly constant gain in the corresponding frequency range, and the magnitude maintains its steady-state value ($\hat{i}_{\mathrm{od}}/\hat{u}_{\mathrm{od}} \approx I_{\mathrm{od}}/U_{\mathrm{od}}$) inside the active-damping loop.

The resonant-frequency gain difference in the output admittance between the multi and single-current-feedback schemes can be explained by analyzing Fig. 4.13. The magnitude of the modifier term $|G_{\mathrm{mod-d}}^{\mathrm{multi}}|$ equals to the magnitude of the open-loop output admittance as $|G_{\mathrm{mod-d}}^{\mathrm{multi}}| \approx |Y_{\mathrm{o-d}}|$ and $\theta_1 - \theta_2 \approx 180^{\mathrm{o}}$ in vicinity of the resonant frequency. Thus, the resonant behavior is effectively damped. Moreover, the gain of the modifier term in case of the multi-current-feedback scheme damps the LCL-filter resonance for a wider frequency range compared to the single-current-feedback counterpart as $\Delta(|G_{\mathrm{mod-d}}^{\mathrm{multi}}| - |G_{\mathrm{mod-d}}^{\mathrm{single}}|) \approx 20$ dB when $f > f_{\mathrm{res}}$. Therefore, the multi-current-feedback scheme induces increased damping on the resonant-frequency magnitude of the output admittance as can be observed from Fig. 4.14. Considering the single-current-feedback counterpart, the phase difference between the open-loop admittance and the modifier term deviates from 180 degrees causing decreased damping of the resonance.

For demonstrative purposes, Fig. 4.14 shows the active-damping-affected open-loop output admittances in case of proportional multi-current-feedback, proportional single-current-feedback and HPF single-current-feedback active damping schemes. As observable, the proportional multi-current-feedback scheme resembles the HPF single-current-feedback scheme due to similarities in the active damping loop gain. Conversely, the single-current-feedback scheme induces significantly different admittance properties within the corresponding active-damping-loop bandwidth. This yields to decreased admittance

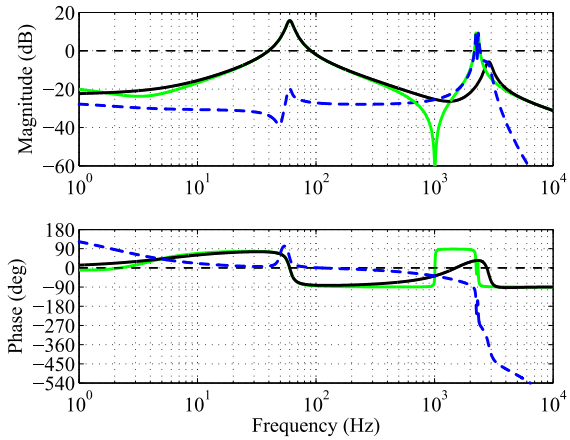

Fig. 4.11: Active-damping-affected output admittance (solid black line), nominal open-loop output admittance (solid green line) and modifier transfer function (dashed blue line) in case of multi-current-feedback scheme.

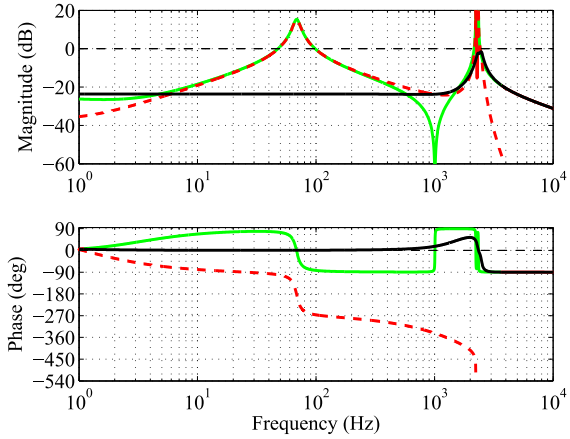

Fig. 4.12: Active-damping-affected output admittance (solid black line), nominal open-loop output admittance (solid green line) and modifier transfer function (dashed red line) in case of single-current-feedback scheme.

magnitude (or increased impedance) for $10 < f < 800$ Hz (see Fig. 4.15). Accordingly, the current control bandwidth is limited to $400 - 500$ Hz. Beyond the current-control bandwidth, open-loop dynamics begin to determine the shape of the output admittance.

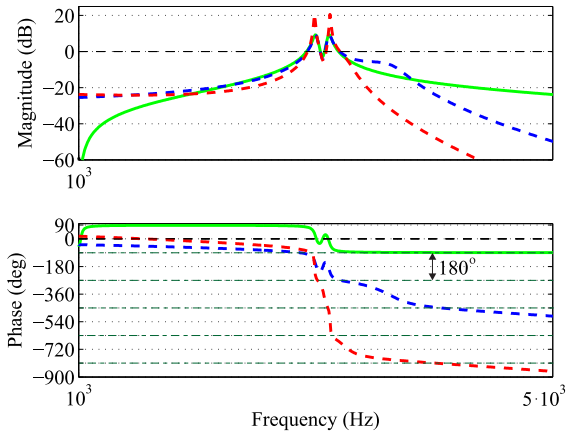

Fig. 4.13: Enlarged depiction of the modifier terms in case of multi-current-feedback scheme (dashed blue line), single-current-feedback scheme (dashed red line) and nominal open-loop output admittance (solid green line). Note that the phase of the nominal transfer function (green line) is shifted +360°.

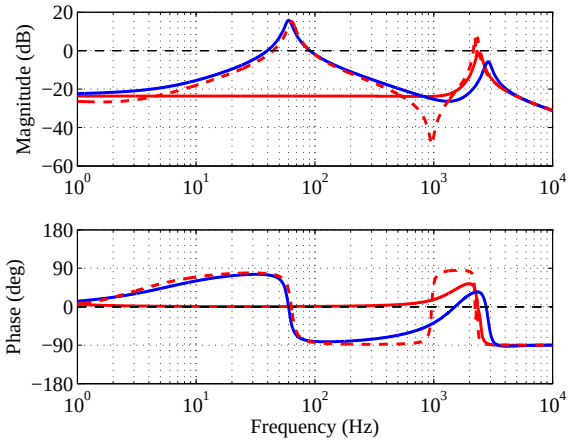

Fig. 4.14: Active-damping-affected output admittances in case of multi-current-feedback scheme (solid blue line), single-current-feedback scheme with proportional AD feedback (solid red line) and single-current-feedback scheme with HPF AD (dashed red line).

4.2.2 Passivity of output admittance

As shown in Section 4.1.2, the single-current-feedback active damping scheme induces passive high-frequency characteristics in the output impedance even when $f_{\mathrm{res}} > f_{\mathrm{s}}/6$. This imposes a major advantage compared with the multi-current-feedback scheme as the sensitivity to impedance-based instability is decreased. The explanation for such

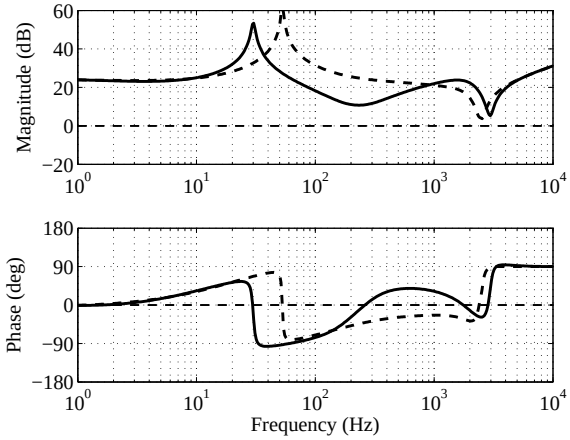

Fig. 4.15: Closed-loop output impedances in case of multi-current-feedback scheme (solid line) and single-current-feedback scheme with proportional AD (dashed line).

behavior lies in the active-damping-affected open-loop output admittance. Accordingly, the active-damping-affected output admittances in (3.22) and (3.35) are sums of the nominal open-loop output admittance and the active-damping-induced modifier part as shown in (4.1) and (4.2), respectively. The nominal open-loop output admittance $Y_{\mathrm{o-d}}$ is inherently passive regardless of the sampling frequency as it is determined only by the operating point and passive power-stage components, i.e., $\mathrm{Re}\{Y_{\mathrm{o-d}}\} \geq 0$. Therefore, it can be assumed that the modifier parts $G_{\mathrm{mod-d}}^{\mathrm{multi}}$ or $G_{\mathrm{mod-d}}^{\mathrm{single}}$ may induce the observed non-passivity. Considering Section 3.1.2, the delay term changes its sign depending on the operating conditions and, therefore, the modifier transfer functions may vary and induce the non-passive behavior. Similar observations are shown in [51, 61], where the behavior of the delay was noticed to induce the active-type impedance via the current control loop.

Fig. 4.16a shows the behavior of the real part in the active-damping-affected output admittance when the multi-current-feedback active damping scheme is used under $f_{\mathrm{res}} < f_{\mathrm{s}}/6$ and $f_{\mathrm{s}}/6 < f_{\mathrm{res}} < f_{\mathrm{s}}/3$. The real parts are similar when $f < 500$ Hz, but a negative real part is evident when $500 < f < 2000$ Hz if $f_{\mathrm{s}}/6 < f_{\mathrm{res}} < f_{\mathrm{s}}/3$, which indicates non-passive admittance characteristics in the active-damping-affected open-loop output admittance. If the non-passive behavior cannot be eliminated by the current control design, it also persists in the closed-loop output admittance characteristics.

The output admittance under single-current-feedback active damping scheme is shown in Fig. 4.16b for both $f_{\mathrm{res}} < f_{\mathrm{s}}/6$ and $f_{\mathrm{s}}/6 < f_{\mathrm{res}} < f_{\mathrm{s}}/3$. Evidently, the real part does not go below zero in the frequency range of 500−2000 Hz when $f_{\mathrm{s}}/6 < f_{\mathrm{res}} < f_{\mathrm{s}}/3$, contrary to the multi-current-feedback counterpart. Thus, the phase of the output

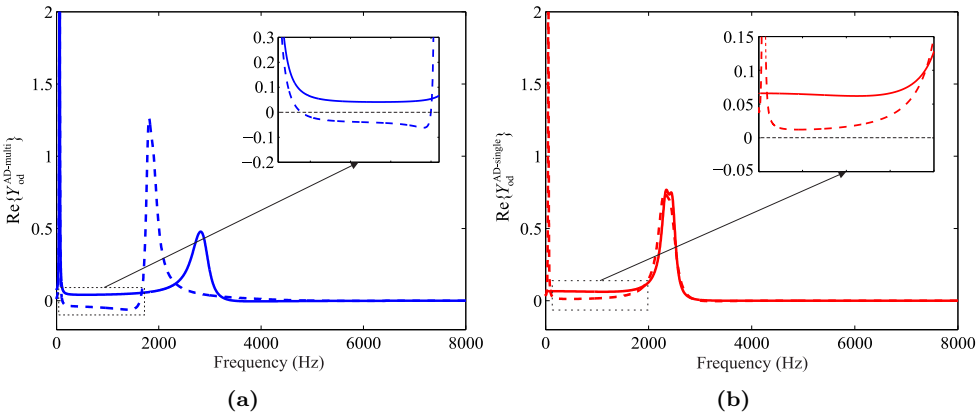

Fig. 4.16: Real part of the active-damping-affected output admittance when $f_{\mathrm{res}} < f_{\mathrm{s}}/6$ (solid line) and $f_{\mathrm{s}}/6 < f_{\mathrm{res}} < f_{\mathrm{s}}/3$ (dashed line) in (a) multi-current-feedback active damping scheme and (b) single-current-feedback active damping scheme.

admittance exhibits passive characteristics.

Considering both the multi and single-current-feedback schemes, the corresponding admittance properties can be explained by analyzing the active-damping-modifier terms in (4.1) and (4.2). The real parts of the modifiers are shown for both the aforementioned active damping schemes in Figs. 4.18a and 4.18b, respectively. In Fig. 4.18a, as the $\mathrm{Re}\{Y_{\mathrm{od}}\} \geq 0$ in the nominal open-loop output admittance (cf. Fig. 4.17), the modifier term imposes the observed negative real part when $500 < f < 2000$ Hz as $\mathrm{Re}\{G_{\mathrm{mod-d}}^{\mathrm{multi}}\} \leq 0$. On the contrary, the output admittance under single-current-feedback scheme exhibits positive real part between when $500 < f < 2000$ Hz. Accordingly, the real part in the modifier term is different compared with the multi-current-feedback scheme since the sign of the active damping gain is not changed. Thus, in both frequency regions of $f_{\mathrm{res}} < f_{\mathrm{s}}/6$ and $f_{\mathrm{s}}/6 < f_{\mathrm{res}} < f_{\mathrm{s}}/3$, the modifier has a positive real part, which affects the active-damping-affected output admittance, because $\mathrm{Re}\{Y_{\mathrm{od}}\} \geq 0$ and $\mathrm{Re}\{G_{\mathrm{mod-d}}^{\mathrm{single}}\} \geq 0$ in the aforementioned frequency range. Therefore, the active-type behavior of the output admittance is absent.

4.3 Conclusions

The single-current-feedback active damping scheme may clearly yield higher impedance below the resonant frequency compared with the multi-current scheme, which would attenuate the most common grid voltage harmonics (i.e., the 3$^{\mathrm{rd}}$, 5$^{\mathrm{th}}$, and 7$^{\mathrm{th}}$ harmonic) more efficiently. However, according to the stability analysis of the single-current scheme, the stability margins are inferior especially when $f_{\mathrm{res}} > f_{\mathrm{s}}/6$. Furthermore, the magnitude of the impedance in vicinity of the resonant frequency does not necessarily reach

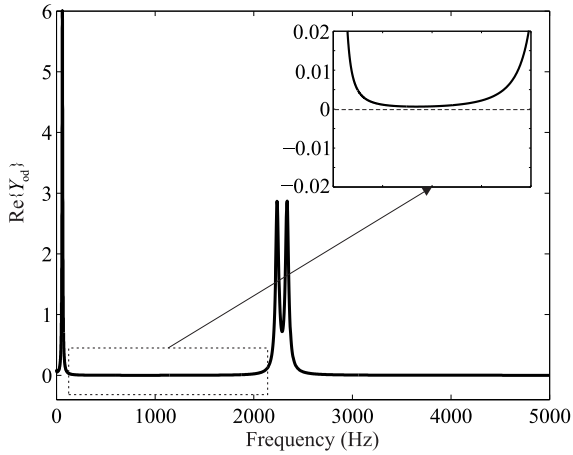

Fig. 4.17: Real part of the nominal open-loop output admittance.

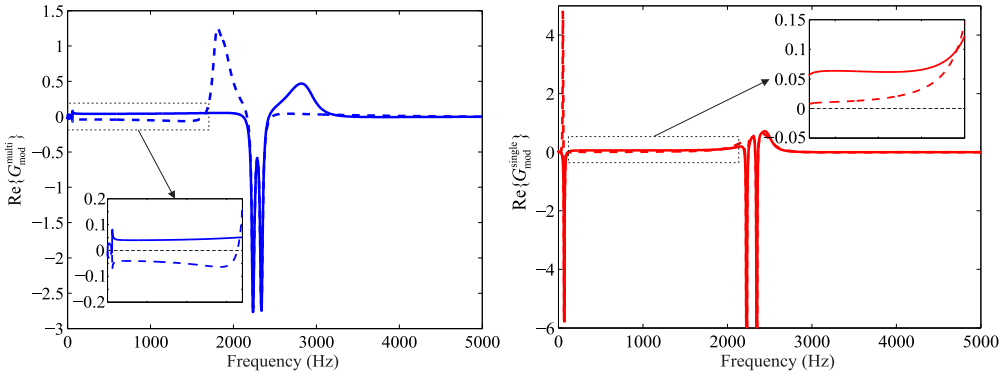

Fig. 4.18: Real part of the modifier term when $f_{res} < f_s/6$ (solid line) and $f_s/6 < f_{res} < f_s/3$ (dashed line) in (a) multi-current-feedback active damping scheme and (b) single-current-feedback active damping scheme.

the same level as with the multi-current-feedback scheme. Even though the low frequency impedance might be higher, the voltage harmonics may be transferred into the grid current via the resonant frequency impedance. Actually, as discussed in the previous section, the main advantages of the single-current feedback scheme are reduced costs and the passivity of the impedance, which is obtained even for $f_{res} > f_s/6$. This significantly decreases the risk for the impedance-based instability in all operating conditions of the converter. Hence, the single-current method may be used if the system costs are to be reduced and robustness regarding the impedance-based stability is required. Considering the low impedance at the resonant frequency, it would inevitably lead to operating constraints of the corresponding converter as the real grid may contain significant amount of

voltage harmonics especially in multi-parallel inverter systems [47, 58]. Thus, the multi-current scheme is better in terms of the mitigation capability of harmonic voltages as well as internal system stability, which was shown in the root trajectory analysis in Section 3.5. Furthermore, the real capacitor-current is measured, which allows more robust operation, when $f_{\mathrm{res}} > f_{\mathrm{s}}/6$.

5 EXPERIMENTAL RESULTS

This chapter provides the experimental measurements in order to verify the accuracy of the derived small-signal models, the root locus analyses, and the output-impedance properties. Accordingly, both the simulated and measured transfer functions are presented regarding the open and closed-loop models in Chapter 2 as well as the impedance analysis in Chapter 4. The internal stability of the converter regarding the root trajectories in Section 3.5 is verified with time-domain measurements. The impedance-based interactions are demonstrated as well.

The measurement setup, shown in Fig. 5.1, was used in the experimental tests. Photovoltaic (PV) simulator PVS7000 and three-phase grid-emulator PAS15000 manufactured by Spitzenberger & Spies are used as an input source and load, respectively. The three-phase grid-connected inverter is implemented on the SiC-based inverter bridge MWINV-1044-SIC manufactured by MyWay. Converter control was implemented by using a dSPACE DS1103 platform. Furthermore, the output impedance was measured with the corresponding platform by using pseudo-random binary sequence (PRBS) method [87]. Note that simulated frequency responses were also obtained by using the PRBS technique implemented in MATLAB with Simscape Power Systems tools.

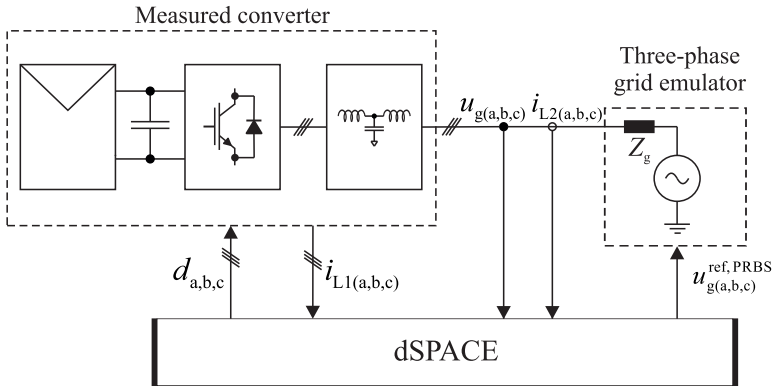

Fig. 5.1: Overview of the measurement setup.

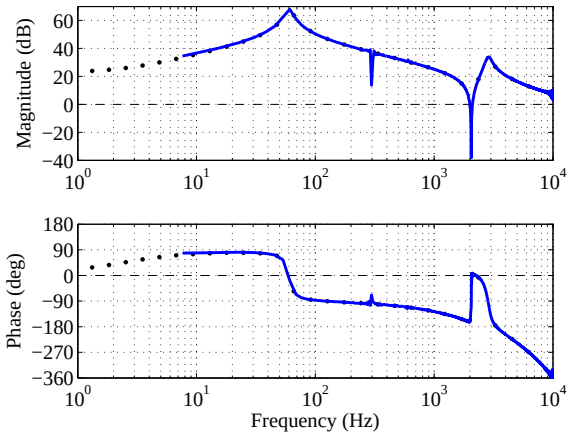

Fig. 5.2: Simulated (solid line) and modeled (dotted line) open-loop control-to-inductor-current $G_{\text{cL-d}}$ response in case of multi-current-feedback active damping.

5.1 Open-loop verifications

The open-loop dynamics are verified by simulations with MATLAB, which is an efficient way to verify the open-loop models. The validity of the open-loop transfer functions is important since the analysis in this thesis is based on the active-damping-affected open-loop dynamics. A PRBS method is utilized to extract the frequency responses from the time-domain simulation model. These open-loop simulations verify the models derived in Chapters 2 and 3. The parameters used in the simulations are found in Table 3.1, which are used also for the experimental measurements of the prototype inverter.

As discussed earlier, the open-loop control-to-inductor-current transfer function and the output admittance are analyzed here. The former is used in the closed-loop control design and the latter in the specific active damping analysis. Fig. 5.2 shows the predicted and simulated active-damping-affected control-to-inductor-current transfer function in case of the multi-current-feedback active damping scheme. Furthermore, the corresponding frequency responses in case of the single-current-feedback scheme are shown in Fig. 5.3. The simulated and predicted frequency responses match well in both cases, and the differences between the two schemes are clearly visible.

As discussed in Chapter 3, the open-loop output admittance changes significantly depending on the active damping implementation. Accordingly, the single-current-feedback active damping scheme induces control-loop-like properties and, therefore, the output admittance was observed to exhibit significantly lower magnitude below the resonant frequency. This observation is visible also in the simulations, which are presented in case of both the multi and single-current-feedback schemes in Figs. 5.4 and 5.5, respectively.

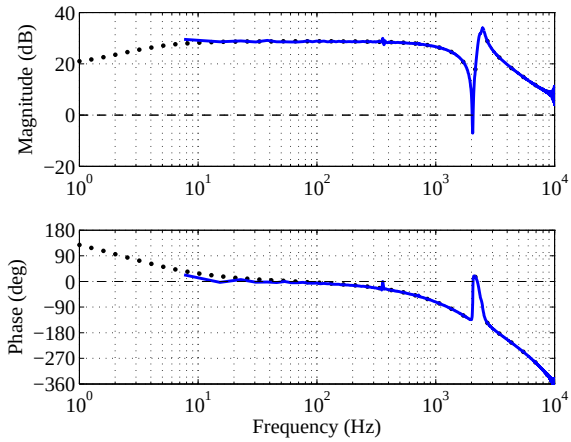

Fig. 5.3: Simulated (solid line) and modeled (dotted line) open-loop control-to-inductor-current $G_{\text{cL-d}}$ response in case of single-current-feedback active damping.

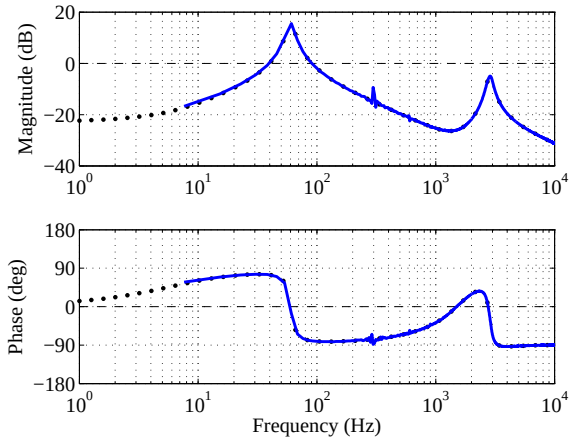

Fig. 5.4: Simulated (solid line) and modeled (dotted line) open-loop output admittance $Y_{\text{o-d}}$ in case of multi-current-feedback active damping.

Clearly, the simulated frequency responses match well with the analytical models.

5.2 Closed-loop verifications

Closed-loop verifications validate the obtained closed-loop impedance model as well as the control and active damping designs. The DC-link voltage control loop is verified by means of MATLAB simulation and the output impedance is measured with a prototype inverter. As the closed-loop output impedance is affected by both the output-current and DC-link voltage-control designs, the validity of the closed-loop model can be determined

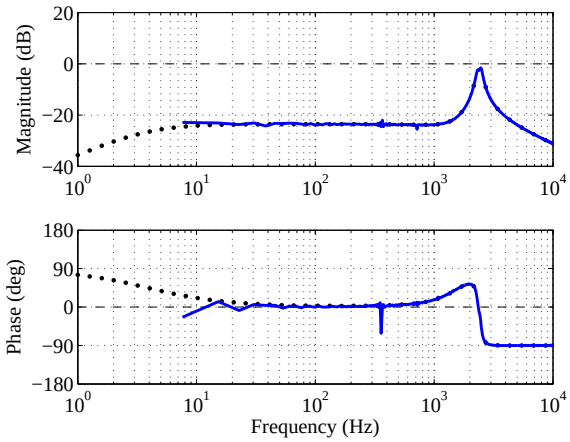

Fig. 5.5: Simulated (solid line) and modeled (dotted line) open-loop output admittance $Y_{\text{o-d}}$ in case of single-current-feedback active damping.

by the impedance measurements.

5.2.1 Input-voltage control design

The input-voltage control should be designed properly due to inherent constraints caused by the used topology, which introduces an RHP pole into the control dynamics, when operating in the CCR. Regarding the control engineering principles, the crossover frequency of the control loop shall be higher than the RHP-pole frequency, which is $\omega_{\text{pole}} = I_{\text{in}}/C_{\text{in}}U_{\text{in}} \approx 12.3$ rad/s. Furthermore, the maximum limit for the crossover frequency is imposed by the 100 Hz DC-link voltage ripple caused by an unbalanced grid. Sufficient attenuation should be provided in order to avoid the pollution of the grid current reference.

The method to verify the DC-link control loop is shown in Fig. 5.6. A sinusoidal injection is provided to the input voltage reference signal, and the error signal as well as the input voltage are measured. Thus, the voltage control loop is determined according to corresponding figure as $\mathbf{L}_{\text{in}} = \mathbf{G}_{\text{ci}}^{\text{out}}\mathbf{G}_{\text{vc}}$. Fig. 5.7 shows the simulated input-voltage loop gain, where the desired 20 dB attenuation at 100 Hz is nearly obtained. Furthermore, the gain and phase margins are 60 dB and 89 degrees, respectively, indicating good stability margins. Moreover, difference between the simulated and predicted loop gains is negligible, thus, the control design can be assumed to be accurate.

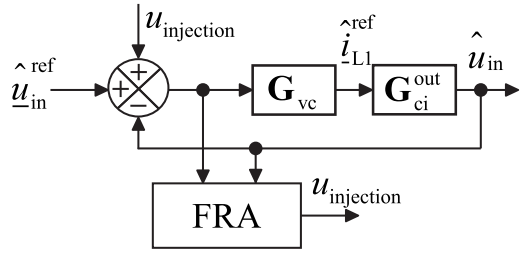

Fig. 5.6: Methodology for the input voltage loop gain measurement.

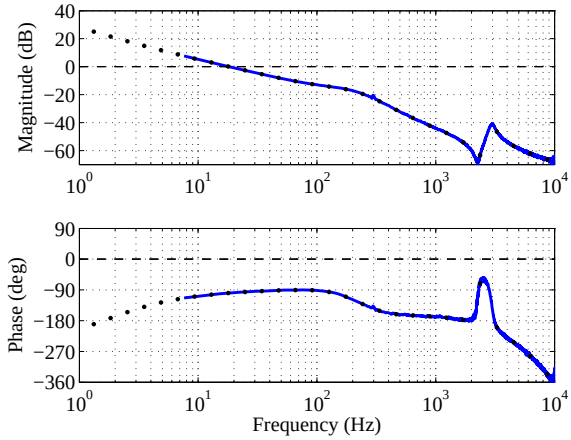

Fig. 5.7: Simulated (solid line) and modeled (dotted line) input-voltage loop gain.

5.2.2 Output impedance verification

This section presents the output impedance measurements from the prototype inverter. The corresponding measurement setup is shown in Fig. C.1 in Appendix B. Considering both the multi and single-current-feedback schemes, different active damping feedback implementations are verified according to the analyses shown in Sections 3.5 and 3.1.2 under operating conditions of $f_{\text{res}} < f_{\text{s}}/6$, $f_{\text{s}}/6 < f_{\text{res}} < f_{\text{s}}/3$ and $f_{\text{s}}/3 < f_{\text{res}} < f_{\text{s}}/2$.

Multi-current-feedback scheme

Fig. 5.8 shows the measured d and q-components of the output impedance, when $f_{\text{res}} < f_{\text{s}}/6$ with proportional active damping feedback ($R_{\text{d}} = 10\ \Omega$). As can be seen, the active-type impedance is visible in the q-component at low frequencies as the phase is close to -180 degrees, which is caused by the PLL [66]. The impedance magnitude in vicinity of the resonant frequency is around 5 dB, which might be insufficient since 5 dB $\approx 1.8\ \Omega$. That is, a voltage harmonic at the corresponding frequency with only 1.8 V amplitude

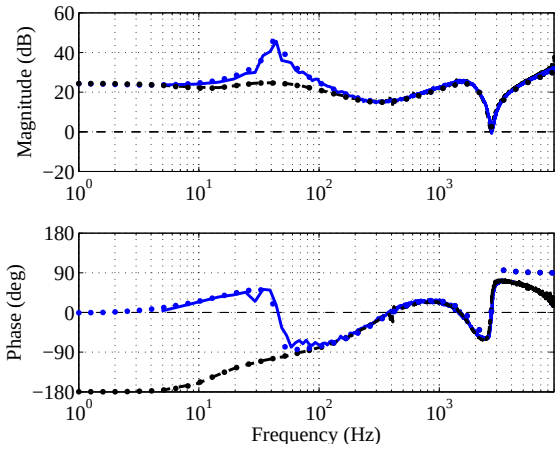

Fig. 5.8: Modeled (dotted lines) and measured d and q-components (blue line and black dashed line) of the output impedance in case of proportional active damping feedback, $R_\mathrm{d} = 10\ \Omega$.

would yield a harmonic current response of 1 A. Regarding the operating point, the corresponding grid current is around 10 A and, therefore, the harmonic current would be 10 % of the nominal current.

The robustness of the converter can be improved for $f_\mathrm{res} < f_\mathrm{s}/6$ by using a high-pass-filtered active damping feedback according to the analysis in Section 3.5. As shown earlier in both the root locus and impedance analyses, the HPF induces more damped transient response and higher output impedance magnitude. Accordingly, Fig. 5.9 shows the output impedance for the corresponding case with $R_\mathrm{d} = 10\ \Omega$ and $\omega_\mathrm{cutoff} = \omega_\mathrm{res}$. Comparing Figs. 5.8 and 5.9, the magnitude at the resonant frequency is increased from 5 dB to around 15 dB $\approx 5.6\ \Omega$ by using the HPF active damping and, therefore, significantly larger voltage harmonic at the resonant frequency would be required to induce the same 1 A harmonic current as in Fig. 5.8.

When the sampling frequency changes as $f_\mathrm{s}/6 < f_\mathrm{res} < f_\mathrm{s}/3$, significant changes occur in the output impedance. The phase begins to resemble active-type impedance (i.e., non-passive) around the resonant frequency, which is harmful for the overall system stability. This can be seen in Fig. 5.10, which shows the output impedance for proportional active damping feedback with $R_\mathrm{d} = -10\ \Omega$.

Considering Section 3.5, a low-pass filter is recommended for improving the system stability, when the converter is operating under $f_\mathrm{s}/6 < f_\mathrm{res} < f_\mathrm{s}/3$. Comparing the root trajectories in Figs. 3.19a and 3.20b, it is evident that such filter induces beneficial properties in the current-control dynamics. Correspondingly, the low-pass-filtered active damping feedback improves the output impedance characteristics as shown in Fig. 5.11 with $R_\mathrm{d} = -15\ \Omega$. Clearly, the resonant behavior is effectively reduced as the magnitude

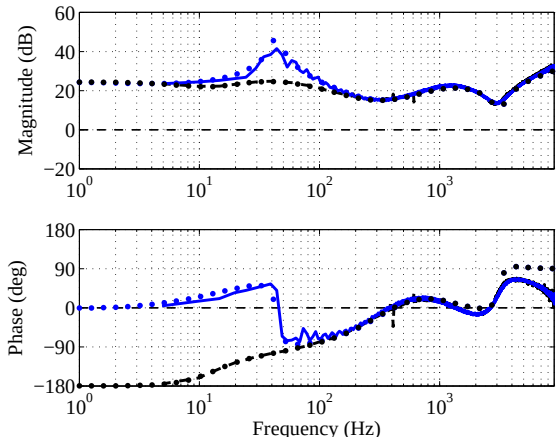

Fig. 5.9: Modeled (dotted lines) and measured d and q-components (blue line and black dashed line) of the output impedance in case of HPF active damping feedback, $R_\mathrm{d} = 10\ \Omega$, $\omega_\mathrm{cutoff} = \omega_\mathrm{res}$.

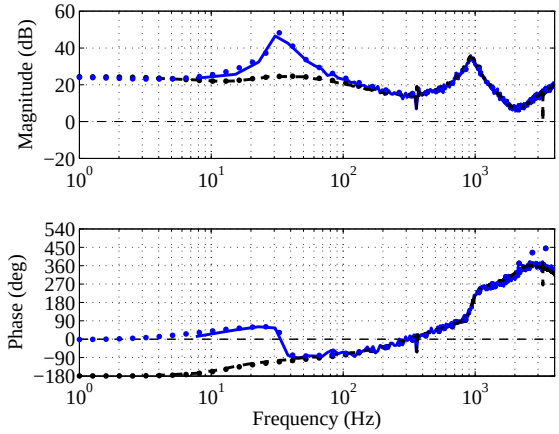

Fig. 5.10: Modeled (dotted lines) and measured d and q-components (blue line and black dashed line) of the output impedance in case of proportional active damping feedback, $R_\mathrm{d} = -10\ \Omega$.

of the output impedance ($\approx$ 15 dB) only slightly varies within the frequency range of $1-3$ kHz. Hence, the grid-voltage harmonics do not affect the grid current significantly in the given frequency range compared to the case of proportional feedback in Fig. 5.10.

By further changing the sampling frequency as $f_\mathrm{s}/3 < f_\mathrm{res} < f_\mathrm{s}/2$, a high-pass filter is recommended to improve the system stability as well as the output impedance properties. Fig. 5.12 shows the output impedance with high-pass-filtered active damping ($R_\mathrm{d} = -15$, $\omega_\mathrm{cutoff} = 0.5\omega_\mathrm{res}$). As can be observed, the output impedance exhibits similar characteristics as in case of Fig. 5.11, since the magnitude stays relatively constant in

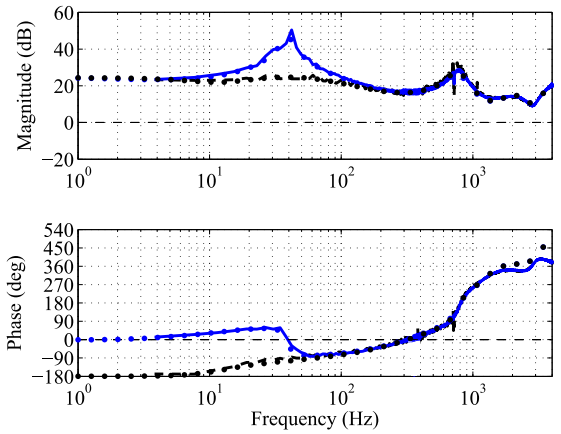

Fig. 5.11: Modeled (dotted lines) and measured d and q-components (blue line and black dashed line) of the output impedance in case of LPF active damping feedback, $R_\mathrm{d} = -15\ \Omega$, $\omega_\mathrm{cutoff} = \omega_\mathrm{res}$.

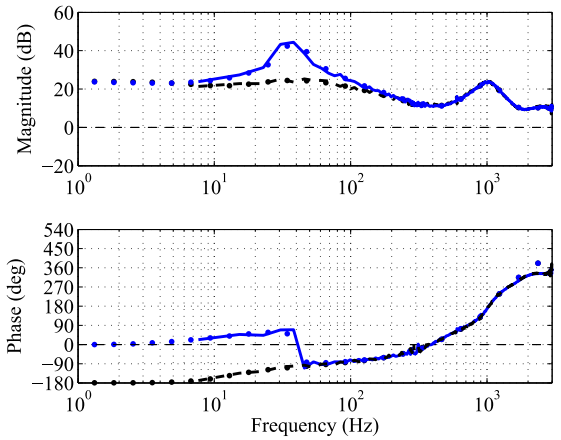

Fig. 5.12: Modeled (dotted lines) and measured d and q-components (blue line and black dashed line) of the output impedance in case of HPF active damping feedback, $R_\mathrm{d} = -15\ \Omega$, $\omega_\mathrm{cutoff} = 0.5\omega_\mathrm{res}$.

a wide frequency range. Clearly, the resonant behavior is effectively reduced, and the magnitude of the output impedance is sufficiently high (≈ 10 dB).

Considering the measurements presented in this section, the derived model is accurate and predicts the resonant-frequency-impedance behavior well. This is important as the active damping affects only in vicinity of the resonant frequency, which can be accurately analyzed using the derived model.

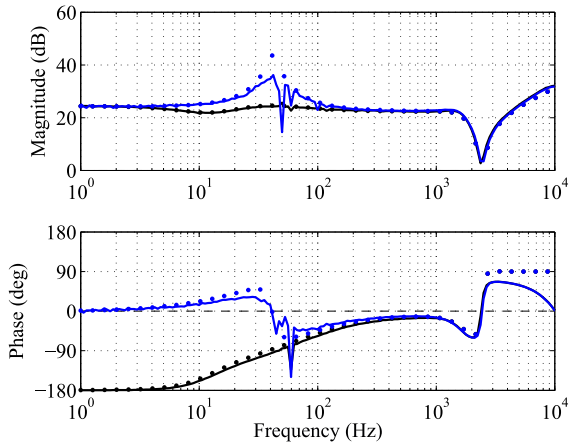

Fig. 5.13: Modeled (dotted lines) and measured d and q-components (blue line and black dashed line) of the output impedance in case of single-current-feedback active damping , $R_\mathrm{d} = 10\ \Omega$.

Single-current-feedback scheme

Regarding the inherent operating constraints discussed in Section 3.5.3 in case of the single-current-feedback active damping scheme, the output impedance is verified with proportional and HPF active damping for $f_\mathrm{res} < f_\mathrm{s}/6$ and with HPF active damping for $f_\mathrm{s}/6 < f_\mathrm{res} < f_\mathrm{s}/3$. Fig. 5.13 shows the output impedance in case of proportional active damping with $R_\mathrm{d} = 10\ \Omega$, when the converter operates under $f_\mathrm{res} < f_\mathrm{s}/6$. Evidently, the magnitude of the output impedance in the frequency range of $100 - 1000$ Hz is higher compared to the multi-current-feedback counterpart in Fig. 5.8. This property is beneficial as the common grid-voltage harmonics are the 3^rd, 5^th and 7^th harmonics. In case of the aforementioned frequencies, the output impedance in the demonstrated case is always higher than 20 dB, which effectively prevents the voltage harmonics from polluting the grid current.

Considering the filtered active damping feedback implementation, Fig. 5.14 shows the output impedance in case of high-pass-filtered active damping with $R_\mathrm{d} = 15\ \Omega$ and $\omega_\mathrm{cutoff} = 3\omega_\mathrm{res}$. Clearly, the shape of the output impedance is similar to Fig. 5.8, since the HPF single-current-feedback active damping resembles the proportional multi-current-feedback method. Accordingly, a decrease in the magnitude is observable in the frequency range of $100-1000$ Hz, which is peculiar in the multi-current-feedback schemes due to the lower open-loop output admittance. Referring to the measured impedances in Figs. 5.13 and 5.14, the analysis shown in Section 4.2 regarding the behavior of the single-current-feedback active damping and its effect on the system transfer functions is accurate.

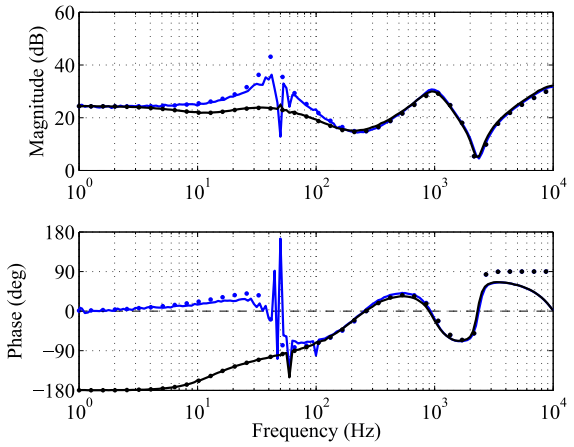

Fig. 5.14: Modeled (dotted lines) and measured d and q-components (blue line and black dashed line) of the output impedance in case of single-current-feedback HPF active damping , $R_\mathrm{d} = 15\ \Omega$, $\omega_\mathrm{cutoff} = 3\omega_\mathrm{res}$.

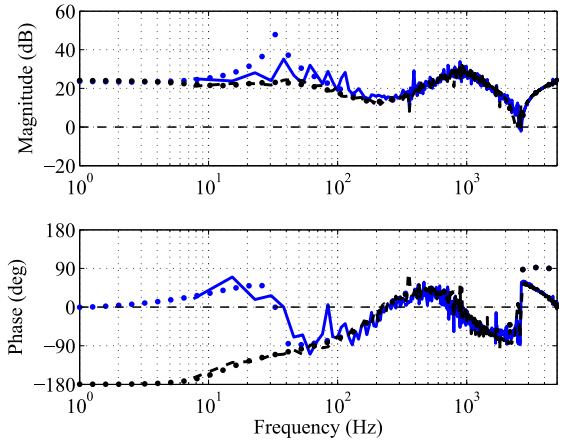

Fig. 5.15: Modeled (dotted lines) and measured d and q-components (blue line and black dashed line) of the output impedance in case of single-current-feedback HPF active damping , $R_\mathrm{d} = 55\ \Omega$, $\omega_\mathrm{cutoff} = 3.5\omega_\mathrm{res}$.

As discussed in Section 3.5, the measured inverter current must be high-pass filtered, when operating under $f_\mathrm{s}/6 < f_\mathrm{res} < f_\mathrm{s}/3$ in order to eliminate the low frequency gain and to induce phase boost in the active damping loop. Accordingly, Fig. 5.15 shows the output impedance in case of HPF AD when $R_\mathrm{d} = 55$ and $\omega_\mathrm{cutoff} = 3\omega_\mathrm{res}$. Significant distortions are visible in the measured impedance as the internal stability of the converter is weak according to the root locus analysis of the corresponding case in Fig.

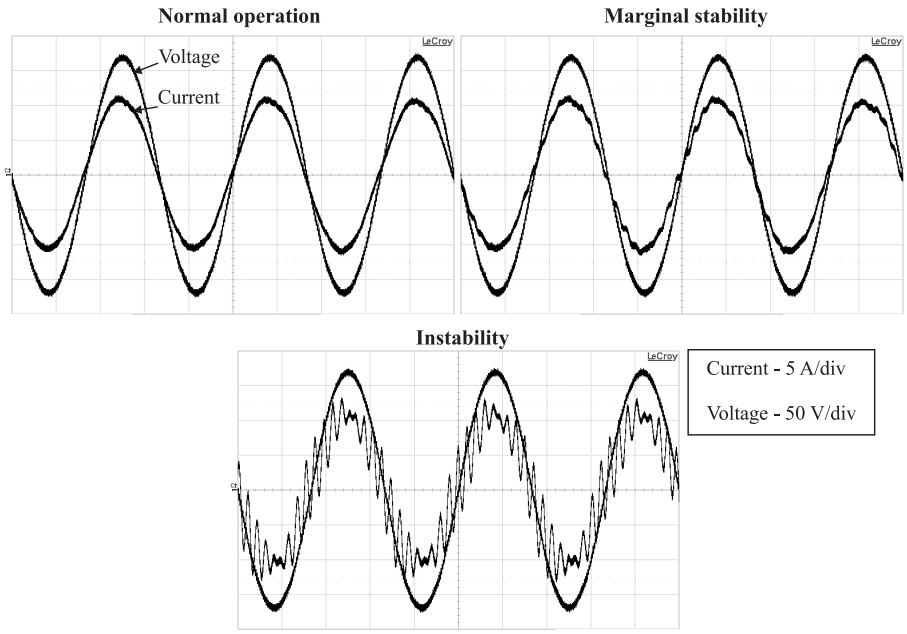

Fig. 5.16: Measured phase voltage and current during normal operation (top left), marginal stability (top right) and instability (bottom).

3.27a. Accordingly, the roots stay near the imaginary axis regardless of the feedback gain indicating poor stability characteristics of the output-current control. Therefore, the measured impedance is distorted. However, the measured impedances clearly follow the predictions regardless of the distortions.

5.2.3 Stability of the active damping loop

The location of the roots in the current-control dynamics determines the system stability, that is, whether the roots lie in the left-half plane or the right-half plane and how far they are from the real and imaginary axes. Considering the root loci presented in Section 3.5, the validity of the results should be addressed in order to justify their utilization in the active damping design. Accordingly, two different cases are shortly analyzed here in order to present the accuracy of the root loci in determining the control-system stability.

In Fig. 5.16, the active-damping stability is analyzed in case of the proportional capacitor-current feedback in the naturally stable resonant frequency region of $f_{\mathrm{res}} < f_{\mathrm{s}}/6$. The system stability is determined by the corresponding root locus shown in Fig. 3.18a. Accordingly, the active damping gain is first set to $R_{\mathrm{d}} = 10\ \Omega$, which yields stable current-control dynamics. The virtual resistor value is then changed to $R_{\mathrm{d}} = 27$

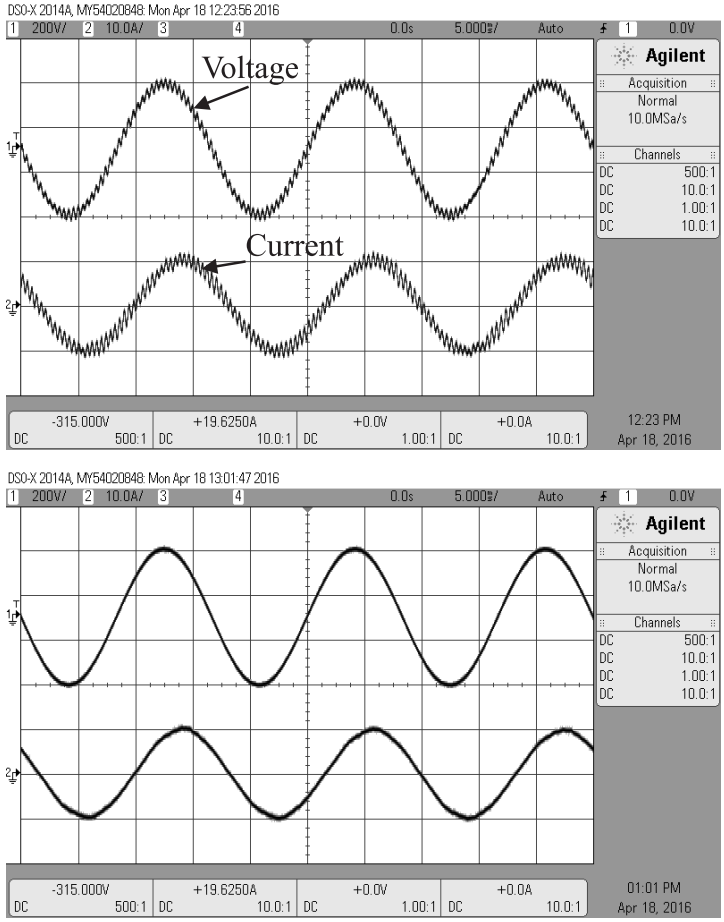

Fig. 5.17: Measured phase voltage and current during unstable operation without HPF (top) and under nominal operation with HPF (bottom).

Ω, where the system is marginally stable referring to the root trajectory in Fig. 3.18a. Clearly, the output current becomes slightly distorted (cf. Fig. 5.16 top right figure). By setting $R_\mathrm{d} = 29\ \Omega$, the roots cross the imaginary axis to the RHP causing unstable current dynamics as is evident in the bottom figure in Fig. 5.16.

The high-pass filter improves the system stability characteristics and allows selecting the virtual resistor value for wider range compared to the pure proportional active-damping-feedback implementation. This is demonstrated in Fig. 5.17 in case of the single-current-feedback scheme when $f_\mathrm{res} < f_\mathrm{s}/6$. The root loci regarding the stability analysis are shown in Figs. 3.26a and 3.26b. The pure proportional feedback is demonstrated first, and the virtual resistor value is first set to $R_\mathrm{d} = 41\ \Omega$, which places the control-system poles to the RHP yielding unstable operation as visible in the top figure in

Fig. 5.17. However, by activating the high-pass filter, the roots with the aforementioned active damping gain move back into the LHP, which stabilizes the system. Considering the root locus analysis, it can be concluded that the aforementioned root loci predict accurately the overall control system stability and, thus, they can be used to determine the suitable active-damping-feedback gain.

5.3 Impedance-based analysis

This section demonstrates the impedance-based interactions affecting the stable operation of grid-connected converters. Accordingly, both the effect of the grid background harmonics and the impedance-based instability are presented. The Nyquist stability criterion is an essential tool in the analyzing stability of interconnected systems and, therefore, it is briefly discussed next in order to elaborate the matter. The stability criterion is demonstrated later in order to validate its usefulness.

5.3.1 Nyquist stability criterion

In grid-connected applications, the utility grid regulates the voltage seen by the converter, thus the grid voltage acts as a disturbance element from the system point-of-view. Accordingly, the converter controls its output current with high bandwidth, and is considered, in the small-signal analysis, as a constant current source feeding the grid. The interconnection can be represented as a small-signal impedance model as shown in Fig. 5.18a. The grid voltage should not affect the output current, which maintains its value regardless of the voltage and, therefore, the current source should exhibit ideally infinite parallel output impedance. In practical applications, this is not true as the converter has a finite output impedance dictated by the control dynamics and the filter parameters. As shown earlier, the output impedance can exhibit very low magnitude around the resonant frequency, which impairs its ideal properties.

The ideal grid, on the other hand, should have a zero series impedance in order to decouple the grid from the converter. However, the real grid contains a finite series input impedance exhibiting mostly inductive properties with various resonances [45, 46]. Therefore, the voltage at the PCC (cf. Fig. 5.18a) is affected by the injected grid current as $\hat{\underline{u}}_{\mathrm{PCC}} = \mathbf{Z}_{\mathrm{g}}\hat{\underline{i}}_{\mathrm{L2}} + \hat{\underline{u}}_{\mathrm{o}}$ and, thus, the grid and the converter are considered to be coupled and susceptible to interactions.

Based on the small-signal equivalent circuit shown in Fig. 5.18a, the output current vector $\hat{\underline{i}}_{\mathrm{L2}}$ can be given as in (5.1).

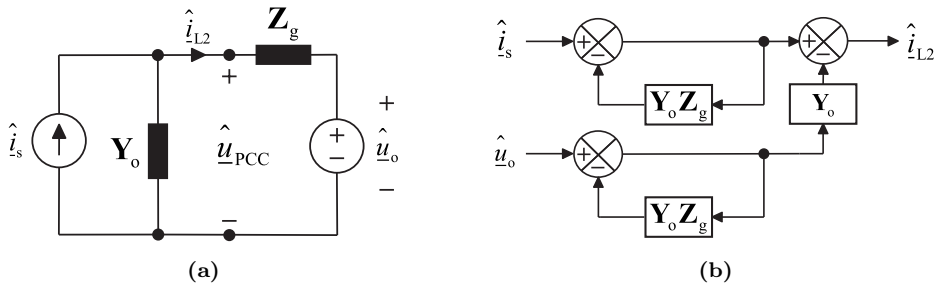

Fig. 5.18: (a) Small-signal representation of the grid interface and (b) its equivalent control block-diagram.

$$\begin{aligned}
\hat{\underline{i}}_{L2} &= \hat{\underline{i}}_s - \mathbf{Y}_o\hat{\underline{u}}_{PCC}, \quad \hat{\underline{u}}_{PCC} = \hat{\underline{u}}_o + \mathbf{Z}_g\hat{\underline{i}}_{L2} \\
\hat{\underline{i}}_{L2} &= \hat{\underline{i}}_s - \mathbf{Y}_o\left[\hat{\underline{u}}_o + \mathbf{Z}_g\hat{\underline{i}}_{L2}\right] \\
\hat{\underline{i}}_{L2} &= [\mathbf{I} + \mathbf{Y}_o\mathbf{Z}_g]^{-1}\hat{\underline{i}}_s - [\mathbf{I} + \mathbf{Y}_o\mathbf{Z}_g]^{-1}\mathbf{Y}_o\hat{\underline{u}}_o
\end{aligned} \tag{5.1}$$

It can be seen from (5.1) that the grid current is dependent on the source current (affected by the control dynamics) and the grid voltage. The interconnection imposes a loop structure, which affects the behavior and stability of the grid current as demonstrated in Fig. 5.18b.

The stability can be evaluated by applying the generalized Nyquist stability criterion to the return-ratio matrix $\mathbf{Y}_o\mathbf{Z}_g$ [88]. If the cross-couplings are neglected as they usually are small in magnitude, since no reactive power is produced, the direct and quadrature components of the impedances suffice for the analysis separately and are considered decoupled. That is, the stability of the *d*-component can be analyzed with the *inverse* minor loop gain $L_{\text{minor-dd}} = Y_{o-dd}Z_{g-dd}$ and the *q*-component by $L_{\text{minor-qq}} = Y_{o-qq}Z_{g-qq}$. Considering Fig. 5.18b and the basic control engineering principles, the stability of the loop is guaranteed if the converter output impedance is higher than the grid impedance as then $|Z_g|/|Z_o| < 1$, which would ensure the stability of the corresponding minor loop gain. Moreover, an ideal grid with zero series impedance would guarantee the stability of the minor loop gain as well.

The real grid often exhibits inductive characteristics especially at higher frequencies [46] and, thus the grid impedance may exceed the converter output impedance yielding $|Z_g|/|Z_o| > 1$. The aforementioned case would make the converter susceptible to impedance-based instability if the converter output impedance loses its passive characteristics and the phase difference of $Z_{g\text{-}qq}$ and $Z_{o\text{-}qq}$ exceeds 180 degrees. It has been already observed that the PLL causes active-type-impedance behavior at the low frequencies [52, 58, 64, 66, 68]. Such phase behavior can exist also at higher frequencies, in

certain conditions, due to the current controller [51] and the active damping, which may easily introduce high-frequency impedance-based instability.

5.3.2 Impedance-based instability and background harmonics

Regarding the factors affecting the stable operation of a grid-connected converter, active-type output impedance increases significantly the impedance-based-instability sensitivity of the grid-connected converter. Furthermore, in a grid-feeding converter, low output impedance at the resonant frequency enables the grid voltage harmonics to interact with the converter causing harmonic currents proportional to the impedance magnitude at the corresponding frequency. These two factors may degrade the power quality, because the grid current may get excessively polluted as observed, e.g., in [49]. Therefore, it should be ensured that the output impedance of the converter exhibits passive properties and the magnitude is as high as possible. Accordingly, it is important to address the aforementioned risks as a part of the active damping design as its effect on the output impedance is significant. In order to emphasize the importance of aforementioned factors, this section will verify the power quality issues induced by the impedance-based instability and the grid background harmonics.

Considering the impedance-based stability, active-type output impedance is analyzed in this case, where the sampling frequency is restricted as $f_{\text{res}} > f_{\text{s}}/6$. As discussed in Section 5.3.1, a finite series grid impedance is required for interactions. Thus, a high impedance grid (i.e., a weak grid) is analyzed here, which is determined by the short-circuit-ratio (SCR) or the X/R-ratio, where SCR$<$ 3 or $X/R < 5$. The weak grid is demonstrated with the resistive and inductive values of $R = 0.5\ \Omega$ and $L = 1$ mH, respectively, yielding $X/R = 0.63$.

Fig. 5.19 shows the Bode plots of the grid impedance $Z_{\text{g-dd}}$ and the active-type output impedance Z_{odd} with LPF AD, which refer to the case shown in Fig. 4.5. Moreover, the Nyquist plot of the impedance ratio $Z_{\text{g-dd}}/Z_{\text{o-dd}}$ is shown in the same figure. The d and q-component impedances are assumed to be decoupled and, thus, the generalized Nyquist stability criterion (GNC) is not required. In Fig. 5.19, the Nyquist plot encircles the $(-1, 0)$-point when the virtual resistor value is decreased from $R_{\text{d}} = -18\ \Omega$ to $R_{\text{d}} = -21\ \Omega$ indicating unstable behavior. The same phenomenon can be intuitively seen from the Bode plots as the phase difference between $Z_{\text{g-dd}}$ and $Z_{\text{o-dd}}$ exceeds 180^{o} when $|Z_{\text{g-dd}}| > |Z_{\text{o-dd}}|$ leading to instability. Regarding the impedance-based instability, Fig. 5.20 shows the measured output current under the violation of the Nyquist stability criterion. Accordingly, the output current begins to oscillate at the frequency of the violation, i.e., $f_{\text{harmonic}} \approx 1500$ Hz. As the high-frequency oscillations have been reported from industrial photovoltaic generators [49], active damping design may have important contribution regarding the mitigation of such harmonic oscillations and instability.

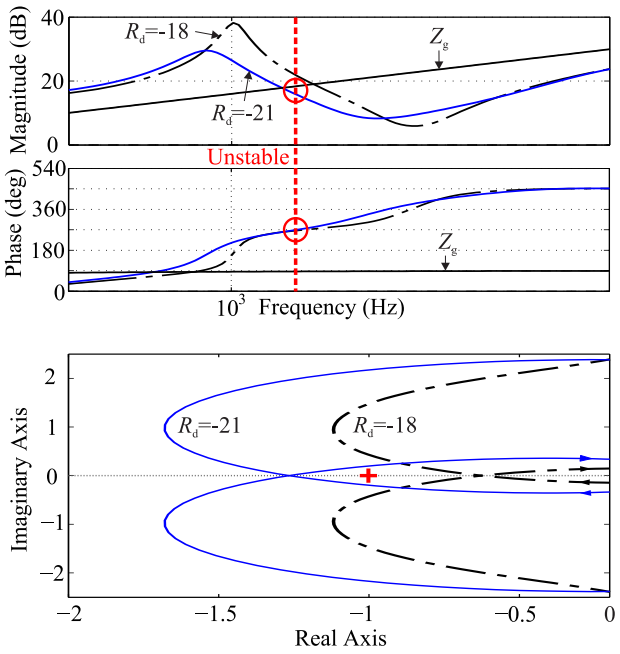

Fig. 5.19: Bode plots (upper figure) for $Z_{\text{odd}}, Z_{\text{g}}$ and Nyquist diagram (lower figure) for the ratio of $Z_{\text{g}}/Z_{\text{odd}}$, $f_{\text{res}} > f_{\text{s}}/6$.

The solar panels in photovoltaic power stations are not necessarily connected to a single high-power central inverter. In fact, medium-power inverters are usually connected in parallel (string inverters) to address the situations caused, e.g., by partial shading conditions. In these multi-parallel inverter systems, the voltage of the point-of-common-coupling (PCC) can be distorted due to resonant interaction between converters [18]. Thus, the PCC voltage may contain elevated harmonics near the LCL-filter resonant frequency. This can cause oscillations in the grid current if the output impedance of the inverter is relatively low compared to the magnitude of the oscillation. Furthermore, the harmonic oscillation in the grid current will eventually increase the harmonic pollution in the grid voltage due to the coupling with the grid impedance, which, in turn, will circulate and increase the overall harmonic currents. Active damping should be, therefore, designed to achieve as high output impedance as possible in order to prevent the grid voltage harmonics from exciting the resonances.

The harmonic rejection capability of the converter can be analyzed by imposing a high-frequency component in the grid voltage. In this setup, a harmonic voltage with 5 V amplitude and $f_{\text{harmonic}} = 1378$ Hz was produced by the grid emulator, which represents a grid with elevated harmonic content. In the measurements, the output impedance magnitude of the converter is modified by adjusting the active damping gain

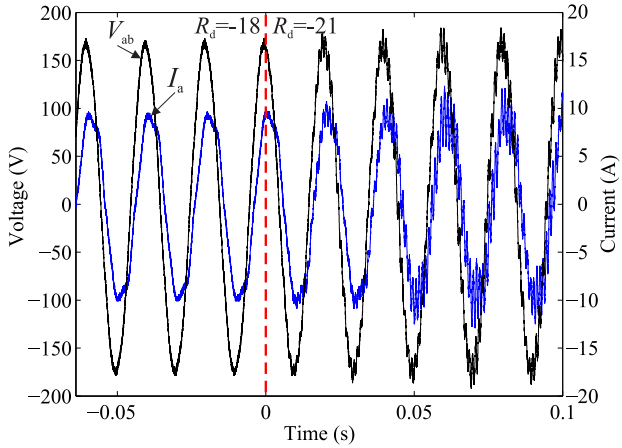

Fig. 5.20: Measured phase to phase voltage V_{ab} and phase current I_a with high-frequency impedance-based instability due to violation of Nyquist stability criterion in Fig. 5.19.

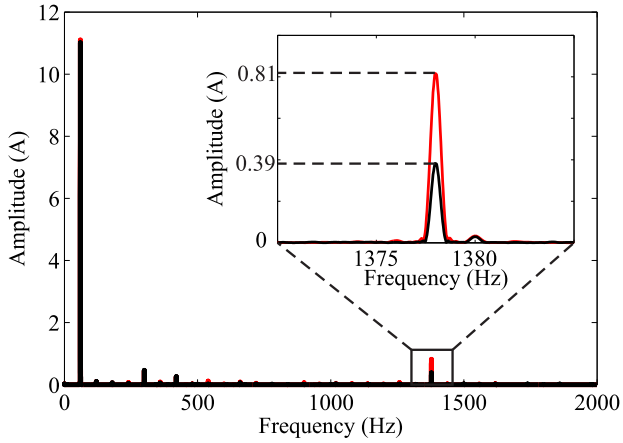

Fig. 5.21: Grid-current spectrum under influence of grid background harmonics with low impedance (red line) and high impedance (black line).

in order to present two different cases. Accordingly, the lowest magnitude of the output impedance is set to 10 dB $\approx$ 3.2 Ω and the highest to 18 dB $\approx$ 7.9 Ω, representing a case with proportional active damping feedback when $f_{res} > f_s/6$ (cf. Fig. 4.3). The grid-current spectrum was measured for both impedance levels, which are shown in Fig. 5.21. Evidently, the grid-voltage harmonic causes a large harmonic current if the impedance is low, which in practical applications may cause, e.g., shutdown of the photovoltaic inverters due to high harmonic content. Moreover, the transformers may get damaged by the high-frequency currents flowing through the capacitively coupled parts. However, by increasing the output impedance, the amplitude of the harmonic

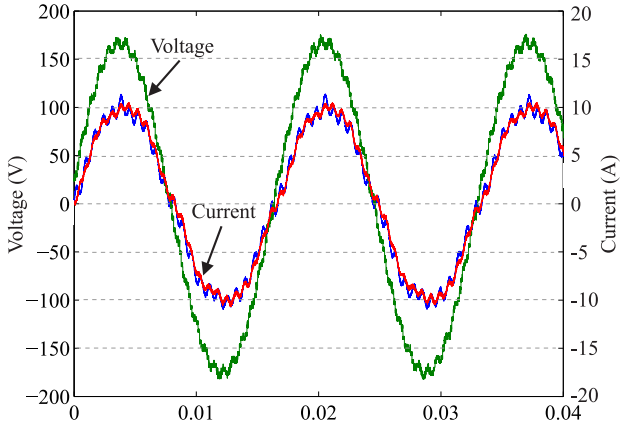

Fig. 5.22: Grid-current waveform under influence of grid background harmonics with low impedance (blue line) and high impedance (red line).

current can be effectively decreased to around half of the original current. Time-domain measurements of the corresponding case are shown in Fig. 5.22. Clearly, active damping can be designed to provide sufficient impedance level and, therefore, the susceptibility to the grid background harmonics is decreased.

6 CONCLUSIONS

This chapter presents the final conclusions regarding the thesis as well as the interesting future research topics.

6.1 Final conclusions

Photovoltaic generator is a power-limited non-ideal current source and, thus, it imposes peculiar design constraints on the interfacing power-electronic-based converters. Three different operating regions, which characterize the internal dynamic of the PV cell, can be identified as the constant-current region, constant-voltage region and the maximum power point. These have to be considered in the analysis when deriving mathematical models for switched-mode power converters as well as in the control system design. This guarantees stable operation of the converter in varying operating conditions.

Multi-variable small-signal modeling was extensively applied in this thesis in order to produce a comprehensible mathematical model for a three-phase grid-connected converter. The modeling requires identification of the system input and output variables, which subsequently affect the analysis profoundly. Therefore, it is important to assess the dynamics of the interfaced source and load systems accurately as well. In case of grid-connected photovoltaic inverter, the PV generator has to be considered as a current source from the dynamic point-of-view due to its internal characteristics. Furthermore, the load is the utility grid, which is considered as a rigid voltage source since it dictates the voltage and frequency seen by the converter. These factors impose restrictions for the possible controlled variables of the system. That is, the converter controls its own input voltage in order to achieve maximum power delivery into the grid. Furthermore, the converter controls its output current, which is synchronized with the grid by means of the PLL. Therefore, the converter is analyzed as a current-fed-current-output system.

LCL-filter is an effective and cost-efficient way in attenuating the switching frequency harmonics and is, therefore, widely used in practical applications. However, the inductors and capacitance create resonant circuits causing ideally infinite or zero impedances at certain frequencies. Accordingly, these resonances appear in the control dynamics, which must be damped in order to achieve stable operation of the converter. Passive damping method is a robust and simple way to damp the resonances, which is performed by inserting a resistor usually in series with the filter capacitor. However, this will introduce

additional power losses for up to 1 % and weaken the attenuation capability of the LCL-filter. Therefore, different active damping techniques are used, which rely on modifying the inverter control signal in order to produce the desired damping effect without any physical components. It is shown in this thesis that both the multi and single-current-feedback active damping schemes provide sufficient performance regarding the system stability and impedance characteristics.

The stability of the control system regarding the active damping design was assessed with root locus diagrams. Corresponding ICF converters lack the explicit active damping design rules and, therefore, the aforementioned root locus plots were used to determine the system stability. Furthermore, the root trajectories were subsequently used to analyze their correspondence with the output impedance characteristics. Considering the active damping design, the inherent properties of the delay were analyzed carefully as it imposes major design constraints. Accordingly, it was observed that a low-pass filter is beneficial when $f_s/6 < f_{res} < f_s/3$ and, on the contrary, a high-pass filter is recommended when $f_s/3 < f_{res} < f_s/2$ and $f_{res} < f_s/6$ for improved stability characteristics. Generally, the root locus analysis proposes that the roots should be placed as far from the imaginary-axis as possible if high output impedance magnitude is desired. Moreover, in order to improve the current control characteristics and stability, filtered active damping feedbacks are recommended to be used.

As discussed in this thesis, active damping has a significant effect on the output impedance of the converter. The output impedance determines the converter sensitivity to external interactions and is, therefore, the key factor affecting the stability of the grid interface. Active damping, when poorly designed, can easily compromise the stable operation of the converter or impair the impedance characteristics. This is manifested as extremely low magnitude in the impedance and active-type (i.e., negative real part) phase behavior. However, by accurately considering the inherent properties of active damping, such as delay dependency, the impedance characteristics as well as the converter stability can be greatly improved. The stability of the grid interface can be intuitively assessed by analyzing the frequency-domain output impedance predictions, which, on the other hand, dictate the allowed grid impedance required for stable operation. With accurate output impedance models, the risk for instability can be deterministically analyzed, thus decreasing the risk for impedance-based interactions. Furthermore, the output impedance can be used to assess the susceptibility for grid-voltage harmonics especially in vicinity of the LCL-filter resonant frequencies.

To conclude, this thesis analyzed the effect of the active damping on system dynamics and, especially, on the output impedance. Multi-variable small-signal modeling was utilized in order to simplify the derivation of the model. This modeling technique allows insertion of different control loops and their analysis easily. Moreover, the effect of dif-

ferent active damping feedbacks was addressed and the design guidelines regarding the selection of correct feedback technique were presented. Accordingly, improved output impedance characteristics can be achieved by using correct active damping design.

6.2 Future research topics

This thesis presented an accurate small-signal model of three-phase grid-connected inverter and its impedance properties. The effect of active damping on the system dynamics was analyzed. However, some aspects may not have been addressed thoroughly and some topics may need further research. Below are listed observations regarding the possible and interesting future research topics:

- As the HPF and LPF affect significantly the stability of the converter and the shape of the output impedance, explicit parametric design rules should be presented for these filters. Accordingly, design criteria could be used to guarantee optimized impedance properties for all operating conditions, i.e. $f_{\mathrm{res}} < f_{\mathrm{s}}/6$ and $f_{\mathrm{res}} > f_{\mathrm{s}}/6$. However, due to the complexity of the small-signal modeling, explicit design criteria may be hard to realize.
- In case of the single-current-feedback converter operating under $f_{\mathrm{res}} > f_{\mathrm{s}}/6$, it should be analyzed whether the HPF is the best solution in providing suitable stability and output impedance properties. For example, band-pass filters have been used for ICF converters successfully in some cases and, therefore, additional design criteria would be appreciated.
- Considering significant delay-induced constraints and differences for ICF and GCF converters, it would be interesting to analyze and compare the active damping on both converter control topologies regarding the output impedance. Accordingly, it would be interesting to analyze whether one topology would be superior to another.
- The low-frequency phase flip in the d-component of the output impedance over 180 degrees is caused by the input voltage control loop and should be studied. This behavior may impose a risk for low-frequency impedance-based instability and should be, therefore, analyzed. It was observed that the phase flip is related to the phase margin of the input voltage control loop, but its detailed analysis was omitted from this thesis.
- Active damping for a grid-feeding inverter was analyzed here. However, when islanded, the converter operates in a grid-forming mode, which leads to a different topology and modeling details as the grid-side inductor is 'omitted' in the analysis. Thus, resonances in the system dynamics will change. It would be interesting to compare active damping and output impedance characteristics of both grid-feeding and grid-forming converters as well.

REFERENCES

[1] B. K. Bose, "Energy, environmental pollution, and the impact of power electronics," *IEEE Ind. Electron. Mag.*, pp. 6–17, Mar. 2010.

[2] "Roadmap 2050: a practical guide to a prosperous, low-carbon europe," European Climate Foundation (ECF), Tech. Rep., Apr. 2010.

[3] S. Valkealahti, "Forecasting the future of renewables," in *Climate Change-Socioeconomic Effects, In Tech*, Sep.. 2010, pp. 425–440.

[4] L. Nousiainen, J. Puukko, A. Maki, T. Messo, J. Huusari, J. Jokipii, J. Viinamaki, D. T. Lobera, S. Valkealahti, and T. Suntio, "Photovoltaic generator as an input source for power electronic converters," *IEEE Trans. Power Electron.*, vol. 28, no. 6, pp. 3028–3038, Jun. 2013.

[5] L. Nousiainen, J. Puukko, and T. Suntio, "Appearance of a RHP-zero in VSI-based photovoltaic converter control dynamics," in *IEEE INTELEC'11*, Oct. 2011, pp. 1–8.

[6] T. Messo, J. Jokipii, J. Puukko, and T. Suntio, "Determining the value of DC-link capacitance to ensure stable operation of a three-phase photovoltaic inverter," *IEEE Trans. Power Electron.*, vol. 29, no. 2, pp. 665–673, Feb. 2014.

[7] J. Kivimaki, S. Kolesnik, M. Sitbon, T. Suntio, and A. Kuperman, "Design guidelines for multi-loop perturbative maximum power point tracking algorithms," *IEEE Trans. Power Electron.*, vol. PP, no. 99, pp. 1–1, 2017.

[8] R. D. Middlebrook, "Small-signal modeling of pulse-width modulated switched-mode power converters," *Proceedings of the IEEE*, vol. 76, no. 4, pp. 343–354, Apr 1988.

[9] Y. Chen and F. Liu, "Design and control for three-phase grid-connected photovoltaic inverter with LCL filter," *IEEE Circuits and Systems International Conference on Testing and Diagnosis*, pp. 1–4, Apr. 2009.

[10] M. Liserre, R. Teodorescu, and F. Blaabjerg, "Stability of photovoltaic and wind turbine grid-connected inverters for a large set of grid impedance values," *IEEE Trans. Power Electron.*, vol. 21, no. 1, pp. 263–272, Jan. 2006.

[11] M. Shahparasti, M. Mohamadian, and A. Yazdian, "Derivation of a stationary-frame single-loop controller for three-phase standalone inverter supplying nonlinear loads," *IEEE Trans. Power Electron.*, vol. 29, no. 9, pp. 5063–5071, Sep. 2014.

[12] D. N. Zmood and D. G. Holmes, "Stationary frame current fegulation of PWM inverters with zero steady-state error," *IEEE Trans. Power Electron.*, vol. 18, no. 3, pp. 814–822, May 2003.

[13] Y. Jia, J. Zhao, and X. Fu, "Direct grid current control of LCL-filtered grid-connected inverter mitigating grid voltage disturbance," *IEEE Trans. Power Electron.*, vol. 29, no. 3, pp. 1532–1541, Mar. 2014.

[14] S. Jayalath and M. Hanif, "Generalized LCL-filter design algorithm for grid-connected voltage-source inverter," *IEEE Trans. Ind. Electron.*, vol. 64, no. 3, pp. 1905–1915, Mar. 2017.

[15] M. Liserre, F. Blaabjerg, and S. Hansen, "Design and control of an LCL-filter-based three-phase active rectifier," *IEEE Trans. Ind. Appl.*, vol. 41, no. 5, pp. 1281–1291, Sep. 2005.

[16] B. Ren, X. Sun, S. An, X. Cao, and Q. Zhang, "Analysis and design of an LCL filter for the three-level grid-connected inverter," *IEEE IPEMC'12*, pp. 2023–2027, Jun. 2012.

[17] C. Bao, X. Ruan, X. Wang, and W. Li, "Step-by-step controller design for LCL-type grid-connected inverter with capacitor-current-feedback active-damping," *IEEE Trans. Power Electron.*, vol. 29, no. 3, pp. 1239–1253, Mar. 2014.

[18] J. L. Agorreta, M. Borrega, J. López, and L. Marroyo, "Modeling and control of N-paralleled grid-connected inverters with LCL filter coupled due to grid impedance in pv plants," *IEEE Trans. Power Electron.*, vol. 26, no. 3, pp. 770–785, Mar. 2011.

[19] S. Arcuri, M. Liserre, D. Ricchiuto, T. Kerekes, and F. Blaabjerg, "Stability analysis of grid inverter LCL-filter resonance in wind or photovoltaic parks," in *IEEE IECON'11*, Nov. 2011, pp. 2499–2504.

[20] E. Twining and D. G. Holmes, "Grid current regulation of a three-phase voltage source inverter with an LCL input filter," *IEEE Trans. Power Electron.*, vol. 18, no. 3, pp. 888–895, May 2003.

[21] V. Blasko and V. Kaura, "A novel control to actively damp resonance in input LC filter of a three-phase voltage source converter," *IEEE Trans. Ind. Appl.*, vol. 33, no. 2, pp. 542–550, Mar. 1997.

[22] P. Dahono, Y. Bahar, Y. Sato, and T. Kataoka, "Damping of transient oscillations on the output LC filter of PWM inverters by using a virtual resistor," in *Proc. IEEE 4th Int. Conf. on Power Electron. and Drive Syst.*, 2001, pp. 403–407.

[23] M. Liserre, A. Dell'Aquila, and F. Blaabjerg, "Genetic algorithm-based design of the active damping for an LCL-filter three-phase active rectifier," *IEEE Trans. Power Electron.*, vol. 19, no. 1, pp. 76–86, Jan. 2004.

[24] J. Dannehl, M. Liserre, and F. W. Fuchs, "Filter-based active damping of voltage source converters with lcl filter," *IEEE Trans. Ind. Electron.*, vol. 58, no. 8, pp. 3623–3633, Aug. 2011.

[25] M. Ciobotaru, A. Rosse, L. Bede, B. Karanayil, and V. G. Agelidis, "Adaptive notch filter based active damping for power converters using LCL filters," in *IEEE PEDG'16*, Jun. 2016, pp. 1–7.

[26] J. Dannehl, C. Wessels, and F. Fuchs, "Limitations of voltage-oriented PI current control of grid-connected PWM rectifiers with LCL filters," *IEEE Trans. Ind. Electron.*, vol. 56, no. 2, pp. 380–388, Feb. 2009.

[27] Y. W. Li, "Control and resonance damping of voltage-source and current-source converters with LC filters," *IEEE Trans. Ind. Electron.*, vol. 56, no. 5, pp. 1511–1521, May 2009.

[28] D. Pan, X. Ruan, C. Bao, W. Li, and X. Wang, "Optimized controller design for LCL-type grid-connected inverter to achieve high robustness against grid-impedance variation," *IEEE Trans. Ind. Electron.*, vol. 62, no. 3, pp. 1537–1547, Mar. 2014.

[29] D. Pan, S. Member, X. Ruan, S. Member, and C. Bao, "Capacitor-current-feedback active damping with reduced computation delay for improving robustness of LCL-type grid-connected inverter," *IEEE Trans. Power Electron.*, vol. 29, no. 7, pp. 3414–3427, Jul. 2014.

[30] X. Wang, C. Bao, X. Ruan, W. Li, and D. Pan, "Design considerations of digitally controlled LCL-filtered inverter with capacitor-current-feedback active damping," *IEEE Trans. Emerg. Sel. Topics Power Electron.*, vol. 2, no. 4, pp. 972–984, Dec. 2014.

[31] J. Dannehl, F. W. Fuchs, S. Hansen, and P. B. Thøgersen, "Investigation of active damping approaches for PI-based current control of grid-connected pulse width modulation converters with LCL filters," *IEEE Trans. Ind. Appl.*, vol. 46, no. 4, pp. 1509–1517, Jul. 2010.

[32] Y. Tang, P. C. Loh, P. Wang, F. H. Choo, and F. Gao, "Exploring inherent damping characteristic of LCL-filters for three-phase grid-connected voltage source inverters," *IEEE Trans. Power Electron.*, vol. 27, no. 3, pp. 1433–1443, Mar. 2012.

[33] S. G. Parker, B. P. McGrath, and D. G. Holmes, "Regions of active damping control for LCL filters," *IEEE Trans. Ind. Appl.*, vol. 50, no. 1, pp. 424–432, Jan. 2014.

[34] J. Wang, J. D. Yan, L. Jiang, and J. Zou, "Delay-dependent stability of single-loop controlled grid-connected inverters with LCL filters," *IEEE Trans. Power Electron.*, vol. 31, no. 1, pp. 743–757, Jan. 2016.

[35] X. Li, X. Wu, Y. Geng, X. Yuan, C. Xia, and X. Zhang, "Wide damping region for LCL-type grid-connected inverter with an improved capacitor-current-feedback method," *IEEE Trans. Power Electron.*, vol. 30, no. 9, pp. 5247–5259, Sep. 2015.

[36] X. Wang, F. Blaabjerg, and P. C. Loh, "Grid-current-feedback active damping for LCL resonance in grid-connected voltage source converters," *IEEE Trans. Power Electron.*, vol. 31, no. 1, pp. 213 – 223, Jan. 2015.

[37] S. G. Parker, B. P. McGrath, and D. G. Holmes, "Regions of active damping control for LCL filters," *IEEE Trans. Ind. Appl.*, vol. 50, no. 1, pp. 424–432, Jan. 2014.

[38] C. Bao, X. Ruan, X. Wang, W. Li, D. Pan, and K. Weng, "Step-by-step controller design for LCL-type grid-connected inverter with capacitor-current-feedback active-damping," *IEEE Trans. Power Electron.*, vol. 29, no. 3, pp. 1239–1253, Mar. 2014.

[39] C. Zou, B. Liu, S. Duan, and R. Li, "Influence of delay on system stability and delay optimization of grid-connected inverters with LCL filter," *IEEE Trans. Ind. Informat.*, vol. 10, no. 3, pp. 1775–1784, Aug. 2014.

[40] Y. Lyu, H. Lin, and Y. Cui, "Stability analysis of digitally controlled LCL-type grid-connected inverter considering the delay effect," *IET Power Electron.*, vol. 8, no. 9, pp. 1651–1660, Mar. 2015.

[41] J. Yin, S. Duan, and B. Liu, "Stability analysis of grid-connected inverter wth LCL filter adopting a digital single-loop controller with inherent damping characteristic," *IEEE Trans. Ind. Informat.*, vol. 9, no. 2, pp. 1104–1112, May 2013.

[42] X. Zhang, J. W. Spencer, and J. M. Guerrero, "Small-signal modeling of digitally controlled grid-connected inverters with LCL filters," *IEEE Trans. Ind. Electron.*, vol. 60, no. 9, pp. 3752–3765, Sep. 2013.

[43] J. Xu, S. Xie, J. Kan, and L. Ji, "An improved inverter-side current feedback control for grid-connected inverters with LCL filters," in *IEEE ICPE- ECCE'15 Asia*, 2015, pp. 984–989.

[44] J. Xu, S. Xie, and T. Tang, "Active damping-based control for grid-connected lcl -filtered inverter with injected grid current feedback only," *IEEE Trans. Ind. Electron.*, vol. 61, no. 9, pp. 4746–4758, Sep. 2014.

[45] S. Zhang, S. Jiang, X. Lu, B. Ge, and F. Z. Peng, "Resonance issues and damping techniques for grid-connected inverters with long transmission cable," *IEEE Trans. Power Electron.*, vol. 29, no. 1, pp. 110–120, Jan. 2014.

[46] L. Jessen and F. W. Fuchs, "Modeling of inverter output impedance for stability analysis in combination with measured grid impedances," in *IEEE PEDG'15*, Jun. 2015, pp. 1–7.

[47] J. He, Y. W. Li, D. Bosnjak, and B. Harris, "Investigation and active damping of multiple resonances in a parallel-inverter-based microgrid," *IEEE Trans. Power Electron.*, vol. 28, no. 1, pp. 234–246, Jan. 2013.

[48] M. Lu, X. Wang, P. C. Loh, and F. Blaabjerg, "Resonance interaction of multiparallel grid-connected inverters with lcl filter," *IEEE Trans. Power Electron.*, vol. 32, no. 2, pp. 894–899, Feb. 2017.

[49] C. Li, "Unstable operation of photovoltaic inverter from field experiences," *IEEE Trans. Power Del.*, vol. PP, no. 99, pp. 1–1, Early Access 2017.

[50] J. Sun, "Impedance-based stability criterion for grid-connected inverters," *IEEE Trans. Power Electron.*, vol. 26, no. 11, pp. 3075–3078, Nov. 2011.

[51] L. Harnefors, X. Wang, A. Yepes, and F. Blaabjerg, "Passivity-based stability assessment of grid-connected VSCs - An overview," *IEEE Trans. Emerg. Sel. Topics Power Electron.*, vol. 4, no. 1, pp. 116 – 125, Mar. 2016.

[52] B. Wen, D. Boroyevich, R. Burgos, P. Mattavelli, and Z. Shen, "Analysis of D-Q small-signal impedance of grid-tied inverters," *IEEE Trans. Power Electron.*, vol. 31, no. 1, pp. 675–687, Jan. 2016.

[53] X. Wu, X. Li, X. Yuan, and Y. Geng, "Grid harmonics suppression scheme for LCL-type grid-connected inverters based on output admittance revision," *IEEE Trans. Sustain. Energy*, vol. 6, no. 2, pp. 411–421, Apr. 2015.

[54] D. Yang, X. Ruan, and H. Wu, "Impedance shaping of the grid-connected inverter with LCL filter to improve its adaptability to the weak grid condition," *IEEE Trans. Power Electron.*, vol. 29, no. 11, pp. 5795–5805, Nov. 2014.

[55] X. Chen, Y. Zhang, S. Wang, J. Chen, and C. Gong, "Impedance-phased dynamic control method for grid-connected inverters in a weak grid," *IEEE Trans. Power Electron.*, vol. PP, no. 99, pp. 1–1, Early Access. 2016.

[56] M. Cespedes and J. Sun, "Impedance modeling and analysis of grid-connected voltage-source converters," *IEEE Trans. Power Electron.*, vol. 29, no. 3, pp. 1254–1261, Mar. 2014.

[57] Y. Yu, H. Li, and Z. Li, "Impedance modeling and stability analysis of lcl-type grid-connected inverters with different current sampling schemes," in *IEEE IPEMC-ECCE'16 Asia*, May 2016, pp. 974–981.

[58] Y. Wang, X. Chen, Y. Zhang, J. Chen, and C. Gong, "Impedance modeling of three-phase grid-connected inverters and analysis of interaction stability in grid-connected system," in *IEEE IPEMC-ECCE'16 Asia*, May 2016, pp. 3606–3612.

[59] Z. Liu, J. Liu, X. Hou, Q. Dou, D. Xue, and T. Liu, "Output impedance modeling and stability prediction of three-phase paralleled inverters with master-slave sharing scheme based on terminal characteristics of individual inverters," *IEEE Trans. Power Electron.*, vol. 31, no. 7, pp. 5306–5320, Jul. 2016.

[60] X. Wang, Y. W. Li, F. Blaabjerg, and P. C. Loh, "Virtual-impedance-based control for voltage-source and current-source converters," *IEEE Trans. Power Electron.*, vol. 30, no. 12, pp. 7019–7037, Dec. 2015.

[61] L. Harnefors, M. Bongiorno, and S. Lundberg, "Input-admittance calculation and shaping for controlled voltage-source converters," *IEEE Trans. Ind. Electron.*, vol. 54, no. 6, pp. 3323–3334, Dec 2007.

[62] Y. Song, X. Wang, and F. Blaabjerg, "Impedance-based high-frequency resonance analysis of dfig system in weak grids," *IEEE Trans. Power Electron.*, vol. 32, no. 5, pp. 3536–3548, May 2017.

[63] D. Yang, X. Ruan, and H. Wu, "Impedance shaping of the grid-connected inverter with LCL filter to improve its adaptability to the weak grid condition," *IEEE Trans. Power Electron.*, vol. 29, no. 11, pp. 5795–5805, Nov. 2014.

[64] B. Wen, D. Dong, D. Boroyevich, R. Burgos, P. Mattavelli, and Z. Shen, "Impedance-based analysis of grid-synchronization stability for three-phase paralleled converters," *IEEE Trans. Power Electron.*, vol. 31, no. 1, pp. 26–38, Jan. 2016.

[65] X. Wu, X. Li, X. Yuan, and Y. Geng, "Grid harmonics suppression scheme for LCL-type grid-connected inverters based on output admittance revision," *IEEE Trans. Sustain. Energy*, vol. 6, no. 2, pp. 411–421, Apr. 2015.

[66] T. Messo, J. Jokipii, A. Mäkinen, and T. Suntio, "Modeling the grid synchronization induced negative-resistor-like behavior in the output impedance of a three-phase photovoltaic inverter," in *IEEE PEDG'13*, Jul. 2013, pp. 1–7.

[67] K. M. Alawasa, Y. A. R. I. Mohamed, and W. Xu, "Active mitigation of subsynchronous interactions between pwm voltage-source converters and power networks," *IEEE Trans. Power Electron.*, vol. 29, no. 1, pp. 121–134, Jan. 2014.

[68] B. Wen, D. Dong, D. Boroyevich, R. Burgos, P. Mattavelli, and Z. Shen, "Impedance-based analysis of grid-synchronization stability for three-phase paralleled converters," *IEEE Trans. Power Electron.*, vol. 31, no. 1, pp. 26–38, Jan. 2016.

[69] H. Bai, X. Wang, and F. Blaabjerg, "Passivity enhancement in RES based power plant with paralleled grid-connected inverters ," in *IEEE ECCE'16*, Sep. 2016, pp. 72–72.

[70] L. Harnefors, A. G. Yepes, A. Vidal, and J. Doval-Gandoy, "Passivity-based stabilization of voltage-source converters equipped with lcl input filters," in *IEEE IECON'14*, Oct. 2014, pp. 1700–1706.

[71] L. Harnefors, L. Zhang, and M. Bongiorno, "Frequency-domain passivity-based current controller design," *IET Power Electron.*, vol. 1, no. 4, pp. 455–465, Dec. 2008.

[72] Q. Qian, S. Xie, L. Huang, J. Xu, Z. Zhang, and B. Zhang, "Harmonic suppression and stability enhancement for parallel multiple grid-connected inverters based on passive inverter output impedance," *IEEE Trans. Ind. Electron.*, vol. 64, no. 9, pp. 7587–7598, Sep. 2017.

[73] F. D. Freijedo, D. Dujic, and J. A. Marrero-Sosa, "Design for passivity in the z-domain for LCL grid-connected converters," in *IEEE IECON'16*, Oct. 2016, pp. 7016–7021.

[74] J. He and Y. W. Li, "Generalized closed-loop control schemes with embedded virtual impedances for voltage source converters with LC or LCL filters," *IEEE Trans. Power Electron.*, vol. 27, no. 4, pp. 1850–1861, Apr. 2012.

[75] Y. Li, P. Jia, and T. Q. Zheng, "Active damping method to reduce the output impedance of the dc-dc converters," *IET Power Electron.*, vol. 8, no. 1, pp. 88–95, Aug. 2015.

[76] L. Harnefors, "Modeling of three-phase dynamic systems using complex transfer functions and transfer matrices," *IEEE Trans. Ind. Electron.*, vol. 54, no. 4, pp. 2239–2248, Aug 2007.

[77] P. M. Dalton and V. J. Gosbell, "A study of induction motor current control using the complex number representation," in *IEEE Industry Applications Society Annual Meeting*, vol. 1, Oct. 1989, pp. 355–361.

[78] A. Aapro, T. Messo, and T. Suntio, "An accurate small-signal model of a three-phase VSI-based photovoltaic inverter with LCL-filter," in *IEEE ICPE- ECCE'15 Asia*, 2015, pp. 2267–2274.

[79] I. Cvetkovic, M. Jaksic, D. Boroyevich, P. Mattavelli, F. Lee, Z. Shen, S. Ahmed, and D. Dong, "Un-terminated, low-frequency terminal-behavioral dq model of three-phase converters," in *IEEE ECCE'11*, 2011, pp. 791–798.

[80] X. Wang, F. Blaabjerg, and P. C. Loh, "Virtual RC damping of LCL-filtered voltage source converters with extended selective harmonic compensation," *IEEE Trans. Power Electron.*, vol. 30, no. 9, pp. 4726–4737, Sep. 2015.

[81] R. Peña-Alzola, M. Liserre, F. Blaabjerg, R. Sebastián, J. Dannehl, and F. W. Fuchs, "Systematic design of the lead-lag network method for active damping in LCL-filter based three phase converters," *IEEE Trans. Ind. Informat.*, vol. 10, no. 1, pp. 43–52, Feb. 2014.

[82] J. Dannehl, F. W. Fuchs, and P. B. Thøgersen, "PI state space current control of grid-connected PWM converters with LCL filters," *IEEE Trans. Power Electron.*, vol. 25, no. 9, pp. 2320–2330, Sep. 2010.

[83] B. P. McGrath, S. G. Parker, and D. G. Holmes, "High-performance current regulation for low-pulse-ratio inverters," *IEEE Trans. Ind. Appl.*, vol. 49, no. 1, pp. 149–158, Jan. 2013.

[84] C. Bao, X. Ruan, X. Wang, W. Li, D. Pan, and K. Weng, "Design of injected grid current regulator and capacitor-current-feedback active-damping for LCL-type grid-connected inverter," in *IEEE ECCE'12*, 2012, pp. 579–586.

[85] S. Buso and P. Mattavelli, *Digital Control in Power Electronics*. San Francisco, CA, USA: Morgan & Claypool, 2006.

[86] R. Peña-Alzola, M. Liserre, F. Blaabjerg, M. Ordonez, and Y. Yang, "LCL-filter design for robust active damping in grid-connected converters," *IEEE Trans. Ind. Informat.*, vol. 10, no. 4, pp. 2192–2203, Nov. 2014.

[87] T. Roinila, J. Huusari, and M. Vilkko, "On frequency-response measurements of power-electronic systems applying MIMO identification techniques," *IEEE Trans. Ind. Electron.*, vol. 60, no. 11, pp. 5270–5276, Nov. 2013.

[88] T. Messo, A. Aapro, and T. Suntio, "Generalized multivariable small-signal model of three-phase grid-connected inverter in dq-domain," in *IEEE COMPEL'15*, 2015, pp. 1–8.

A MATLAB CODE FOR CF-VSI STEADY STATE CALCULATION

```
%#########################################################################

% ### This MATLAB code solves the steady state for a grid-connected  ###
% ### photovoltaic inverter                                          ###
% ### Aapo Aapro, 15.5.2017                                          ###

%#########################################################################


% ########### Operating point ###########

% ### With parasitic elements ###

eq1='-k1*IL2q=Ucd'
eq2='k1*IL2d-k1*IL1d=Ucq'
eq3='k2*IL2d+R*IL2q=Ucq'
eq4='R*IL2d-rC*IL1d-k2*IL2q+Uod=Ucd'
eq5='IL1d=2*Iin/(3*Dd)'

f=solve(eq1,eq2,eq3,eq4,eq5,'IL2d','IL2q','Ucd','Ucq','IL1d')

% ### Simplified IL2d IL2q ###

eq10='IL2d=(2*Iin*K_ild-3*Dd*R*Uod)/(3*Dd*K)'
eq11='IL2q=-(2*Iin*K_ilq+3*Dd*Uod*Kuo)/(3*Dd*K)'
eq12='Uin*Dd^2+rC*IL2d*Dd+IL2q*Dd*k1-2*Iin*Req/3=0'
eq13='Dq*Uin-k1*(IL2d-2*Iin/(3*Dd))+rC*IL2q-2*Iin*k3/(3*Dd)=0'
```

```
g=solve(eq10,eq11,eq12,eq13,'Dd','Dq','IL2d','IL2q')

%#########################################################################
%#########################################################################

% ### Without parasitic elements ###

eq1='-k1*IL2q=Ucd'
eq2='k1*IL2d-k1*IL1d=Ucq'
eq3='k2*IL2d+0*IL2q=Ucq'
eq4='0*IL2d-0*IL1d-k2*IL2q+Uod=Ucd'
eq5='IL1d=2*Iin/(3*Dd)'

h=solve(eq1,eq2,eq3,eq4,eq5,'IL2d','IL2q','Ucd','Ucq','IL1d')


% ### Simplified IL2d IL2q ###


eq10='IL2d=(2*Iin*K_ild-3*Dd*0*Uod)/(3*Dd*K)'
eq11='IL2q=-(2*Iin*0+3*Dd*Uod*Kuo)/(3*Dd*K)'
eq12='Uin*Dd^2+0*IL2d*Dd+IL2q*Dd*k1-2*Iin*0/3=0'
eq13='Dq*Uin-k1*(IL2d-2*Iin/(3*Dd))+0*IL2q-2*Iin*k3/(3*Dd)=0'

y=solve(eq10,eq11,eq12,eq13,'Dd','Dq','IL2d','IL2q')

%#########################################################################
%#########################################################################

% ### Now the symbolic values for Dd and Dq can be given as: ###

Dd = ((K*Req*(K_ilq*((8*Iin*Req*Uin*K^2)/3 + (8*Iin*K_ilq*Uin*K*k1)/3 -
 (8*Iin*K_ild*Uin*K*rC)/3 + Kuo^2*Uod^2*k1^2 + 2*Kuo*R*Uod^2*k1*rC
 + R^2*Uod^2*rC^2)^(1/2) + 2*K*Kuo*Req*Uod + K_ilq*Kuo*Uod*k1
 - 2*K_ild*Kuo*Uod*rC - K_ilq*R*Uod*rC))/(2*(K_ilq*k1 - K_ild*rC + K*Req))
 + (K_ilq*k1*(K_ilq*((8*Iin*Req*Uin*K^2)/3 + (8*Iin*K_ilq*Uin*K*k1)/3
 - (8*Iin*K_ild*Uin*K*rC)/3 + Kuo^2*Uod^2*k1^2 + 2*Kuo*R*Uod^2*k1*rC
 + R^2*Uod^2*rC^2)^(1/2) + 2*K*Kuo*Req*Uod + K_ilq*Kuo*Uod*k1
```

```
 - 2*K_ild*Kuo*Uod*rC - K_ilq*R*Uod*rC))/(2*(K_ilq*k1 - K_ild*rC + K*Req))
 - (K_ild*rC*(K_ilq*((8*Iin*Req*Uin*K^2)/3 + (8*Iin*K_ilq*Uin*K*k1)/3
 - (8*Iin*K_ild*Uin*K*rC)/3 + Kuo^2*Uod^2*k1^2 + 2*Kuo*R*Uod^2*k1*rC
 + R^2*Uod^2*rC^2)^(1/2) + 2*K*Kuo*Req*Uod + K_ilq*Kuo*Uod*k1
 - 2*K_ild*Kuo*Uod*rC - K_ilq*R*Uod*rC))/(2*(K_ilq*k1 - K_ild*rC + K*Req))
 - K*Kuo*Req*Uod + K_ild*Kuo*Uod*rC + K_ilq*R*Uod*rC)/(K*K_ilq*Uin)

Dq =  -((K*k1*(K_ilq*((8*Iin*Req*Uin*K^2)/3 + (8*Iin*K_ilq*Uin*K*k1)/3 -
 (8*Iin*K_ild*Uin*K*rC)/3 + Kuo^2*Uod^2*k1^2 + 2*Kuo*R*Uod^2*k1*rC +
 R^2*Uod^2*rC^2)^(1/2) + 2*K*Kuo*Req*Uod + K_ilq*Kuo*Uod*k1
 - 2*K_ild*Kuo*Uod*rC - K_ilq*R*Uod*rC))/(2*(K_ilq*k1 - K_ild*rC + K*Req))
 - (K*k3*(K_ilq*((8*Iin*Req*Uin*K^2)/3 + (8*Iin*K_ilq*Uin*K*k1)/3 -
 (8*Iin*K_ild*Uin*K*rC)/3 + Kuo^2*Uod^2*k1^2 + 2*Kuo*R*Uod^2*k1*rC +
 R^2*Uod^2*rC^2)^(1/2) + 2*K*Kuo*Req*Uod + K_ilq*Kuo*Uod*k1
  - 2*K_ild*Kuo*Uod*rC - K_ilq*R*Uod*rC))/(2*(K_ilq*k1 - K_ild*rC + K*Req))
 - (K_ild*k1*(K_ilq*((8*Iin*Req*Uin*K^2)/3 + (8*Iin*K_ilq*Uin*K*k1)/3 -
 (8*Iin*K_ild*Uin*K*rC)/3 + Kuo^2*Uod^2*k1^2 + 2*Kuo*R*Uod^2*k1*rC +
 R^2*Uod^2*rC^2)^(1/2) + 2*K*Kuo*Req*Uod + K_ilq*Kuo*Uod*k1
  - 2*K_ild*Kuo*Uod*rC - K_ilq*R*Uod*rC))/(2*(K_ilq*k1 - K_ild*rC + K*Req))
 - (K_ilq*rC*(K_ilq*((8*Iin*Req*Uin*K^2)/3 + (8*Iin*K_ilq*Uin*K*k1)/3 -
 (8*Iin*K_ild*Uin*K*rC)/3 + Kuo^2*Uod^2*k1^2 + 2*Kuo*R*Uod^2*k1*rC +
 R^2*Uod^2*rC^2)^(1/2) + 2*K*Kuo*Req*Uod + K_ilq*Kuo*Uod*k1
 - 2*K_ild*Kuo*Uod*rC - K_ilq*R*Uod*rC))/(2*(K_ilq*k1 - K_ild*rC + K*Req))
 - K*Kuo*Uod*k1 + K*Kuo*Uod*k3 + K_ild*Kuo*Uod*k1
 + K_ilq*R*Uod*k1)/(K*K_ilq*Uin)

% ### where the steady state coefficents are as follows: ###

k1=1/(ws*C)
k2=ws*L2
k3=ws*L1
R=rL2+rC
Req=req+rC
K=R^2+(k1-k2)^2
K_ild=k1^2-k1*k2+R*rC
K_ilq=k2*rC+R*k1-k1*rC
Kuo=k1-k2
```

B CURRENT CONTROLLER PARAMETERS

Parameters for the PI-based controllers, used in the analysis and experimental measurements, are shown in Table B.1. The general representation for the PI-based controller is given in (B.1).

$$G_{\mathrm{PI}} = K_{\mathrm{p}} + \frac{K_{\mathrm{i}}}{s} \tag{B.1}$$

Table B.1: Controller parameters.

Controller	Proportional gain, K_{p}	Integral gain, K_{i}
$G_{\text{cc-d}}$	0.018	22.41
$G_{\text{cc-q}}$	0.018	22.41
G_{vc}	0.36	4.47
G_{PLL}	0.67	38.02

C EXPERIMENTAL SETUP

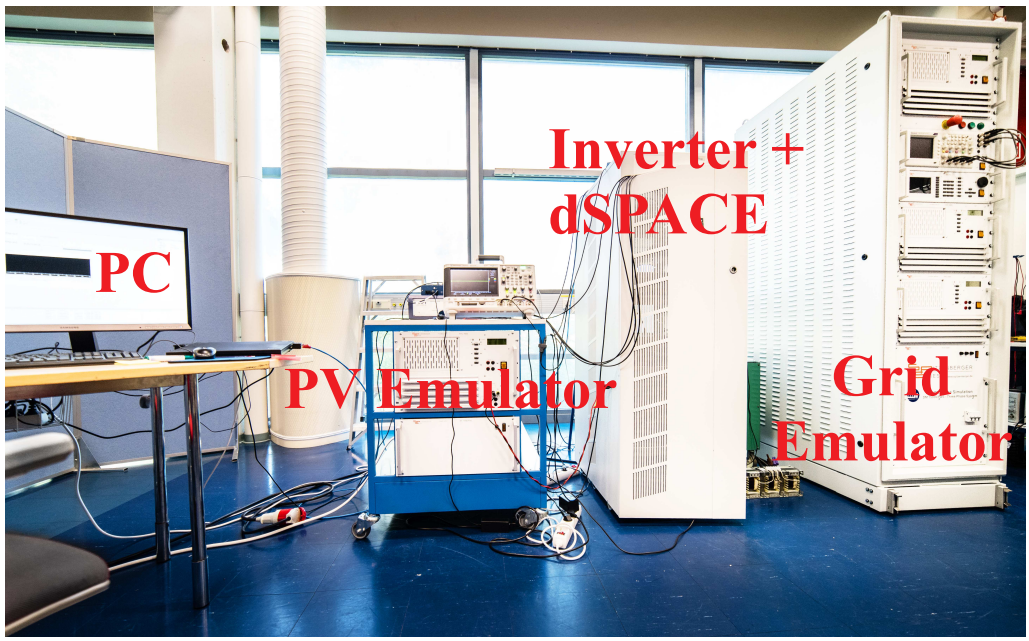

Fig. C.1: The measurement setup.

Tampereen teknillinen yliopisto
PL 527
33101 Tampere

Tampere University of Technology
P.O.B. 527
FI-33101 Tampere, Finland

ISBN 978-952-15-4013-4
ISSN 1459-2045